A Sustainable Approach to Engineering Electrode Materials & Additives for Energy Storage Systems

By

Kathleen Moyer

Dissertation

Submitted to the Faculty of the

Graduate School of Vanderbilt University

in partial fulfilment of the requirements

for the degree of

DOCTOR OF PHILOSOPHY

in

Interdisciplinary Materials Science

December 14, 2019

Nashville, Tennessee

Approved:

Cary Pint, Ph.D.

Rizia Bardhan, Ph.D.

Douglas Adams, Ph.D.

Kelsey Hatzell, Ph.D

Greg Walker, Ph.D.

ACKNOWLEDGEMENTS

There are so many people who have made this journey possible and supported me along the way. I would first and foremost like to thank Dr. Cary Pint, my advisor and mentor, who has had my best interest in mind since day one. Cary, I would not be the researcher I am today without your guidance and perseverance. Thank you for helping mold me into the scientist that I am and nurturing my sense of perpetual curiosity through your love and passion for research. Your work ethic and tireless drive to use fundamental research to solve demanding real-world problems has inspired me and so many others along the way. I would also like to extend my thanks to members of my dissertation committee, including, Dr. Rizia Bardhan, Dr. Douglas Adams, Dr. Kelsey Hatzell, and Dr. Greg Walker for their constant support and commitment to helping shape my research through their insightful suggestions and feedback over the past four years.

Further, I would like to thank all members of the Pint lab for being so instrumental in my research career, providing mentorship, valuable scientific discussions, and being an incredible support system. Specifically, I would like to thank Dr. Rachel Carter and Dr. Anna Douglas for introducing me to the Pint lab and being incredible mentors who I continue to look up to, Dr. Landon Oakes for patiently introducing me to the lab and electrophoretic deposition during my first days of grad school, Dr. Andrew Westover, Dr. Keith Share, and Dr. Adam Cohn for thought-provoking feedback and support, Dr. Nitin Muralidharan for introducing me to the wonderful world of structural batteries and always being there to lend a helping hand, Dr. Mengya Li, Dr. May Ou, Deanna Schauben, and Xiaona Wen for constant encouragement and always knowing how to put a smile on my face, Jackson Meng for help with the structural battery project and being a loyal friend, Murt Zohair and John Waugh for helping teach me how to be a better mentor and

for friendship in and out of the lab, Brice Harkey for helping me through the grad school journey and constant support and friendship, and Janna Eaves-Rathert for steadfast friendship and teaching me so much from electrochemistry to geode cakes. My graduate experience would not have been the same without the privilege of mentoring Trevor Hanken, Jennifer Donohue, Neha Ramanna, Osama Assal, Nora Ait Boucherbil, and Alex Stephens, thank you all for your dedication and hard work.

I would also like to thank Dr. Rizia Bardhan and her research group for the gracious use of their laboratory and facilities, Sarah Ross and Alisha McCord for their constant support, enthusiasm, and friendship, Dr. James McBride for his knowledge, patience, and guidance while training me on the TEM and always making himself available to help, Dr. Dmitry Koktysh, Dr. Anthony Hmelo, Dr. Alice Leach, Dr. Bill Martinez, and all the VINSE staff who have helped train and support my use of VINSE. I would like to extend a special thanks to Robin Midget for being able to come up with a solution for any problem, and for so patiently helping at the drop of a hat with mechanical testing of carbon fiber, wiring cylindrical heaters, and machining alumina rods.

In addition, I would like to thank all my professors at Vanderbilt, Stevens Institute of Technology, and teachers throughout my education who have helped inspire me in pursuing a research career. Specifically, I would like to thank Dr. Stephanie Lee for motivating me to go to grad school and her constant encouragement. I would like to extend my thanks to all the people who I worked with during summer internships and for inspiring me to continue on to graduate school. On that note, I would like to thank Dr. Barry Bunin and Beth Austin DeFares for my first research experience as part of the Maritime Security Summer Research Institute at Stevens, Dr. Ramu Ramachandran, Dr. Ayo Hassan, and Dr. Colin Wick for introducing me to energy storage

research as part of the Louisiana Alliance for Simulation Guided Materials Applications, Dr. Derek Vardon and Dr. Peter Ciesielski at the National Renewable Energy Lab for introducing me to the world of nanotechnology, clean energy, and electron microscopy and ultimately cementing my dreams of becoming a research scientist. I would also like to thank Dr. Luke Roberson, Breeanne Marshall, and the NASA Kennedy Space Center for helping extend my knowledge of structural batteries and teaching me the carbon fiber layup process. Further, I would like to thank the National Science Foundation Graduate Student Research Fellowship for their generous support and helping fund my graduate school career.

I would like to sincerely thank my entire family for their unwavering support and unconditional love. A special thank you to my parents, Pam and Stan Moyer, for always encouraging me to chase my dreams and for being faithful role models who are a continuous source of strength; my grandparents Henry and Kathy Troy for always taking the time to listen to what is going on in my life and inspiring me through their faithful example; my brother and sister, Paul and Emily Moyer, for loving me through all the ups and downs.

Finally, I would like to extend heartfelt thanks to my fiancé, Joe Vanderburgh, for helping me constantly work towards being the best version of myself. Thank you for being the motivation behind all that I do and always being there for me, from hip surgery to figure advice, while paving the path forward. I couldn’t have gotten through this grad school journey without you and am so excited for our future together.

TABLE OF CONTENTS

LIST OF FIGURES

Page

LIST OF PUBLICATIONS

Portions of this dissertation have been drawn from the following publications:

1. K. Moyer, M. Zohair, J. Eaves-Rathert, A. Douglas, C.L. Pint, “Oxygen Evolution Activity Limits the Nucleation and Catalytic Growth of Carbon Nanotubes from Carbon Dioxide Electrolysis via Molten Carbonates” *in preparation.*

2. 2. K. Moyer, R. Carter, T. Hanken, A. Douglas, L. Oakes, C.L. Pint, “Electrophoretic Deposition of $LiFePO_4$ onto 3-D Current Collectors for High Areal Loading Battery Cathodes,” Materials Science & Engineering: B, 241, 42-47 (2019).

3. K. Moyer, R. Carter, K. Share, T. Hanken, L. Oakes, C.L. Pint, “Electrophoretic Deposition as a Manufacturing Strategy for High Areal Capacity Cathodes,” *in preparation.*

4. K. Moyer, J. Donohue, N. Ramanna, A.P. Cohn, N. Muralidharan, J. Eaves, C.L.Pint, “High-Rate Potassium Ion and Sodium Ion Batteries by Co-Intercalation Anodes and Open Framework Cathodes,” Nanoscale, 10, 13335-13342 (2018).

5. K. Moyer, C. Meng, B. Marshall, O. Assal, J. Eaves, D. Perez, R. Karkkainen, L. Roberson, C.L.Pint, “Carbon Fiber Reinforced Structural Lithium-Ion Battery Composite: Multifunctional Power Integration for CubeSats,” Energy Storage Materials, (2019) doi.org/10.1016/j.ensm.2019.08.003.

6. K. Moyer, N. Ait Boucherbil, M. Zohair, J. Eaves-Rathert, C.L. Pint, “Polymer Film Stabilized Carbon Fiber Battery Electrode Interfaces for Stable and High Energy Density Structural Lithium-Ion Batteries,” *in preparation*.

Chapter 1

Introduction

1.1 Motivation

In response to ever-increasing demand for electrical power, it will be necessary to increase grid storage capacity more than 62% by 2050.[1, 2] While energy storage demand and utilization has enabled many of the technological advancements our culture enjoys today, it has also been accompanied by increasing environmental concern.[3, 4] Along with society's heightened dependence on on-demand power, there has been a surge in the concentration of atmospheric carbon dioxide (CO_2) emissions. Since the 1950s, there has been an exponential increase in CO_2 emissions in billions of metric tons, which is steadily on the rise (Figure 1.1). While there are strong initiatives set forth to keep the average rise in global temperatures below 2˚C, at the current rate of increasing CO_2 emissions, > 1.5%/year, carbon negative technologies are needed to solve this problem. With over $300 billion invested in clean energy over the last year, global energy growth is outpacing decarbonization.

One promising form of clean energy is the rechargeable lithium-ion battery (LIB).[5] From handheld electronics to grid size solutions, the developmental trend of battery technology has mainly focused on reduction of cost and improved energy storage capability. Significant advances have been made to increase the energy and power density while enhancing battery lifetime and safety.[6-11] Nonetheless, it is still critical to improve battery development to meet the demands for more energy storage capacity. While energy generation from rechargeable batteries in the form of electrochemical energy is more efficient than that sourced from fossil fuels, unfortunately, LIB

materials and manufacturing methods have a large carbon footprint.[12] Consequently, the demand for more batteries also poses the risk of increasing carbon dioxide emissions. As a result, there is a growing need for sustainable battery development to mitigate CO_2 emissions while simultaneously designing technologies to enable higher energy densities, faster charging rates, and multifunctional architectures for next-generation energy storage systems.

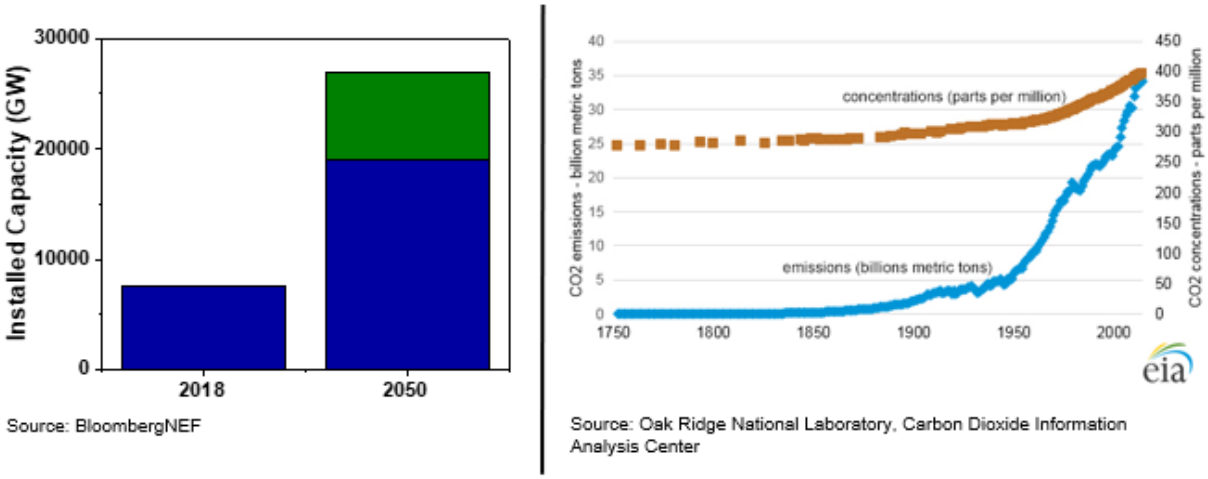

Figure 1.1 Increased energy storage demand and projected increase in installed capacity (left) from Bloomberg New Energy Finance 2019 and increased CO_2 emissions (right) from Oak Ridge National Laboratory Carbon Dioxide Information Analysis Center.

1.2 Challenges for Battery Development

Conventional LIB technology consists of two electrodes; a graphite anode and layered oxide cathode, parted by an electronically insulating but ionically conductive separator, in a lithium containing salt electrolyte that enables lithium ion (Li-ion) transfer from one side of the battery to the other (Figure 1.2). On charge, current is applied, and Li-ions move from the cathode host, through the electrolyte, and intercalate between the graphite layers of the anode. When the battery is discharged, the Li-ions move through the electrolyte back to the cathode host.

There are many components and processes that go into LIB fabrication, and many of these materials and methods have a large carbon footprint such as, 1) mining of transition metals for current collectors and cathode materials,[13] 2) cobalt containing cathode materials,[14] 3) electrolyte and battery recyclability,[15] 4) heat and energy required for synthesis of battery materials,[16] and 5) overall manufacturing of battery packs for portable electronics and grid scale storage.[17]

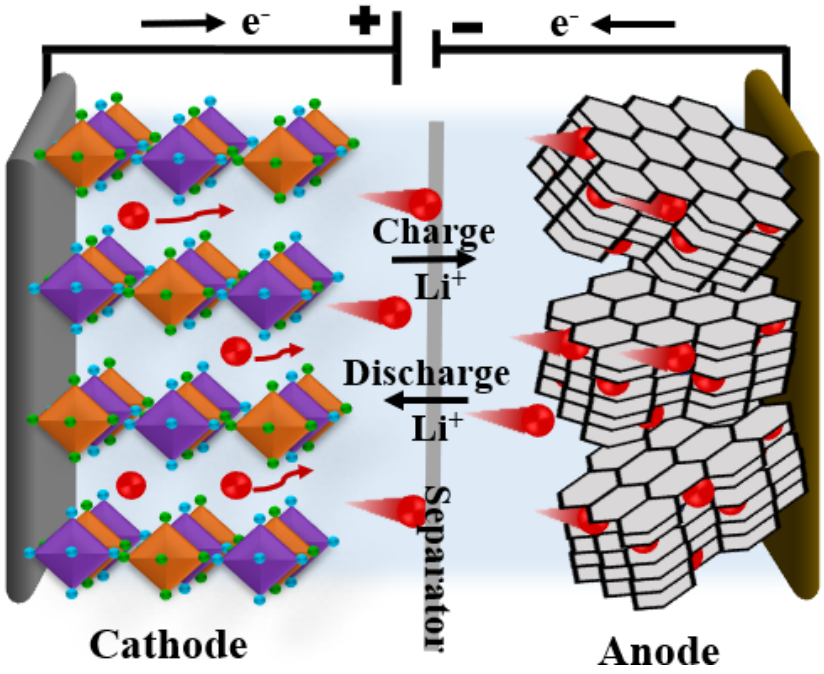

Figure 1.2 Schematic of lithium-ion battery with a graphite anode, layered oxide cathode separated by a separator in a lithium-salt electrolyte. Figure modified from Moyer et al.[18]

Transition metals such as copper and aluminum, are commonly used as anode and cathode current collectors. Oftentimes, it can be challenging to find new metal deposits, and once these metals are located in the Earth's crust, either brute force via machinery or in situ leaching are employed which either emit greenhouse gases or leach hazardous acid into the ground. In addition to toxic lithium, cobalt has been a key component of LIB cathodes since the commercialization of the LIB in the 1970s. Unfortunately, lithium and cobalt are both toxic and unstable and mining

these metals puts people at serious risk, especially since these lithium and cobalt miners are typically children who dig by hand to collect the deadly materials, posing serious violations to human rights. These processes associated with collecting materials to make LIB significantly contribute to the overall carbon footprint of battery manufacturing.

Despite the risks associated with some LIB components, once all these materials have been acquired, they are used to make various LIB battery packs for applications ranging from portable electronics to grid-level design. LIB electrodes are traditionally fabricated via slot-die casting in which battery active materials are mixed and then coated onto metal foil current collectors, calendared to a specific thickness, notch tilled, cut, and finally assembled into the cell architecture. Considering all these steps and materials, to make a single 24kWh battery pack, layered oxide cathode materials, carbonaceous anode materials and polymer binders and conductive additives require ~30 GJ of energy to be produced and manufactured into electrodes,[19] which is about 10 times the energy needed to power the average family household for a month.

Along with the heat and energy required to synthesize battery materials and assemblies, ecotoxicity contributes to the overall carbon footprint. Battery recycling is a viable way to decrease the overall carbon footprint of the LIB, however, battery recyclability is currently a serious issue that exposes society to potentially toxic materials.[20] When spent LIBs become waste, there are not strict disposal guidelines so metals such as lead, chromium, thallium, cobalt, copper, and nickel have been shown to leach out and contaminate water sources. Considering the toxicity associated with and energy required to make a LIB, the conventional LIB today has a significant carbon footprint which needs to be reduced for next-generation technologies to mitigate the concentration of CO_2 in the atmosphere.

1.3 Solution with Nanoengineering

With advances in nanotechnology, there are promising solutions to help offset the carbon footprint of LIB production while also increasing performance, driving towards goals of higher energy density and longer cycle life. Among countless different types of nanomaterials, carbon nanotubes (CNTs), boast a plethora of unique mechanical, electrical, thermal, and optical properties. These one-dimensional rolled up sheets of graphene, with diameters on the nanometer scale, boast incredible tensile strength and elastic modulus, can be either metallic or semiconducting, are excellent thermal conductors, and have useful spectral properties. Consequently, these versatile nanocarbons are highly sought-after for integration into countless applications, ranging from energy storage systems, tires, transparent conductors, and coatings, among countless others.[21, 22]

While CNTs have been on the verge of commercialization for the past twenty-five years, a significant bottleneck to integration lies within the thermodynamics of manufacturing CNTs. Traditionally, CNTs have been grown via chemical vapor deposition (CVD), a vacuum deposition process that involves a high temperature (>800˚C) furnace in which a substrate is exposed to precursor gases which then react and decompose at the substrate surface. In order to grow CNTs, a metal catalyst layer is needed on the substrates. Most substrates for CNT growth are typically silicon wafers with a support layer of alumina and then a layer or combination of metal catalyst particles such as nickel, cobalt, iron, or molybdenum. Then, as hydrocarbon gases are flown over the substrate in a hot furnace, the catalyst particle breaks down the hydrocarbon species to form CNTs. The two main problems with this synthesis strategy are 1) energy efficiency and 2) infrastructure. When hydrocarbon gases are flown over substrates in a high temperature reactor, 99.9% of the inputs are coupled to undesired reacted species other than CNTs. Also, this process

is air-sensitive and requires expensive equipment to scale up. Accordingly, alternative strategies to synthesize CNTs with enhanced energy efficiency and maximize the use of precursors is important for integration of CNTs into next-generation technologies.

Another approach to conventional CVD growth of CNTs that has recently been discovered is the electrolysis of molten carbonates.[23-25] In this system, when a current is applied, the carbonate electrolyte is reduced and carbon is deposited at the cathode, oxygen is evolved at the anode, and lithium oxide, (Li_2O) is an unstable, soluble side-product in the molten electrolyte (Figure 1.3, Eq. 1.1). To regain chemical stability, the Li_2O reacts with CO_2 consumed from air to regenerate the reacted carbonate electrolyte (Eq. 1.2). The net reaction uses greenhouse gas CO_2 to yield value-added carbon nanomaterials and oxygen (Eq. 1.3).

$$Li_2CO_3 \rightarrow Li_2O + C + O_2 \qquad \text{Eq. 1.1}$$

$$Li_2O + CO_2 \rightarrow Li_2CO_3 \qquad \text{Eq.1. 2}$$

$$CO_2 \rightarrow C + O_2 \qquad \text{Eq. 1.3}$$

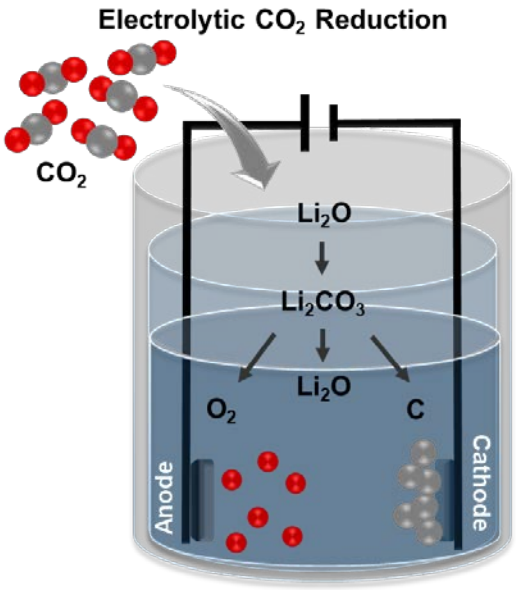

Figure 1.3 Electrolytic CO_2 reduction system with molten Li_2CO_3 where nanocarbon deposit at the cathode and oxygen is evolved at the anode.

Consequently, the carbon from the CO_2 is the carbon deposited during synthesis, resulting in a sustainable process where CO_2 from air can be converted into value-added nanocarbons while oxygen is produced at the anode.[26-29] Studying this system can help better understand the nucleation and growth process of different types of nanocarbons at the cathode. A more comprehensive insight can lead to directed product growth with increased yield of desired nanocarbons, such as CNTs. These CNTs can then be used for countless applications, including energy storage devices to help reduce the greenhouse gas emissions associated with LIBs.

1.4 Integration into Energy Storage Systems

With the alternative to synthesize CNTs via a sustainable pathway, these nanomaterials can help offset the carbon footprint of LIBs. The next challenge to address, is how to incorporate CNTs into energy storage systems and re-think how a LIB can be packaged to reduce wasted energy. Here, there is a promising solution in electrophoretic deposition (EPD) as a technique to overcome the limitations of conventional manufacturing approaches and pioneer unchartered areas of materials synthesis. EPD is a tunable and scalable process that enables one to go beyond the realm of traditional synthesis techniques to better control the desired product and build structures otherwise viewed as unfeasible.[30] This technique opens the door to a range of applications, specifically targeting fabrication of battery electrode interfaces and materials for energy storage devices. Key advantages include, ease of tunability and design, enhanced efficiency, improved interface and surface adhesion, compatibility with less-toxic materials, and scalability for industrial applications.[31, 32] EPD uses an electric field to deposit colloidal particles suspended in a liquid solvent onto an electrode to create a compact, homogeneous film.[33] Any colloidal particle that can carry an electric charge can be an EPD candidate; including polymers, pigments, dyes,

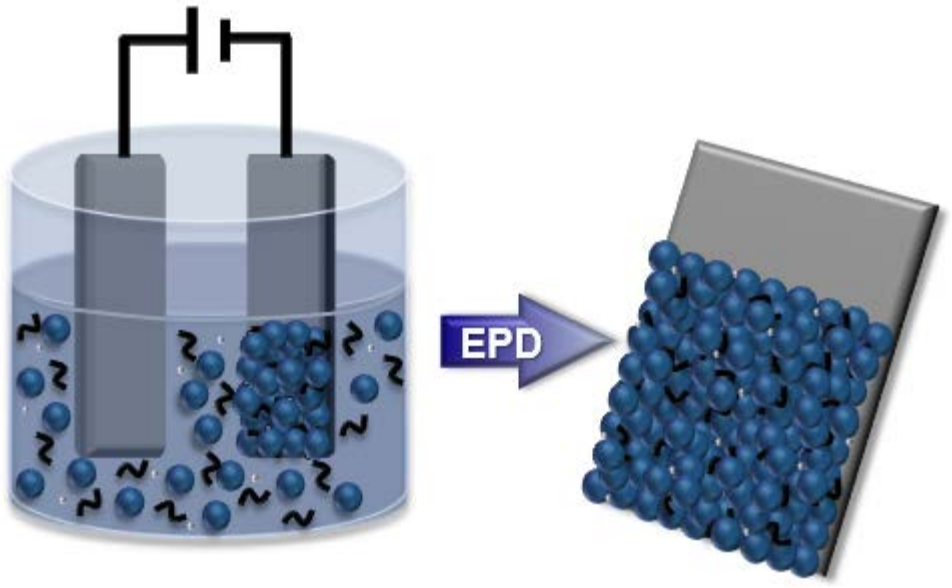

Figure 1.4 Electrophoretic deposition of active battery materials, conductive additive, and polymer binder to synthesize battery electrodes. Adapted from Moyer et al. "Electrophoretic Deposition as a Manufacturing Strategy for High Areal Capacity Cathodes," in preparation.

ceramics, and metals. EPD is typically performed in a two-electrode cell and is an excellent electrochemical method to assemble structures on a variety of substrates using a range of materials. This technique can be used to combine CNTs in solution with active battery materials and co-deposit them onto conductive current collectors to fabricate battery electrodes. Furthermore, EPD is compatible with less toxic solvent materials, such as water and alcohols, compared with organic solvents that are traditionally used in the battery fabrication process. Organic solvents, typically require a solvent recovery process which contributes a significant amount of heat and energy, and ~10%, to the manufacturing process. On the other hand, EPD helps move towards a more sustainable manufacturing platform by helping reduce toxicity in addition to removing an energy-intensive step from traditional battery manufacturing.

The integration of CNTs into battery electrodes can enhance performance of various rechargeable energy storage systems. One promising approach to improve the energy density of

LIBs is to increase the mass loading of the electrodes. Higher areal loadings of active battery material relative to inactive packaging components significantly increases overall energy density. Currently, the bottleneck associated with the design of high areal loading cathodes lies within rate capability. Oftentimes, high areal loading cathodes are densely packed and lack a conductive pathway and porous network throughout the electrode, which consequently leaves a lot of the active battery material inaccessible to alkali ions for energy storage. CNTs can enable the formation of increased mass loading electrodes through facilitating the formation of an electrically conductive and porous network that allows ion transfer. Similarly, CNTs can also enable fast charge transport for battery technology that demands faster charging times such as drones, electric vehicles, and high-power machinery. Adding CNTs to active battery materials increases conductivity and helps create a compact and porous network to enable rapid electron and ion transport, respectively, to support fast charge transport.

In addition, the enhanced electronic properties of CNTs can help overcome the resistive nature of insulating battery materials, such as alternative current collector fabrics to enable the development of multifunctional battery platforms. Structural battery design requires re-thinking how a conventional battery is packaged to ensure that each material has an active role in the system functionality. Repurposing materials that are traditionally considered inactive battery materials, such as current collectors and packaging, and making them the active mechanical components of the system further improves structural battery performance while reducing wasted materials. In order to design a structural battery with active electrochemical and structural materials, textiles and fabrics are favorable alternative current collector materials that offer both energy storage capability and structural integrity. Unfortunately, even carbon cloth and carbon fiber weaves are more insulating compared to traditional metallic foil current collectors such as copper and

aluminum. Therefore, to enable charge transport in these alternative designs, CNTs can help overcome resistance in multifunctional systems and present a simple and effective solution to improve energy storage performance.

In this work, I will demonstrate how the addition of CNTs can augment energy storage capabilities in a range of systems such as, 1) facilitate the development of high areal capacity electrodes,[34] 2) enable high rate capability full-cells,[18] and 3) overcome insulating nature of electrode materials for integration into multifunctional energy storage platforms.[35] Overall, the idea of integrating sustainably synthesized CNTs into energy storage systems, using alternative LIB manufacturing platforms such as EPD, and rethinking battery packaging for multifunctional architectures helps mitigate the carbon footprint of the battery. Synthesizing CNTs from the electrolytic reduction of carbon dioxide presents a sustainable alternative to CNT manufacturing while higher areal-loading electrodes and battery repackaging makes use of inactive materials that are traditionally a source of wasted energy. This sustainable approach has the promise to enhance the performance of rechargeable battery systems to achieve improved energy storage capability and increase the energy and power density while enhancing battery lifetime and safety.

1.5 Dissertation Organization

This dissertation is organized as follows:

Chapter 2 studies the rate-limiting step in the electrochemical conversion of atmospheric carbon dioxide into valuable CNTs. This chapter demonstrates a unique cooperative effect between transport and the onset and effectiveness of catalytic growth that is necessary to understand to produce size-controlled and high quality crystalline high-valued carbon nanomaterials from CO_2 mitigated from the air.

Chapter 3 utilizes electrophoretic deposition as a technique to fabricate LIB cathodes with different areal loadings on 3-D current collectors. This emphasizes EPD as both a technique to overcome the limitations of conventional manufacturing approaches in scaling to 3-D collector architectures for improved cell-level energy density.

Chapter 4 builds upon the findings in chapter 3 to demonstrate electrophoretic deposition as a route to manufacture high areal capacity battery electrodes with multiwall carbon nanotubes that enable operation at high rates.

Chapter 5 demonstrates a full-cell battery design that bridges the energy density and rate capability between that of supercapacitors or pseudocapacitors with that of traditional lithium-ion batteries. This is accomplished by pairing an anode that enables ultrafast ion co-intercalation, an open framework cathode that allows rapid ion diffusion, and linear ether-based electrolyte that sustains cell-level stability and high rate performance.

Chapter 6 studies a multifunctional battery platform where lithium-ion battery active materials are combined with carbon fiber weave materials to form energy storage composites using traditional layup methods. Structural battery panels developed from this approach are demonstrated as an integrated power delivery platform for a 1U CubeSat frame to augment or replace interior external battery packs.

Chapter 7 builds upon the findings in chapter 7 to study a key challenge of material delamination while designing a structurally robust lithium-ion battery composite material. A thin electroconductive poly acrylonitrile, or PAN, coating applied to the surface of the fiber/active material current collector drastically improves the performance of a carbon fiber reinforced structural battery material.

Chapter 8 summarizes the work of this dissertation and outlines future opportunities.

Chapter 2

Oxygen Evolution Activity Limits the Nucleation and Growth of Carbon Nanotubes from Carbon Dioxide Electrolysis via Molten Carbonates

Adapted from: K. Moyer, M. Zohair, J. Eaves-Rathert, A. Douglas, C.L. Pint, "Oxygen Evolution Activity Limits the Nucleation and Catalytic Growth of Carbon Nanotubes from Carbon Dioxide Electrolysis via Molten Carbonates" *in preparation.*

2.1 Introduction

Carbon nanotubes (CNTs) and their growth mechanisms have captivated the nanotechnology community now for decades.[21, 22] Despite much promise, a critical factor that holds back the widespread application of CNTs in bulk manufactured products is the high cost of CNTs in the commercial marketplace. This high cost arises due to a combination of the costly energy, materials, and infrastructure needed to produce CNTs with conventional gas-phase synthesis approaches, such as fluidized bed and other forms of chemical vapor deposition processes.[36] In turn, new approaches to produce CNTs with better energy efficiency and high utilization of precursors remains important to this ongoing effort and the foundation for next-generation mainstream applications where CNTs can be incorporated, such as in tires, membranes, coatings, batteries, among many other applications.

One alternative strategy to conventional gas-phase growth of carbon nanostructures that has recently been discovered has been the electrolysis of molten carbonates.[23-25] In this case, electrolytic reduction of molten carbonate allows carbon to be evolved at the cathode, oxygen

evolved at the anode, and CO_2 scavenged from air to replenish the reacted carbonate. In this way, the carbon atom in CO_2 is the active species for synthesis, making this a sustainable process where CO_2 from air can be transformed into solid carbons while oxygen is evolved.[26-29] Whereas the first report of carbonaceous deposition from molten carbonates was reported in the 1960's, only through the past decade have researchers begun to adapt this process to new electrodes and observe and study the formation of nanostructured carbons. So far, a number of carbons have been synthesized using different techniques including nanoporous carbons,[37] graphene platelets,[38] carbon nanofibers,[39] hollow nanofibers,[40] and most recently multi-walled carbon nanotubes with diameters in the 10-30 nm range.[41, 42] Specifically in the case of CNTs, a key advance toward achieving electrochemical CNT growth with diameters competitive with commercial CNT materials (e.g. < 30-50 nm) was anode passivation to mitigate corrosion of commonly used anode metals, such as Ni, into the molten carbonate media.[42] Since metal anode corrosion has been shown to adversely impact the controlled catalytic formation of carbons at the cathode, this passivation layer isolates the catalytic process of CNT growth to the cathode, facilitating cathode design in a manner parallel to gas phase CNT growth, involving Fe catalyst particles either formed from, or coated onto the cathode surface.[41, 42]

However, since CNT formation involves both a catalytic assembly process of carbon at the cathode and also combined full-cell reaction between the anode and cathode to evolve oxygen and deposit carbon, respectively, this requires cooperation between rate kinetics of these two separate but intertwined processes to form CNTs. From a broader perspective of studies focused on the latter case with the non-catalytic deposition of carbon, key advances have emerged regarding the electrolysis of carbonate molten salts. First, work by Yin et al. used three-electrode cyclic voltammograms along with various anodes and concluded that the choice of anode material

governs the rate of the reaction for electrochemical growth of carbon powders.[37] Very recently, a series of advances from Gao et al. has further isolated mechanisms of anode-limited electrochemistry in molten salts and studied the roles of temperature and convection to control cathode polarization.[43, 44] This work emphasizes that with a poor oxygen evolving anode, sluggish rate kinetics result in poor transport of oxide ions (O^{2-}) from the cathode to the anode, resulting in buildup of lithium oxide (Li_2O) at the cathode. To reduce cathode polarization and accelerate reaction kinetics, two strategies have been demonstrated. First, the solubility of Li_2O that forms across this interface can be improved by increasing the reaction temperature.[43, 45] Second, diffusion of Li_2O from the cathode to the anode can be improved by introducing a hollow gas bubbling electrode into the system. Outside of this, a number of other researchers have observed that perturbing transport in the system by processes such as bubbling CO_2 directly into the electrolyte[46] and introducing a CO_2 atmosphere[47-49] can affect the properties of the carbon deposited during non-catalytic carbon growth, in line with these observations. However, there remains a lack of understanding relating to how the rate limitations associated with the oxygen transport and evolution at the anode can have a corresponding impact on catalytic growth at the cathode, such as is the case during synthesis of carbon nanostructures such as graphene and CNTs.

In this spirit, we demonstrate in this study that the catalytic growth of CNTs during carbonate mediated CO_2 electrolysis is essentially turned on or off based on the oxygen evolution activity of the anode. By comparing stable but poor oxygen evolving anodes, such as copper, with stable anodes exhibiting enhanced oxygen evolution characteristics, like alumina-coated nickel wire and platinum,[49] our results show that the onset of catalytic CNT growth versus non-catalytic micro-fibrous growth is controlled by the anode. Further, our work highlights that in the two cases where CNT growth is observed, CNT properties such as crystallinity are anode-dependent. This

work builds upon recent advances in the electrochemistry of molten salts to demonstrate and distinguish key mechanisms associated with the formation of high quality and controlled CNTs and other valuable carbon nanostructures catalytically produced via carbons sequestered from CO_2.

2.2 Experimental Details

2.2.1 Electrode Materials Preparation

2.5 cm^2 316 stainless steel (Trinity Brand Industries) with 5 nm Fe deposited by e-beam evaporation was used as the cathode for all experiments. Three different anode materials were used: Copper wire (The Hillman Group, 18 gauge), Platinum wire (Fisher Scientific, 99.95%), and Alumina coated Ni wire (Fisher Scientific, 99%). Atomic layer deposition (ALD) using a Gemstar Arradiance system was used to coat the Ni wire with 50 nm of Al_2O_3 by pulsing 28 ms of $C_6H_{18}Al_2$ (TMA) and water with a residence time of 1 second for 500 cycles. An A J.A. Woollam spectrometer was used to measure the thickness of the deposited Al_2O_3 on a silicon wafer and was determined to be 50 nm. All anodes were 6 cm^2 unless otherwise specified in the text.

2.2.2 Carbonate Mediated Carbon Dioxide Electrolysis

40 g lithium carbonate, Li_2CO_3 (Fisher Scientific, 99%), electrolyte was dried under vacuum at 100˚C overnight and used for all electrolysis experiments in 100 mL alumina crucibles (AdValue Technology). The electrolyte was used for 5 hours before disposal. A ceramic fiber cylinder heater (Thermcraft) and temperature controller (OEM Heaters) were used to heat the crucibles filled with electrolyte to 750˚C. Once the electrolyte reached the setpoint of 750˚C, the anode and cathode were placed in the molten Li_2CO_3 electrolyte. A current was then applied between the electrodes for one hour. After the electrolysis, the electrodes were removed from the

electrolyte and allowed to cool before removing carbon from the cathode. The collected carbon was washed in deionized water in a bath sonicator for one hour and then washed in 2 M HCl to remove residual Li_2CO_3 electrolyte. The carbon was collected by a centrifuge and solvent exchange to deionized water and dried overnight at 60˚C.

2.2.3 Cyclic Voltammograms

Cyclic voltammetry was conducted using a 5 nm Fe on stainless steel cathode and one of the previously specified anode materials, copper, platinum, or Al_2O_3 coated nickel. These materials were used as working and counter electrodes as indicated. A pseudo Ag/AgCl reference electrode was used. This was fabricated by machining a closed-one-end alumina tube to a wall thickness of ~0.1 mm and then filling the rod with Li_2CO_3 electrolyte and 10% AgCl (Sigma Aldrich, 99.999%). The Ag/AgCl reference was melted to 750˚C before beginning any experiment.

2.2.4 Characterization

Raman spectroscopy (Raman Microscope Thermo Scientific DXR) with a 532 nm^{-1} laser excitation, 10 mW laser power, 900 lines/mm grating and 50x objective lens was used to analyze the degree of graphitization of the carbon and electron microscopy was used to investigate the morphology and elemental composition with a scanning electron microscope (Zeiss Merlin) and transmission electron microscope (FEI Tecnai Osiris).

2.3 Results & Discussion

In order to study the role of the anode in the electrolysis of molten carbonates and subsequent catalytic growth of CNTs, electrolysis experiments were conducted using the same cathode material of 5 nm Fe on stainless steel with different oxygen evolving anodes that were tested to be thermally and chemically stable from corrosion in lithium carbonates. Until now,

previous studies focused on CNT growth in molten carbonates have demonstrated engineered cathodes where catalytic metal nanoparticles, such as Fe, can be isolated as catalysts for CNT growth in a manner analogous to gas-phase chemical vapor deposition or other processes. However, reports so far have shown CNTs with slightly larger diameters and higher defect content in electrochemical synthesis methods, which can be partially attributed to accelerated Ostwald ripening of catalysts at the cathode. However, in light of recent reports of the strong effect of the anode on the non-catalytic growth of carbons in this general process,[43, 44] our key motivation in this study is to understand how the activity of the anode impacts the catalytic formation of the CNTs on the cathode.

Outside of the catalytic mechanisms that drives CNT growth, when lithium carbonate electrolyte is reduced to carbon, the electrochemical reduction at the cathode is:[22, 43, 46, 48, 50-52]

$$CO_3^{2-} + 4e^- \rightarrow C + 3O^{2-} \quad \text{Eq. 2.1}$$

This electrochemical reduction of Li_2CO_3 in a single four electron step to carbon and Li_2O is thermodynamically favorable.[51] The anodic reaction oxidizes O^{2-} ions to oxygen:[22]

$$2O^{2-} \rightarrow O_2 + 4e^- \quad \text{Eq. 2.2}$$

This is a cyclic process as the carbonate electrolyte is regenerated by CO_2:[22, 43, 48, 50]

$$CO_2 + O^{2-} \rightarrow CO_3^{2-} \quad \text{Eq. 2.3}$$

All these reactions yield a net reaction of:

$$CO_2 \rightarrow C + O_2 \quad \text{Eq. 2.4}$$

Cyclic voltammograms (CVs) were first performed to better understand concentration polarization controlled by mass transfer (Figure 2.1). A 5 nm Fe on stainless steel cathode was the working electrode and the counter electrode was either copper (Cu) wire, alumina coated nickel (Ni/Al_2O_3) wire, or platinum (Pt) wire with a pseudo Ag/AgCl reference electrode. All peaks labeled “C” in

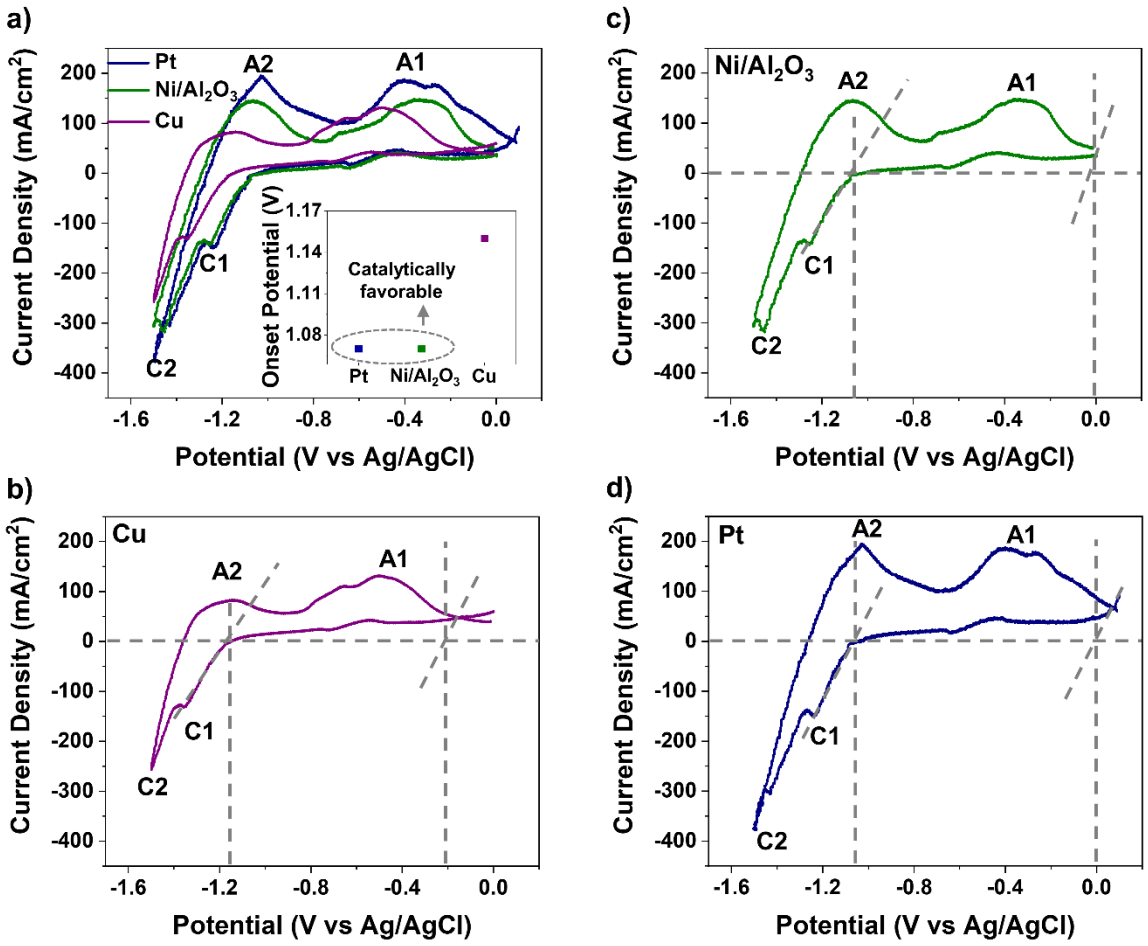

Figure 2.1 Cyclic voltammograms of Ag/AgCl reference electrode, 5 nm Fe on stainless steel working electrode and a) 1st cycles of Pt, Ni/Al_2O_3, and Cu counter electrodes with inset of anode vs onset potential for each material and calculation of onset potential for each anode material, b) Cu, c)Ni/Al_2O_3, d) Pt.

Figure 2.1 are reduction peaks and peaks labeled “A” are due to oxidation. The CVs were performed at a scan rate of 5 mV/s and the onset potential was analyzed by drawing lines tangent to the slope of peak C1 to determine at what potential carbon deposition began in each system. The onset potential was calculated by taking the difference between the potential at which carbon deposition began and the tangent to the anodic limit (Figure 2.1b, c, d). In this characterization, we attribute a lower onset potential to represent a configuration that is more favorable for catalytic carbon growth that appears associated with enhanced oxygen evolution to limit cathodic

polarization (Figure 2.1a inset). Remarkably, it appears from these CV curves that the catalytic activity of the cathode is essentially "switched off" or at least adversely modified by the use of the anode expected to provide the poorest oxygen evolution activity, in this case Cu. In addition to the signature of catalytic formation of carbon species that is evident in the CV curves, these curves also indicate the oxygen evolution of the different anodes that were studied. Peak C1 is the reduction of carbonate ions to carbon (Eq. 2.1) and this peak is also related to the oxide ions, another reduction product.[37, 53-55] The presence of this reduction peak indicates that carbonate ion reduction is controlled by a mass transfer step.[43] This indicates that the evolution of O^{2-} ions to O_2 (Eq. 2.2) is the rate-limiting step of the cathodic process and sluggish reaction kinetics results in buildup of Li_2O on the cathode, as was observed in past reports.[43, 44]

Based upon this, if the system reaction kinetics are slow and the rate-limiting step is the evolution of O^{2-} ions to O_2 (Eq. 2.2), then Li_2O can accumulate at the cathode interface. Whereas this has been recently studied by Gao et al. for non-catalytic growth of carbons in this process,[43, 44] our findings indicate that this Li_2O layer makes the cathode, and any catalyst layer on the cathode, less accessible for directed CNT growth (Figure 2.2a). When the rate kinetics are enhanced to minimize concentration polarization at the cathode, the catalysts are available for carbon nucleation, resulting in CNT growth (Figure 2.2b).

To extend the observations made in three-electrode CV scans, we characterized the resulting growth of carbons on the cathode both with the different anodes of Cu wire, Ni/Al_2O_3 wire, and Pt wire, as well as at different current densities (Figure 2.3). A 5 nm Fe on stainless steel cathode was used for all experiments and current densities of 50 mA/cm^2, 100 mA/cm^2, 200

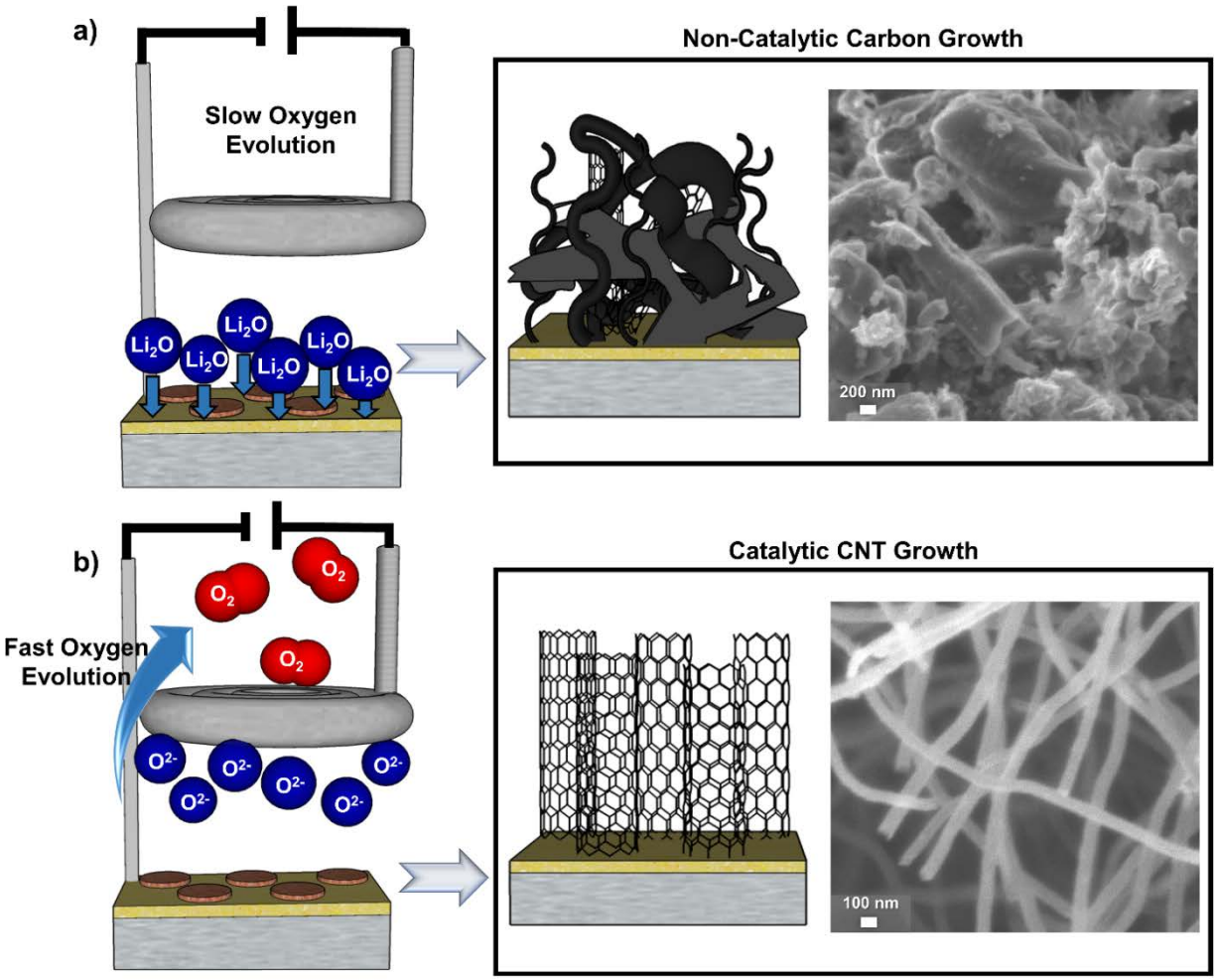

Figure 2.2 Scheme of oxygen evolution for a) poor oxygen evolving anode materials and resulting carbon product and b) enhanced oxygen evolving anodes and resulting carbon nanotubes. mA/cm^2, 400 mA/cm^2, were applied for 60 minutes. The resulting carbon grown can be seen in Figure 2.3a-l. When Cu was used as an anode, tube growth was not observed under any condition.

At the lower current densities of 50 mA/cm^2 (Figure 2.3a) and 100 mA/cm^2 (Figure 2.3b), the morphology of the carbons bore little resemblance to any nanostructured materials. As the current density was increased, the carbon morphology appeared to have a more fibril-like character (Figure 2.3c, d), but in all cases the feature sizes were on the scale of 200 nm or greater, which is above that which is defined as a nanomaterial (Figure 2.12). Ni/Al_2O_3 and Pt anodes showed similar trends in that at 50 mA/cm^2 no tube growth was observed (Figure 2.3e, i) and as the current

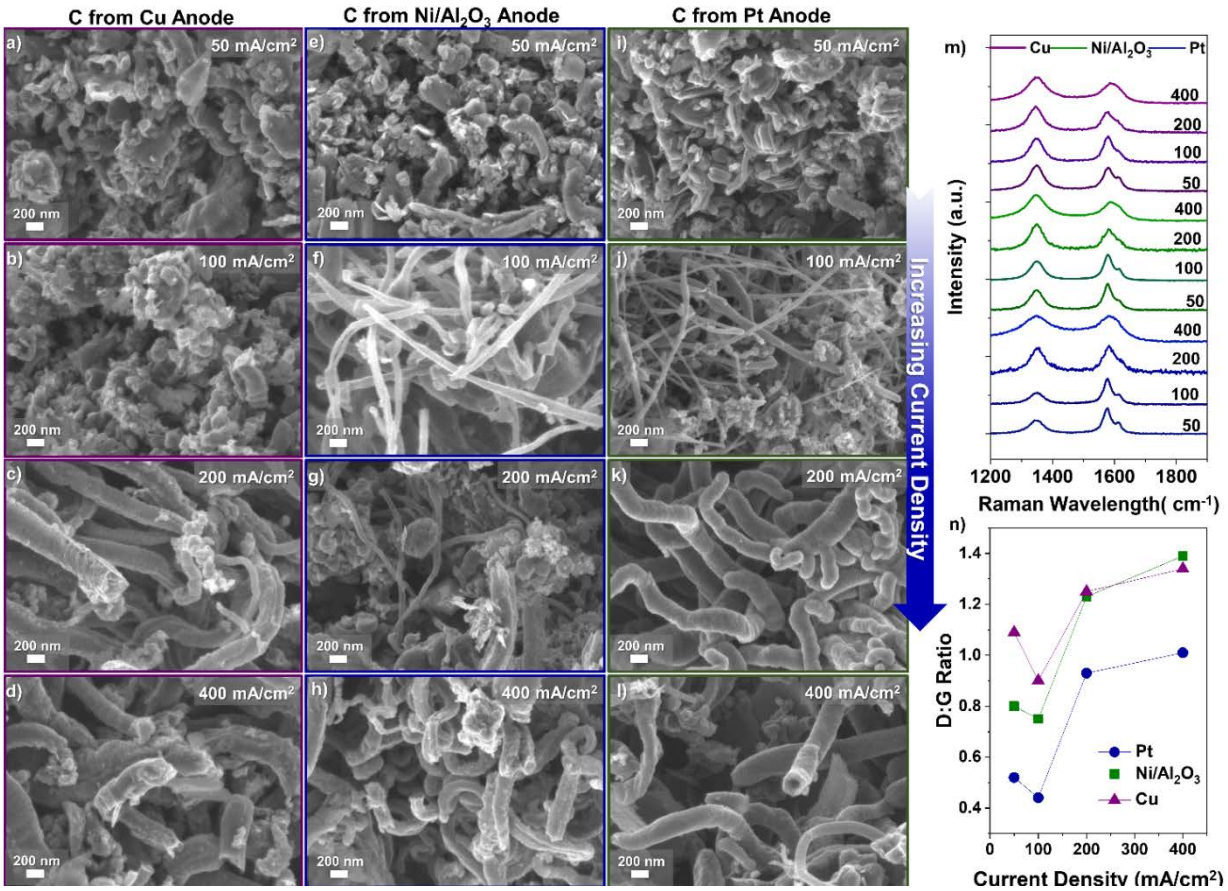

Figure 2.3 SEMs of carbon grown at different current densities using 5 nm Fe on stainless steel cathode with anode materials; a-d) Cu, e-h) Ni/Al2O3, i-l) Pt and m) Raman spectra and n) D:G ratio vs current density.

density was doubled to 100 mA/cm^2, the barrier to realize catalytic CNT growth was overcome and CNTs were observed in both cases. An analysis of the CNT diameter was performed for conditions that resulted in tube or tube-like growth and can be found in Figure 2.12. The tubes grown at 100 mA/cm^2 with the Pt wire anode (Figure 2.3j) resulted in a nearly 2X smaller diameter, mean diameter of 50 nm, than those grown using the Ni/Al_2O_3 anode, mean diameter of 100 nm. (Figure 2.3f), but both samples overall showed CNT growth consistent with that observed previously. As the current density was further increased to 200 mA/cm^2 and 400 mA/cm^2, the

tube-like character remained but the diameter of the resulting tubes significantly increased (Figure 2.12) likely due to the increased current density and different stages of growth of the tubes.

Whereas SEM images can provide information on the morphology and size of the CNTs, another important factor to characterize is the crystallinity of the CNTs. One reliable technique for this purpose is Raman spectroscopy, where the signature of sp^3 hybridized carbon (D-mode) and sp^2 hybridized carbon (G mode) species can be quantified. A CNT with a high degree of crystallinity will exhibit a low D mode relative to the G mode, and vice versa for a "defective," or low-crystallinity CNT. Raman spectra taken with 532 nm excitations are shown in Figure 2.3m for the CNTs grown with the different anodes studied, and at different current densities. Further, Figure 2.3n shows the ratio of the D:G peak intensity from all anodes. The most tube-like character and lowest D:G ratio occurred at current densities of 100 mA/cm^2 for all cases (Figure 2.3n). At higher current densities, the degree of graphitization decreased which is likely due to heightened reaction rates at the cathode coupled with rate-limited oxygen evolution at the anode. Here we believe that even though the reaction efficiency at the cathode increased, if the anode is not able to rapidly support oxygen evolution, O^{2-} mass transfer is sluggish resulting in Li_2O buildup at the cathode and decreased carbon graphitization. However, regardless of the trends between different measured current density, in all cases it is clear that the greatest level of CNT crystallinity is achieved when utilizing an anode with the highest oxygen evolution activity, which is in this case Pt. Based on this argument, we believe that in the case of Cu anodes, the sluggish diffusion kinetics leads to a significant amount of Li_2O buildup at the cathode/carbonate interface, which in this case stifles the catalytic process of CNT growth altogether.

With this understanding in place, one can equally argue that a moderately good oxygen evolution anode that exhibits a large surface area and hence more active sites (relative to the cathode), may exhibit comparable or better performance at the system level than a smaller but better oxygen evolving anode. To test this idea, we studied the effect on CNT synthesis as the surface area of the anode relative to the cathode was increased from a 1:1 ratio to a 20:1 ratio (Figure 2.4). Notably, all prior studies discussed were based on an anode to cathode ratio of 2.4:1,

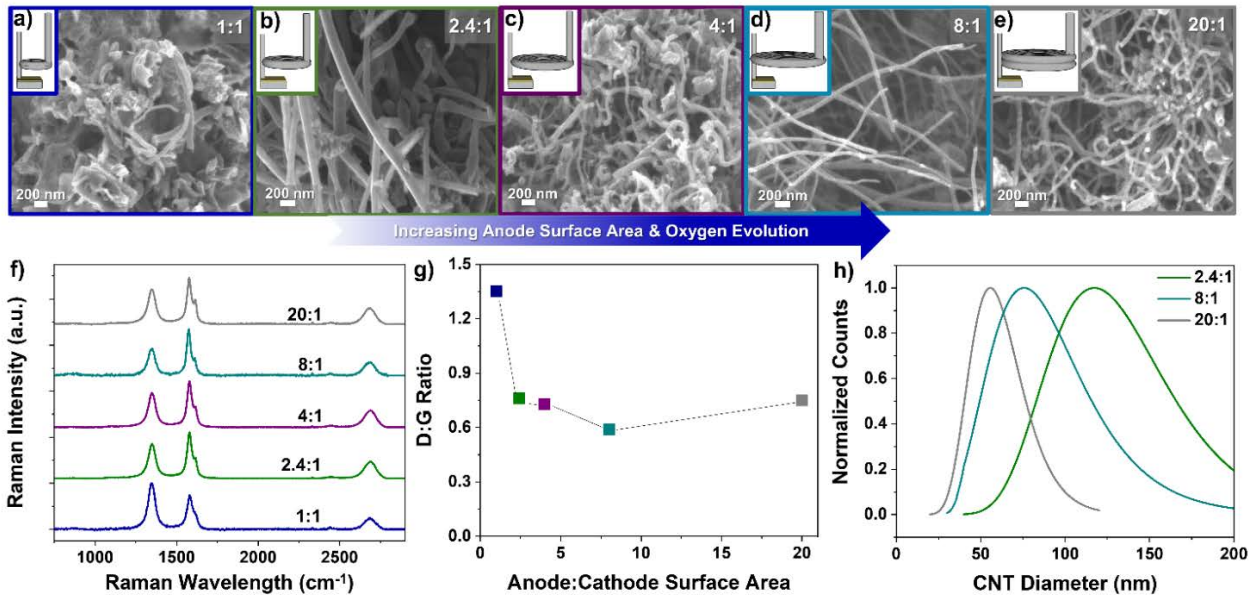

Figure 2.4 Anode surface area study using a Ni/Al_2O_3 anode with 5 nm Fe on stainless steel cathode with different anode to cathode surface area ratios (A:C) and the resulting carbon product from ratios; a) 1:1, b) 2.4:1, c) 4:1, d) 8:1, e) 20:1 and f) Raman spectra, g) D:G Ratio vs Anode:Cathode surface area, and h) normalized lognormal fits from histogram of CNT diameter distribution at ratios of 2.4:1, 8:1, and 20:1.

thereby a 1:1 ratio results in a decreased anode area, and 4:1 or greater ratios reflect an increased anode area. In all studies, the size of the cathode, the composition of the cathode (5 nm of Fe on stainless), and the current density at the cathode surface (100 mA/cm^2) remained the same. In this case, the Ni/Al_2O_3 passivated anode was chosen due to its moderate oxygen evolving activity that leads to CNT growth, but with a lower overall crystallinity of the CNTs compared to the case of

Pt anodes. Similar to Figure 2.3, we analyzed the variation of two key characteristics with anode to cathode size mismatch: the CNT diameter distribution and the CNT crystallinity. Notably, as the ratio of the anode to cathode surface area increased, the crystallinity and yield of CNTs increased up until a peak at a ratio of 8:1 (Figures 2.4f and g). However, further increasing the anode size relative to the cathode up to 20:1 led to slightly lower CNT crystallinity. In the latter case, we attribute this to the highly mismatched anode/cathode sizes that causes the electric field generated between the anode and cathode to no longer be uniform. This causes field lines to "spill over" to the backside of the cathode due to the size mismatch, causing the *effective* current density to be lower on the cathode surface containing Fe. Similarly, looking at normalized lognormal histograms of the CNT diameter distribution (Figure 2.4h and Figure 2.14), it is clear that increasing the anode to cathode ratio leads to a significant decrease in CNT diameters by more than a factor of 2X, from > 100 nm in diameter to ~50 nm.

Overall, comparing the observations made in CNT crystallinity and CNT diameter between these two different experiments discussed in Figure 2.3 and Figure 2.4 demonstrates a consistent and compelling story emphasizing the importance of the oxygen evolution activity of the anode. In both cases, a higher oxygen evolution activity at the anode, regardless of whether this is intrinsic to the anode size or anode composition, results in smaller CNT diameters and higher CNT crystallinity. In turn, this means that rate kinetic bottlenecks associated with oxygen evolution at the anode are cooperative with the catalytic mechanisms resulting in CNT formation at the cathode. To better understand this, we carried out HR-TEM analysis along with analytical STEM-EDS characterization of carbon nanomaterials grown with Ni/Al_2O_3 cathodes at both 1:1 anode to cathode ratios to 20:1 ratios, respectively (Figure 2.5). As is evident in the elemental maps, there is a higher degree of oxygen content in the carbons produced with the 1:1 ratio, 2.76 atomic%

relatively (Figure 2.5k), compared to the 20:1 ratio, 0.37 atomic% relatively (Figure 2.5l). Based on this data and building from past studies, we propose that this higher oxygen content in the carbons arises from a buildup of oxide species at the cathode interface due to the rate-limiting

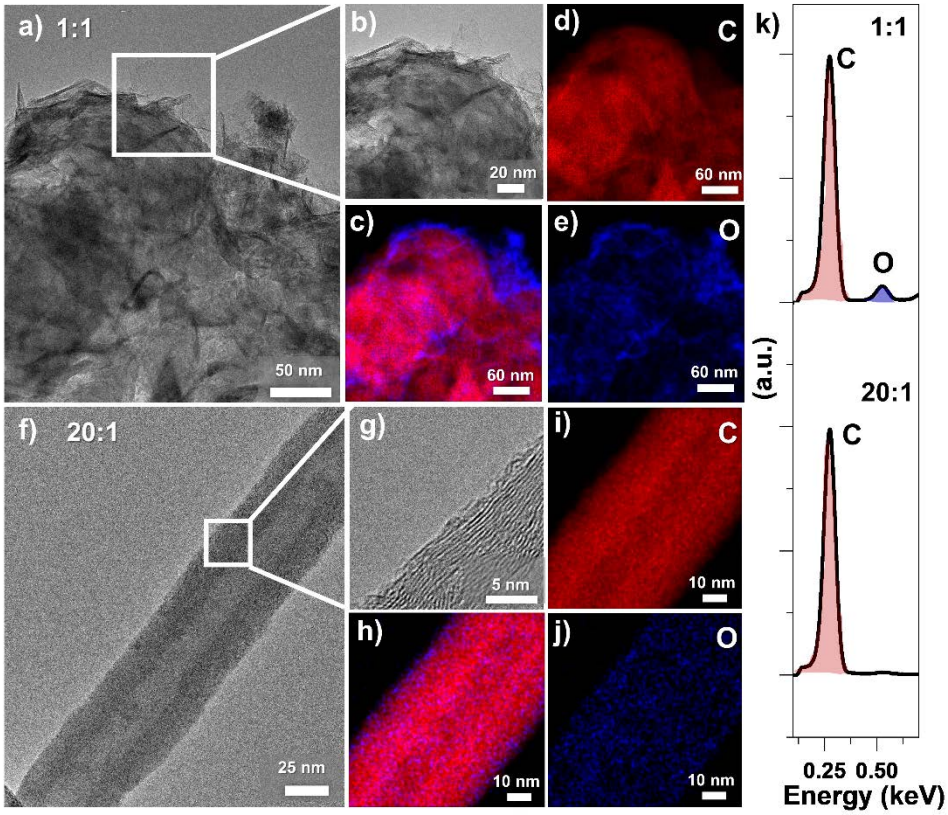

Figure 2.5 TEM images of carbon grown at an anode: cathode surface area a ratio of 1:1 (a-e) and at a ratio of 20:1 (f-j) and k) corresponding STEM-EDS elemental spectra.

transport of these species to the anode. This causes side reactions at the cathode where oxygen-containing species are incorporated into the carbon nanomaterials that are synthesized. This mechanism also explains the lack of CNT growth observed when using an anode with a poor oxygen evolution capability, since the incorporation of too many oxide species along with the carbons can render the transition metal catalysts ineffective for catalytic growth. Whereas this explains the effect of the anode on the crystallinity, Figure 2.3 and Figure 2.4 both indicate that a better oxygen evolving anode results in a smaller diameter distribution of CNTs. In this case, it is

well known that the CNT diameter distribution is a direct reflection of the particle size distribution of the metal catalyst particles where carbons are solubilized and precipitated as CNTs. Our observations therefore reflect that a correlation must exist between catalyst particle size formed from a uniformly deposited 5 nm thick coating of Fe on a stainless surface, and the resulting CNTs that are produced. Unlike traditional gas-phase CNT growth where this size distribution is dictated by the underlayer onto which the catalyst layer is deposited, in this electrochemical system there is an equal or greater role of the carbonate and its local properties at the cathode-carbonate interface to dictate catalyst formation and catalyst size. This indicates that the catalyst size that forms is the largest when there is an oxide layer at this carbonate-cathode interface due to a poor oxygen evolving anode. This makes sense since the Li_2O layer has been shown to increase the surface tension[56, 57] of the carbonate-cathode interface and lead to larger particle formation.

2.4 Conclusion

Overall, these results provide a consistent picture regarding the formation of an oxide layer at the cathode interface in the absence of an anode with high oxygen evolution activity, and in accordance with recent studies on non-catalytic growth of carbons using molten carbonate electrolysis. Our findings show that this oxide layer has an evident role both in the emergence of catalytic growth at the cathode as well as the physical characteristics of CNTs catalytically synthesized. Poor oxygen evolving anodes lead to significant uptake of oxygen species in carbon deposited at the cathode, which deactivates metallic catalyst particles and leads to non-catalytic growth. Increasing the oxygen evolution activity of the anode leads to the onset of catalytic growth at the cathode surface, and the emergence of CNTs with higher crystallinity and smaller diameters. These results are consistent between two separate sets of experiments where the oxygen evolving

activity of the anode is modified by either (1) changing the composition of the anode from stable materials showing low oxygen evolution activity (Cu) to those showing high oxygen evolution activity (Pt), and (2) keeping the anode composition fixed, but changing the ratio of anode to cathode surface area.

From a broader perspective, the ability to synthesize high-valued carbon nanomaterials that are of great relevance to technological systems from CO_2 mitigated from the air has strong future implications at the intersection of technology and sustainability. However, the inability to control the process of catalytic formation of different valuable nanostructures poses a major challenge to producing small diameter CNTs (< 10 nm) and other atomically precise carbon nanostructures that pose the greatest value proposition toward these technologies. Our work presents new insight into a unique cooperative effect between transport in a carbonate medium and catalytic growth at an electrode surface that must be understood and optimized to realize control over catalytic CNT growth from CO_2 based on molten carbonate electrolysis.

Acknowledgments

The authors thank Robin Midgett for help machining the reference electrode and electrical wiring, the laboratory facilities of Prof. Rizia Bardhan for use of the centrifuge, and the VINSE laboratory facilities for use of the Raman spectrometer and the spectroscopic ellipsometer to measure Al_2O_3 thickness, SEM, TEM, and Dr. James McBride for his TEM guidance. K.M. is supported by NSF fellowship under grant 1445197.

2.5 Appendix

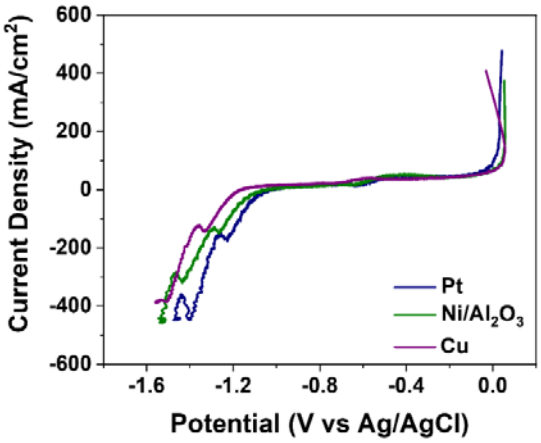

Figure 2.6 Linear sweep voltammograms at a scan rate of 10 mV/s with 5nm Fe on stainless steel working electrode, Pt, Ni/Al_2O_3, or Cu counter electrode, and Ag/AgCl pseudo-reference electrode.

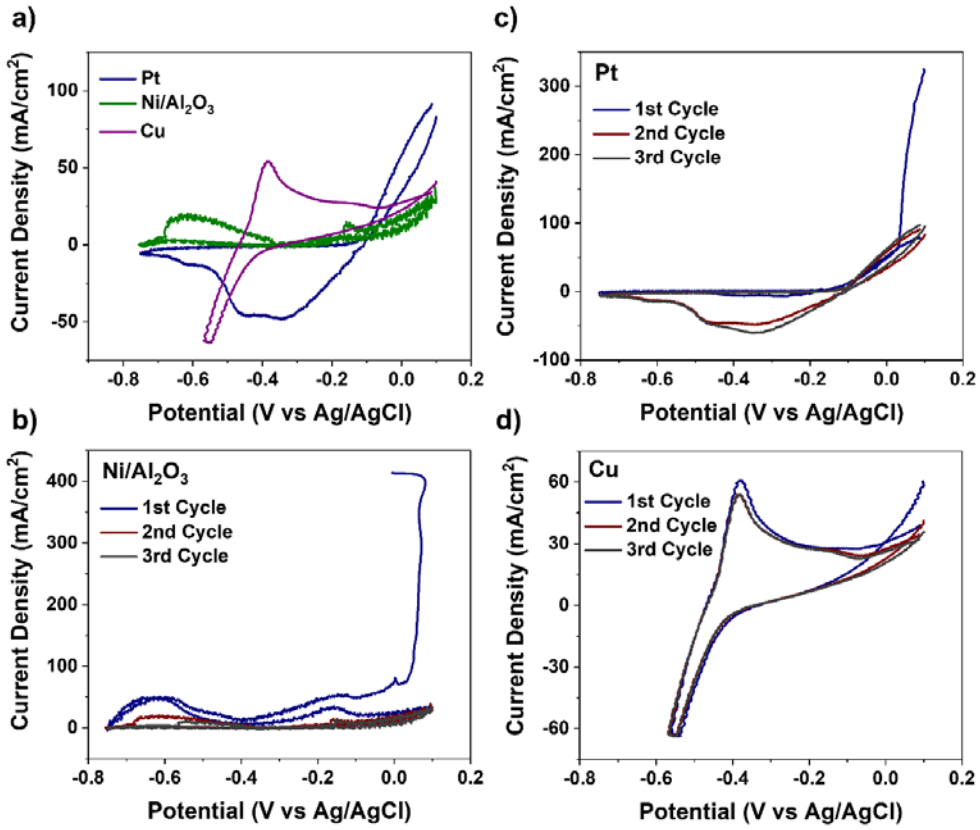

Figure 2.7 Cyclic voltammograms at 10 mV/s with a pseudo-reference Ag/AgCl electrode, 5 nm Fe on stainless steel counter electrode, and a) 1st cycle of Pt, Ni/Al_2O_3, and Cu working electrodes, and three cycles at 10 mV/s of working electrodes b) Ni/Al_2O_3, c) Pt, and d) Cu.

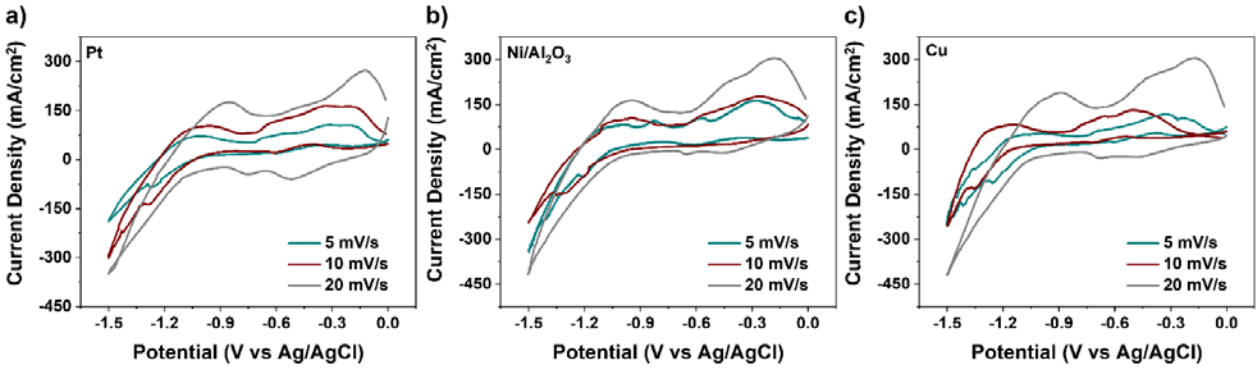

Figure 2.8 Cyclic voltammograms with pseudo Ag/AgCl reference electrode and 5 nm Fe on stainless steel working electrode at rates of 5, 10 and 20 mV/s with different counter electrodes of a) Pt, b) Ni/Al_2O_3, and c) Cu.

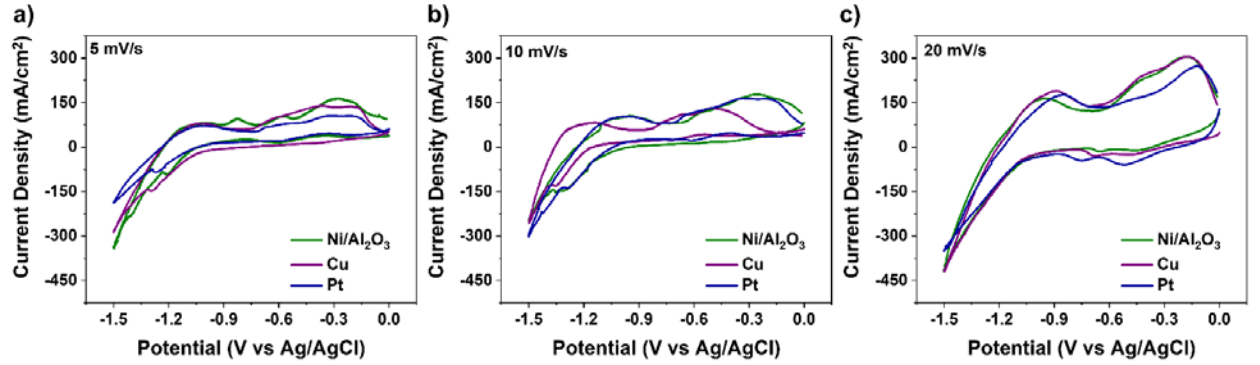

Figure 2.9 Cyclic voltammograms of the first cycle of each scan for a pseudo Ag/AgCl reference electrode, 5 nm Fe on stainless steel working electrode, Pt, Ni/Al_2O_3, or Cu counter electrode at rates of a) 5 mV/s, b) 10 mV/s, c) 20 mV/s.

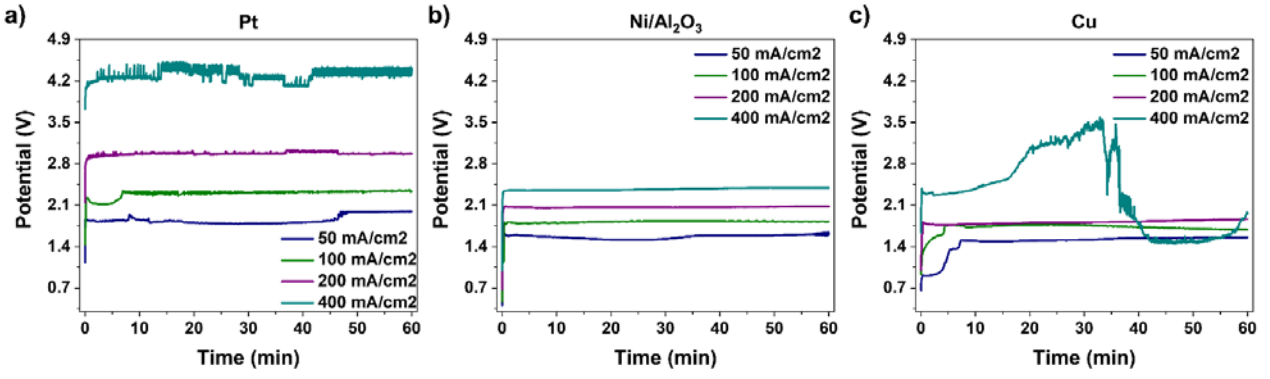

Figure 2.10 Voltage profiles for constant current electrolysis at 50, 100, 200, and 400 mA/cm^2 using a 5 nm Fe on stainless steel cathode and anode of a) Pt, b) Ni/Al_2O_3, and c) Cu.

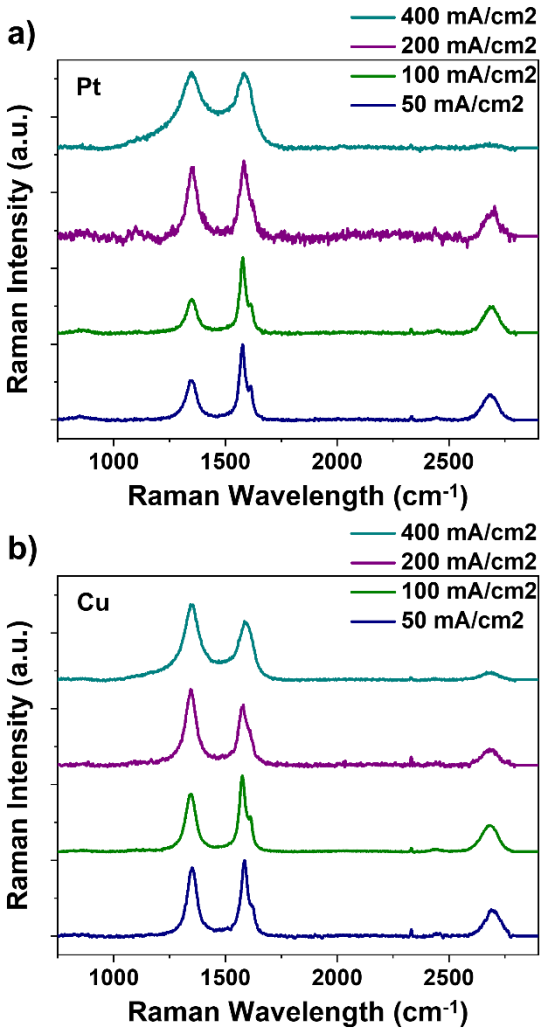

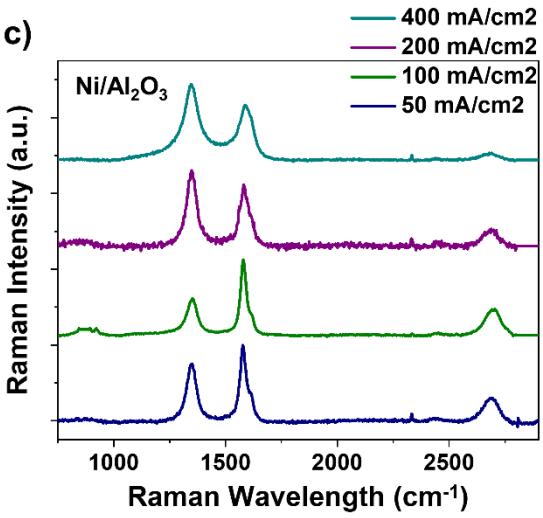

d)

Current Density (mA/cm^2)	D:G		
	Pt	Ni/Al_2O_3	Cu
50	.52	.8	1.09
100	.44	.75	0.9
200	.93	1.23	1.25
400	1.01	1.39	1.34

Figure 2.11 Raman spectra of carbon grown at 50, 100, 200, 400 mA/cm^2 current density using a 5 nm Fe on stainless steel cathode and anode of a) Pt, b) Cu, c) Ni/Al_2O_3, and d) a table of the D:G ratio at each current density for different anode materials used.

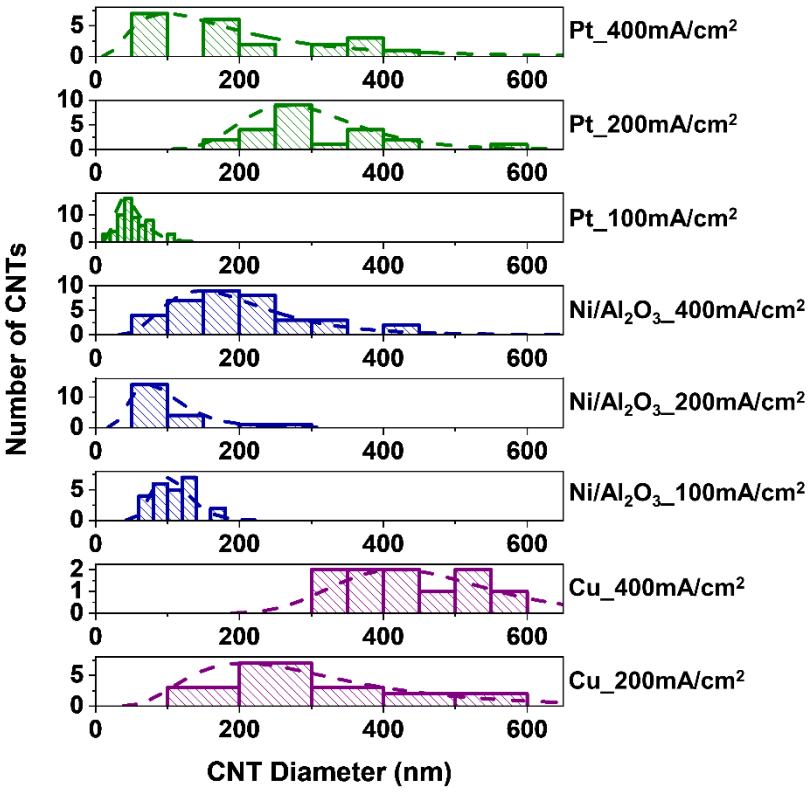

Figure 2.12 Histograms of size distribution of CNT diameters from CNT growth conditions using a 5 nm Fe on stainless steel cathode with different anode materials and different current densities with normalized lognormal distributions.

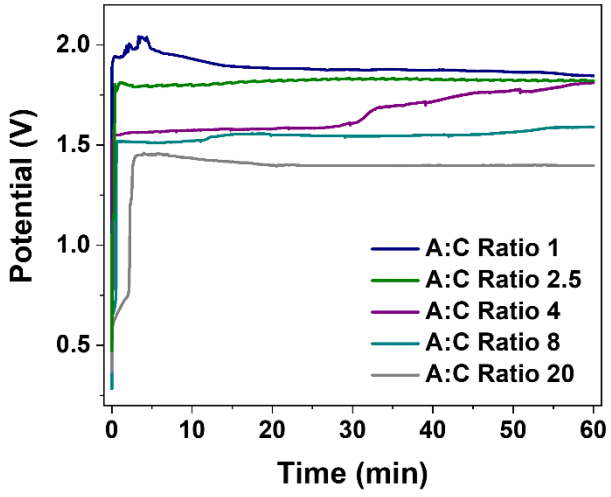

Figure 2.13 Voltage profiles for anode:cathode surface area study using a 5 nm Fe on stainless steel cathode and Ni/Al_2O_3 anode.

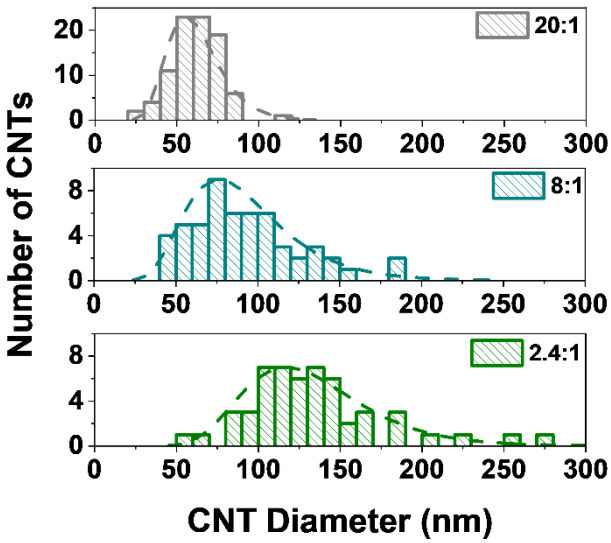

Figure 2.14 Histograms of CNT diameter distributions for CNTs grown at 100 mA/cm^2 with 5 nm Fe on stainless steel cathode and Ni/Al_2O_3 anode with anode:cathode surface area ratios of 2.4:1, 8:1, and 20:1.

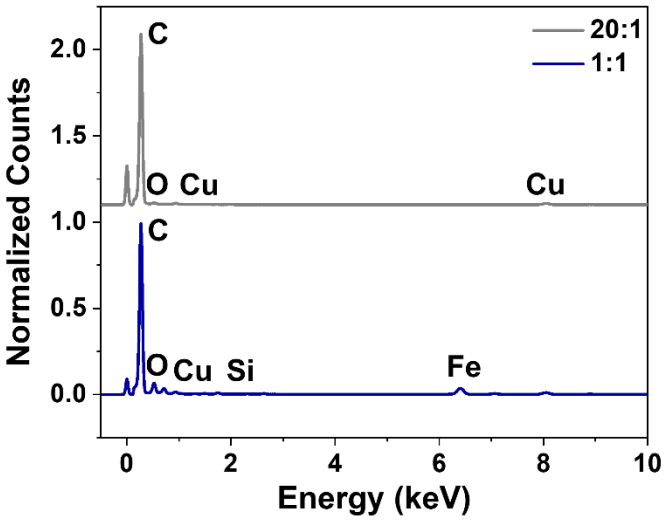

Figure 2.15 Complete STEM-EDS spectra for carbon grown at 100 mA/cm^2 with a Ni/Al_2O_3 anode and 5 nm Fe on stainless steel cathode with an anode:cathode surface area ratio of 1:1 and 20:1.

Chapter 3

Electrophoretic Deposition of $LiFePO_4$ onto 3-D Current Collectors for High Areal Loading Battery Cathodes

Adapted from: K. Moyer, R. Carter, T. Hanken, A. Douglas, L. Oakes, C.L. Pint, "Electrophoretic Deposition of $LiFePO_4$ onto 3-D Current Collectors for High Areal Loading Battery Cathodes," Materials Science & Engineering: B, 241, 42-47 (2019).

3.1 Introduction

Lithium-ion batteries (LIBs) have been a modern-day foundation for existing and emerging technological systems due to their benefits of durability and high energy density.[58, 59] One of the biggest challenges for the LIB manufacturing community is to simultaneously enable lower cell-level cost and improve specific energy density.[2, 60-62] Over 80% of the total costs of making high performance LIBs comes from the expense of materials and materials processing, and this places a large burden on manufacturing methods to command scalability, throughput, and cost footprint either comparable or better than current manufacturing approaches.[63-65] The challenge to improve mass specific performance amidst manufacturing limitations have led to cell-level modifications, such as thinning separator materials, with adverse safety implications.[66] Whereas a significant community of researchers is studying the design and discovery of new electrode materials, it is similarly important to consider new methodologies and manufacturing methods that can overcome bottlenecks for existing LIB chemistries.

In this regard, one route for improved packaging considerations in LIB devices is to transition planar collector materials to 3-D collector materials[67-73] which decreases inactive packaging mass without implications to safety or operation of the device. For example, given the change in geometry, a mesh or fibrous Al or Cu current collector with the same thickness as conventional planar current collectors could reduce the total collector material mass in a LIB by > 40%. Given that ~ 15% of total battery mass is attributed to packaging from excess inactive collector material,[74] this could yield over 15% improvement in specific energy density, which is significant for LIB systems. However, conventional manufacturing methods such as slot-die casting are not well-suited for such a challenge, since these techniques are optimized for planar surfaces.[75-77] This opens the door to new methods for manufacturing 3-D coatings, and electric field-directed methods with this capability such as electrospinning[78-80] or electrophoretic deposition[81, 82] remain excellent candidates.

Specifically, EPD has been an area of significant emerging research due to the ability to controllably fabricate coatings of nano- and microstructures on a wide variety of different functional surfaces.[31-33, 83] Unlike conventional processing routes, EPD allows for controlled mass deposition across the total exposed surface area of a conductive electrode that can satisfy the high throughput required for conventional manufacturing processes. EPD has been a key technique used in the design of electrodes for a range of energy storing devices such as supercapacitors, lithium ion, and lithium sulfur batteries, and lithium oxygen batteries[84-89] and used for coating 3-D surfaces.[90] One critical challenge of any manufacturing technique is the capability to match or surpass the areal loading and areal capacity of conventional manufacturing methods, since high areal loadings maximize the ratio of active energy storage materials to inactive packaging material in the battery needed to achieve high cell-level energy density.[91] Furthermore, conventional

manufacturing methods, such as slot-die coating, require a high solids content in the solvent for fabrication of thick electrodes which increases the viscosity, preventing quick and facile electrode coating. When fabricating thick electrodes *via* EPD, the deposition bath maintains a low viscosity while the coating itself has a high weight percent of solid material that does not impede electrode fabrication.

In this report, we utilize EPD as a technique to produce a stable $LiFePO_4$ cathode with high areal loading of ~ 20 mg/cm^2 of active material using a 3-D carbon cloth current collector. Compared to $LiCoO_2$, which is the benchmark for LIB cathodes, $LiFePO_4$ is non-toxic and overcomes cost limitations of a Co-containing cathode,[92] whereas the 3-D carbon cloth collector provides a flexible current collector framework. Our work demonstrates EPD as a viable technique for the manufacturing of electrodes from 3-D current collector templates, enabling processing routes compatible with cheaper, less-toxic solvent processing and more versatile control needed for lower cost and higher performing LIBs.

3.2 Experimental Details

3.2.1 Electrophoretic Deposition of $LiFePO_4$

$LiFePO_4$ powders (MTI), conductive carbon black,[93, 94] Super C45 (MTI), and nontoxic xanthan gum binder, abbreviated as XG in this work,[95-97] (Sigma Aldrich) were used to produce cathode materials. Composite solutions of 0.5 mg/mL and 5.0 mg/mL $LiFePO_4$ in ethanol (200 Proof, Decon Laboratories) were prepared with the ratio of components $LiFePO_4$/C45/XG = 100/10/2.5. Then, the $LiFePO_4$ composite was prepared using EPD onto fibrous carbon cloth[90, 95-99] (Fuel Cell Store). A two- electrode configuration of 1 cm^2 carbon cloth and an aluminum foil counter electrode with a separation of 0.5 cm was used. A Labview-operated Keithley 2400

Sourcemeter was used to apply a voltage of 100 V to the system for 10 minutes to deposit the $LiFePO_4$ composite on the carbon cloth.

3.2.2 Materials Characterization and Electrochemical Testing

A Malvern Zetasizer Nano ZS instrument was used to obtain the zeta potential and particle size measurements of all solutions. The structure, morphology, and elemental analysis of the deposited film was characterized by a Zeiss Merlin scanning electron microscope. To investigate $LiFePO_4$ as a cathode material, coin cells were fabricated with the EPD $LiFePO_4$ composite films as the cathode material. In the coin cell, Li metal was used as the counter and reference electrode, the liquid electrolyte was 1.0 M lithium hexafluorophosphate (Sigma Aldrich, 98%) ethylene carbonate (Sigma Aldrich, 98%) -diethyl carbonate (Sigma Aldrich, 99%) (1:1 by volume), and Celgard 2400 polypropylene separators were used. A Metrohm Autolab multichannel testing system was used for electrochemical testing.

3.3 Results and Discussion

To explore the use of EPD to produce cathode materials on flexible 3-D current collectors, we used three different mass loadings (Figure 3.1) labeled as low (2 mg/cm^2), medium (10 mg/cm^2), and high (20 mg/cm^2), respectively (Figure 3.2a). Here we use flexible, lightweight carbon cloth for scaling to flexible energy storage devices with improved energy density. All cathode materials underwent EPD for ten minutes and the low mass loading films were deposited from $LiFePO_4$

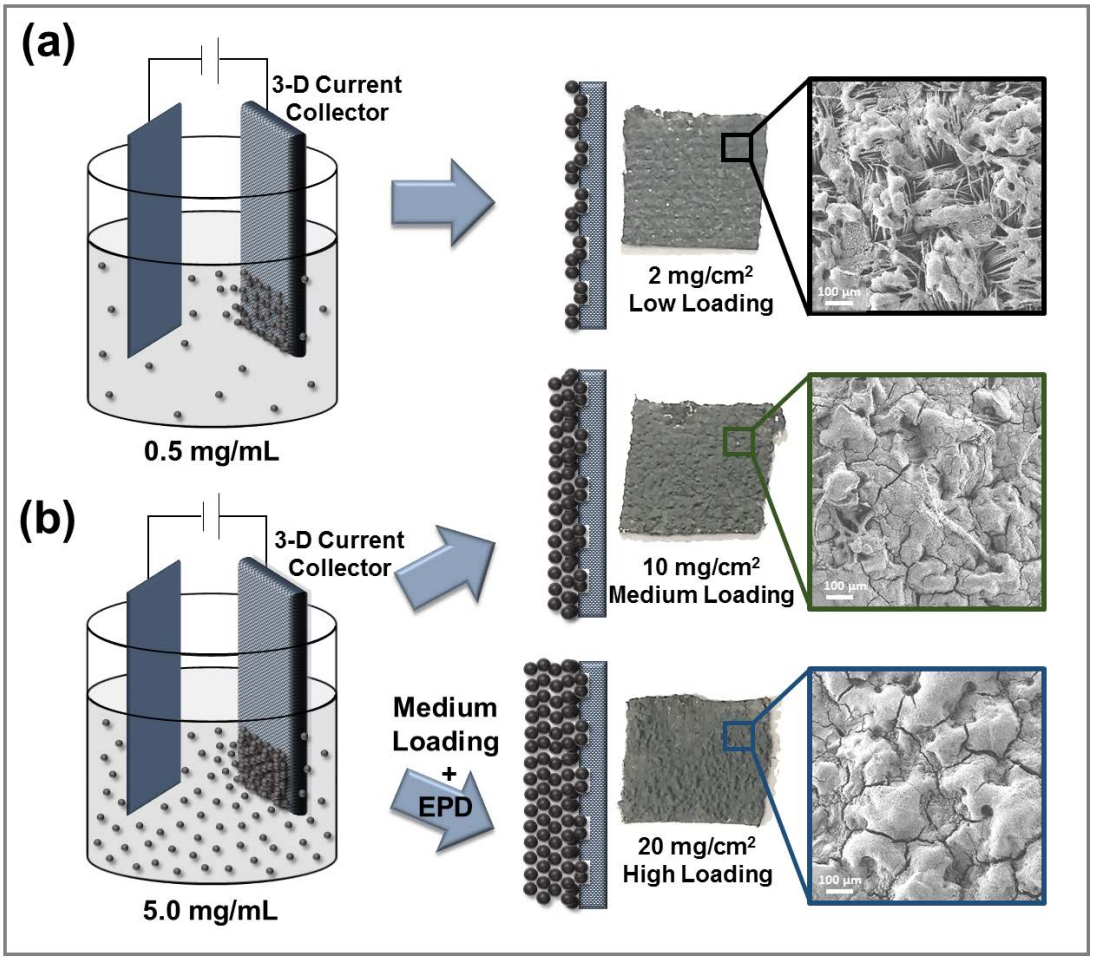

Figure 3.1 Electrophoretic deposition of $LiFePO_4$ on a three-dimensional carbon cloth current collector to achieve variable mass loadings at two different solution concentrations (a) Low mass loadings from 0.5 mg/mL solution and (b) Medium and high mass loadings from 5.0 mg/mL solution.

composite solution of 0.5 mg/mL and both the medium and high mass loading films were deposited from $LiFePO_4$ composite solution of 5.0 mg/mL. To achieve a $LiFePO_4$ film with medium mass loading, a depositing solution with concentration 5.0 mg/mL was used. Then, to achieve the high mass loading film of 20 mg/cm^2, the film underwent EPD two times in the 5.0 mg/mL depositing solution for ten minutes each.

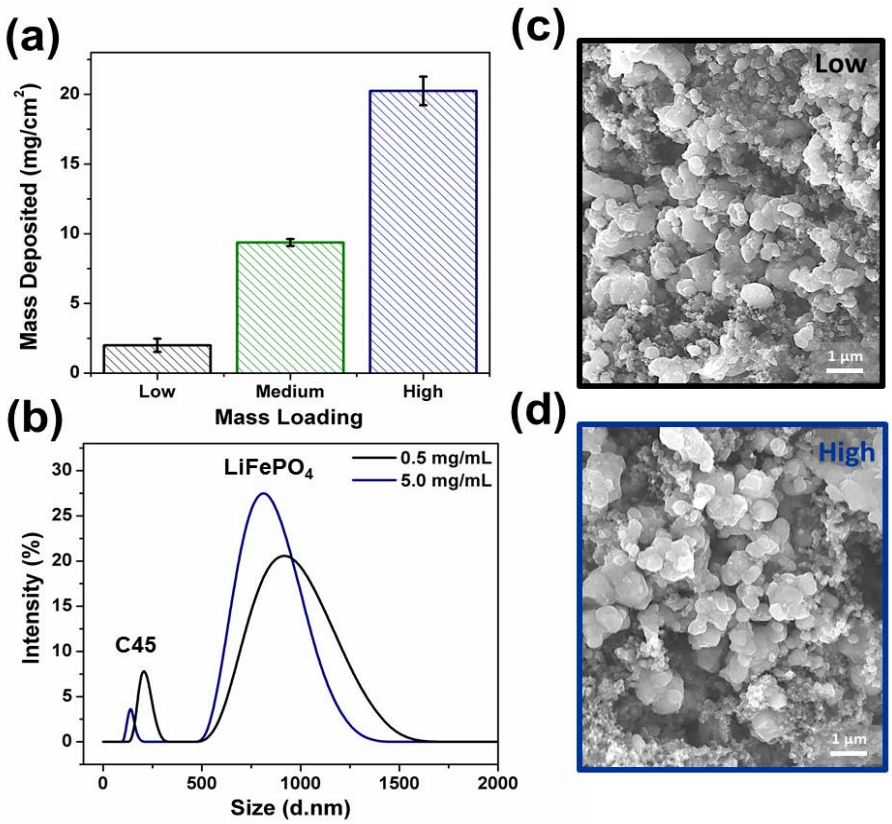

Figure 3.2 Electrophoretic deposition can be used on a three-dimensional current collector to achieve (a) Variable mass loadings with low and high areal densities. The particle size of the $LiFePO_4$ and C45 being deposited is (b) Very similar regardless of depositing solution concentration and the morphology and size of the deposited material appears the same for all films (c) Low and (d) High mass loadings.

Particle size characterization based on the measured hydrodynamic diameter indicated particles of $LiFePO_4$ and conductive carbon black (C45) in both the 0.5 mg/mL and 5.0 mg/mL solutions were approximately the same at ~ 1 µm $LiFePO_4$, matching that on the supplier's website implying no particle aggregation, and ~ 0.25 µm C45 (Figure 3.2b). However, the particle diameter of xanthan gum (XG) was significantly smaller than this and undetectable by the Malvern Zetasizer. Film characterization by scanning electron microscopy (SEM) generally confirms the particle sizes of $LiFePO_4$ and C45 obtained from the Zetasizer hydrodynamic diameter

measurements and shows that at higher magnification the morphology of $LiFePO_4$ is the same for all the films, independent of the depositing solution concentration used (Figure 3.2c-d).

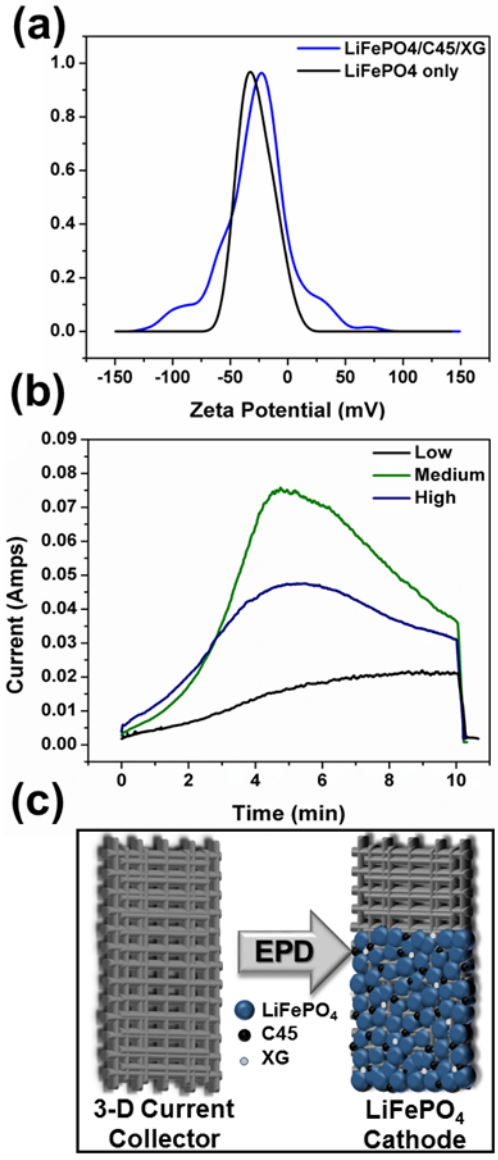

Figure 3.3 (a) Zeta potential of the composite $LiFePO_4$/C45/XG solution and $LiFePO_4$ only solution in ethanol (b) current profiles for the deposition of the low, medium, and high mass loading films for the 10-minute deposition time at which the electrodes were removed from the solution (c) assembly of full $LiFePO_4$ cathode.

Electrophoretic mobility measurements were performed to obtain the zeta potential of the $LiFePO_4$ solution to better understand the deposition conditions (Figure 3.3a). In order to confirm

that the zeta potential of the solution did not change upon addition of C45 and XG binder to the $LiFePO_4$ in ethanol solution, the zeta potential of the $LiFePO_4$ only solution and $LiFePO_4$/C45/XG solution are compared and both have a zeta potential of ~ -30.0 mV. The as received $LiFePO_4$ particles are carbon coated, contributing to having a similar mobility to carbon black. The current profiles were used to electrochemically monitor the EPD environment during deposition for each type of full cathode film fabricated (Figure 3.3b) and the assembly via EPD of each film yielded a full cathode composed of $LiFePO_4$, C45, and XG particles (Figure 3.3c). Following the fabrication of cathodes using EPD coated $LiFePO_4$, 2032 coin cells were fabricated by soaking the electrode and separator in electrolyte, and crimping the cell. These devices were then tested for their

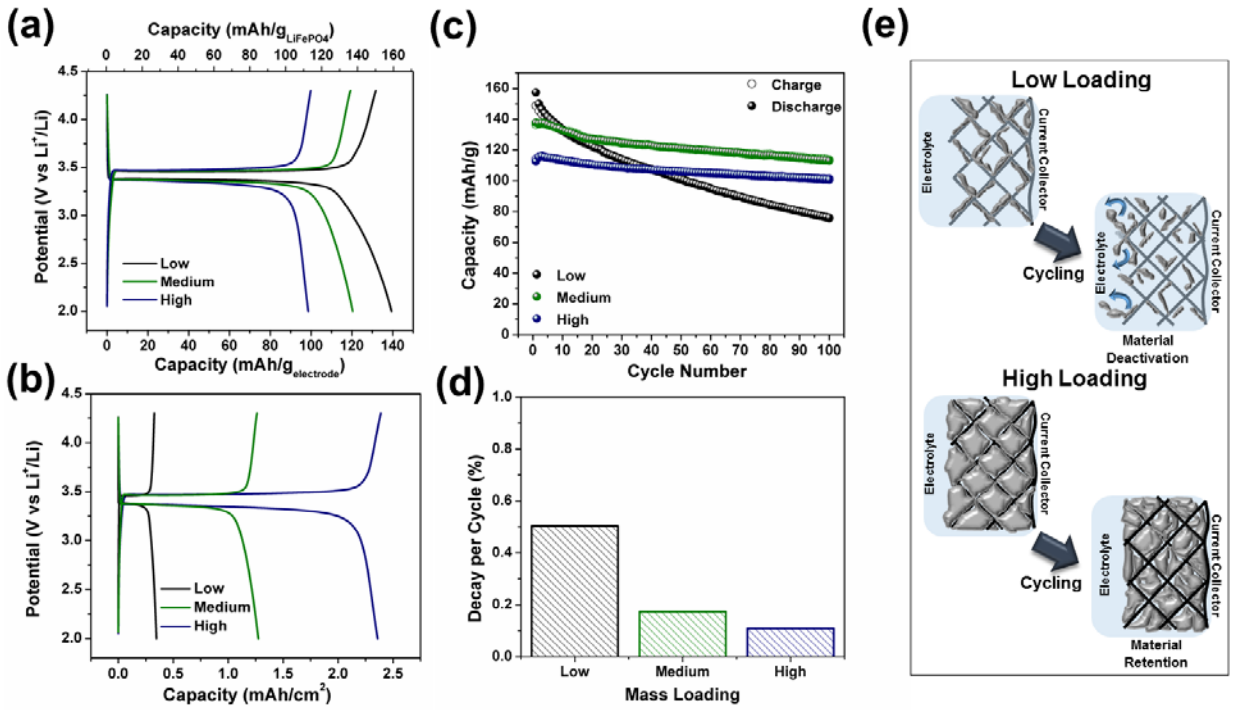

Figure 3.4 Electrochemical tests of $LiFePO_4$ on 3-D carbon cloth current collectors as lithium-ion battery cathodes. Galvanostatic charge discharge at a rate of 0.1C of (a) The specific capacity of the first cycles for low, medium, and high mass loading films normalized to the $LiFePO_4$ active mass and composite electrode, (b) The areal capacity of the first cycles for low, medium, and high mass loading films, (c) Cycling performance at 0.1C for 100 cycles of low, medium, and high mass loading films and (d) Corresponding decay rates and (e) Material deactivation and material retention of the 3-D current collector.

performance utilizing galvanostatic charge -discharge measurements. Notably, the long and stable voltage plateau associated with $LiFePO_4$ is evident at all mass loadings (Figure 3.4a). When the electrode mass is normalized to the active mass of $LiFePO_4$, the voltage profile reveals a capacity for the low loading film of ~ 160 mAh/$g_{LiFePO4}$, medium loading film of ~ 140 mAh/$g_{LiFePO4}$, high loading film of ~ 110 mAh/$g_{LiFePO4}$ at the expected operating voltage range (3.4 V – 3.6 V). Even though the specific capacity slightly decreases with increased mass loadings, the high mass loading film exhibits a much larger areal capacity of 2.40 mAh/cm^2 compared to that of the medium and low mass loading films of 1.30 mAh/cm^2 and 0.35 mAh/cm^2, respectively (Figure 3.4b). Notably, the device with the greatest areal capacity yields areal performance competitive with conventional manufacturing methods. However, whereas a significant portion of the cost in conventional LIB manufacturing is associated with NMP processing, this EPD methodology employs fast-drying ethanol as a solvent, which can decrease the total energy required for cathode processing by significantly reducing solvent drying and recovery which can make up >12% of electrode processing costs, and hence lowering this processing cost proportionally.[100] This implies that EPD onto 3-D current collectors can yield performance that meets or exceeds the areal capacity of conventional manufacturing processes while enabling routes to use solvents that can significantly decrease processing time and cost, such as ethanol.

To understand the differences in the durability of 3-D current collectors processed with coatings of $LiFePO_4$ cathode materials, devices with all three mass loadings prepared in this study were cycled at a rate of 0.1 C for 100 cycles (Figure 3.4c). Our findings support the overall observation that the 3-D current collector enhances the stability of cathodes prepared with higher mass loadings, yielding decay per cycle < 0.11% (Figure 3.4d) and corresponding Coulombic

efficiencies can be found in Figure 3.9. Devices prepared with 2.0 mg/cm^2 areal loading exhibited 0.5% decay per cycle, which indicates significant performance loss. We attribute this observation

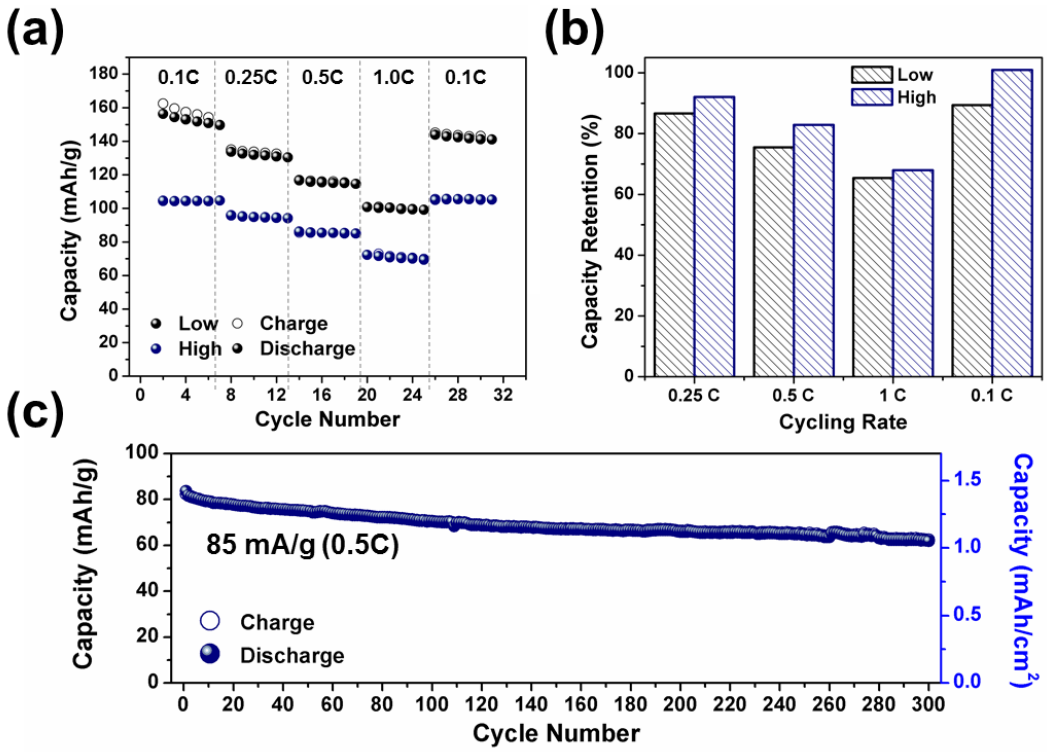

Figure 3.5 (a) Rate performance of the low and high mass loading $LiFePO_4$ 3-D carbon cloth electrode system at the specified rates, (b) Corresponding capacity retention for each system at each cycling rate, and (c) Durability measurements based on galvanostatic charge discharge at 0.5C over 300 cycles.

to the fact that the low-loading material framework involves $LiFePO_4$ particles that are only topically adhered to the current collector surface. Upon cycling, volume change associated with lithium extraction and insertion cause shear stress at the $LiFePO_4$/current collector interface, facilitating delamination of the active material. However, at higher loadings, the thicker layer of $LiFePO_4$ becomes "wedged" into crevices in the 3-D current collector architecture, and shear-stress induced delamination of active material becomes less likely. This implies a unique structure-

property relationship correlating cathode stability and current collector microstructure that could be important for the practical design of improved LIB devices.

To better understand these results, the electrochemical performance of $LiFePO_4$ cathodes produced at different loadings with EPD are further examined in a rate study comparing the stability and decay of $LiFePO_4$ at rates of 0.1 C, 0.25 C, 0.5 C, and 1.0 C (Figure 3.5a), where 0.1 C corresponds to 17 mA/g. As the rate is increased, the high mass loading films exhibit greater capacity retention than the low mass loading film at each current density rate (Figure 3.5b). Upon returning to cycling at a rate of 0.1 C, the high mass loading films exhibit ideal capacity retention whereas the low mass loading films only retain ~90% capacity that we attribute to the decay mechanism illustrated in Figure 3.4e and corresponding Coulombic efficiencies can be found in Figure S6c. To further examine the capacity retention of the high mass loading films, cycling at 0.5 C over duration of 300 cycles demonstrates excellent stability and average areal capacity of ~1.20 mAh/cm^2 (Figure 3.5c). This demonstrates the capability of EPD to produce $LiFePO_4$ cathodes directly into 3-D current collector geometries with the stability and areal performance necessary to be competitive for LIB processing.

3.4 Conclusion

The findings of this work support the underlying premise of this study that (1) EPD is an effective method to prepare cathodes with high areal capacity competitive with or better than conventional manufacturing methods on 3-D current collectors, (2) EPD enables the use of solvent processing that relieves the low-throughput and energy-intensive NMP processing steps of conventional battery manufacturing, and (3) EPD enables straightforward processing $LiFePO_4$ cathode materials into high areal capacity networks to overcome costly Co-containing cathode

materials currently utilized for LIBs. This work solidifies EPD as a competitive manufacturing technique for LIB devices with lower packaging weight and hence improved cell-level specific and volumetric energy.

Acknowledgments

The authors acknowledge Nitin Muralidiharan, Keith Share, Adam Cohn, Andrew Westover, and Mengya Li for helpful discussions, Dmitry Koktysh for his training K.M. on the Malvern Zetasizer Nano ZS instrument, and the laboratory facilities of Rizia Bardhan. This work was supported in part by NSF grant CMMI 1400424, A.D., K.S., and A.P.C. were supported by NSF graduate fellowships under grant 1445197, and R.C. acknowledges support from a graduate fellowship provided by the Vanderbilt Institute of Nanoscale Science and Technology.

3.5 Appendix

$LiFePO_4$ Solution Characterization

In order to determine the optimum electrophoretic deposition (EPD) conditions for $LiFePO_4$ in ethanol, zeta potential measurements using a Malvern Zetasizer Nano ZS instrument were taken at various solution pH. Solutions of 0.5 mg/mL $LiFePO_4$ (MTI) in ethanol (200 Proof, Decon Laboratories) were prepared and tuned to a range of pH; 2.73, 5.09, 8.98, 10.35, 12.70. The zeta potentials are plotted as a function of pH in Figure S1a, a distribution of the zeta potential for each solution pH can be found in Figure S1b, and the $LiFePO_4$ hydrodynamic diameter can be viewed in Figure S1c. Using this information and testing each solution via EPD, the solution of pH 10.35, zeta potential ~ -30.0 mV, resulted in the optimum deposition conditions for the $LiFePO_4$ system.

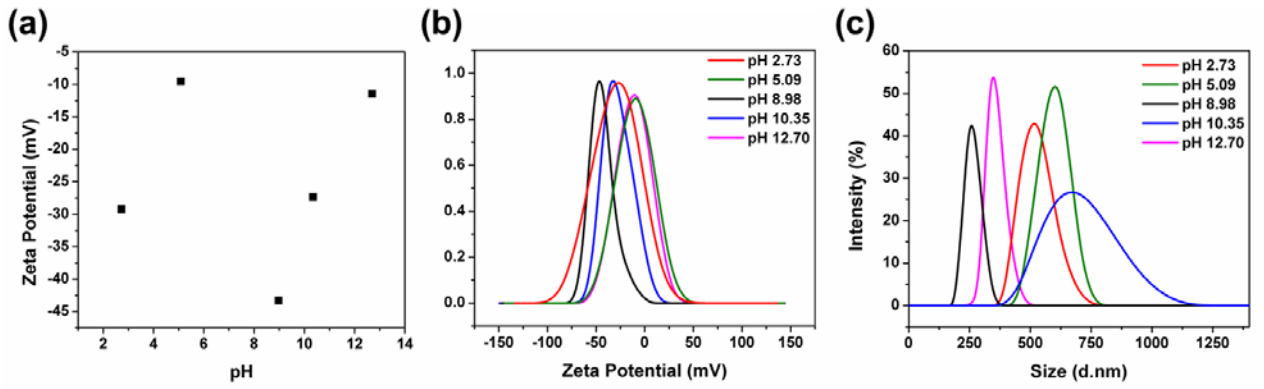

Figure 3.6 (a) Zeta potential vs pH, (b) Zeta potential distribution, and (c) Size distribution of $LiFePO_4$ in ethanol at various pH.

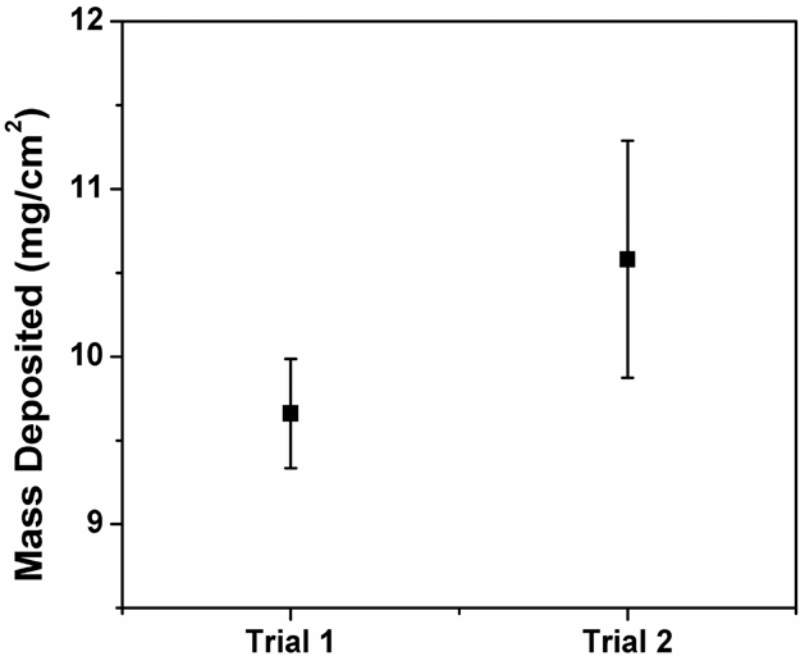

Figure 3.7 Mass deposited for each EPD trial for high mass loading films to achieve a total mass deposition of 20 mg/cm^2.

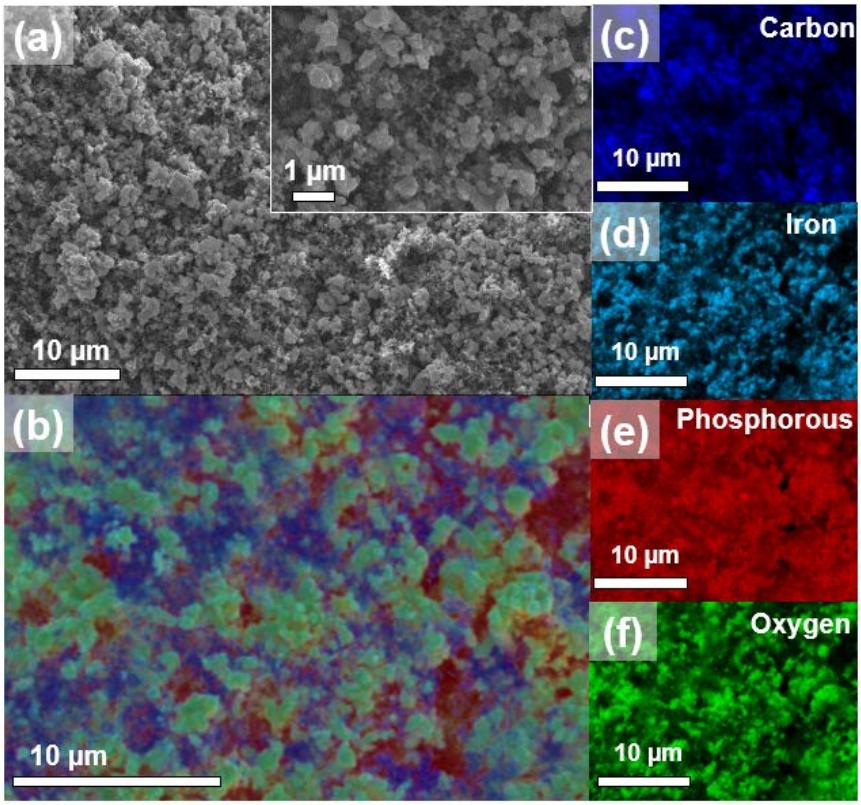

Figure 3.8 (a) SEM image of the $LiFePO_4$ composite deposited on carbon cloth with inset of higher magnification image of $LiFePO_4$ spherical particles and (b) EDS elemental map and corresponding elements (c) Carbon, (d) Iron, (e) Phosphorous, and (f) Oxygen.

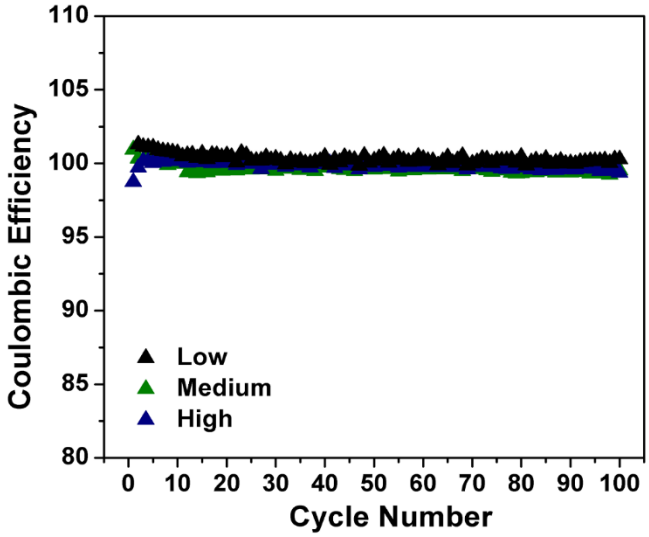

Figure 3.9 Coulombic efficiencies of the low, medium, and high mass loading films cycling at 0.1C (17 mA/g) for 100 cycles.

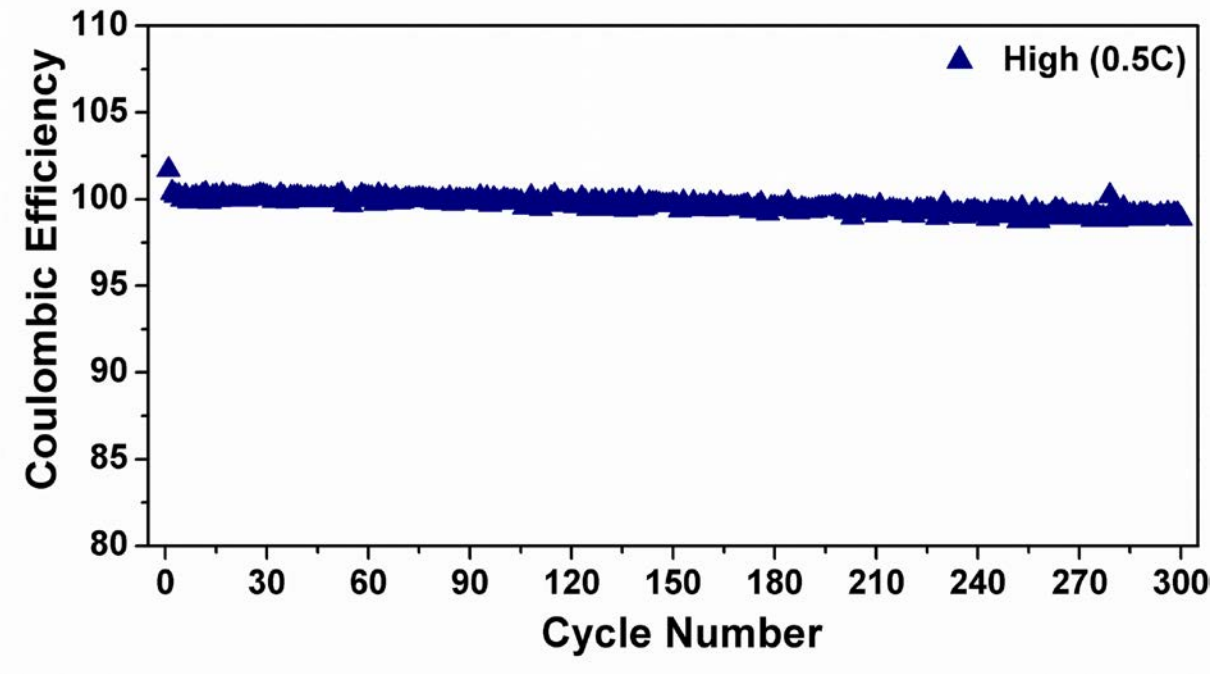

Figure 3.10 Coulombic efficiencies of the high mass loading film at an increased rate of 0.5C (85 mA/g) for 300 cycles.

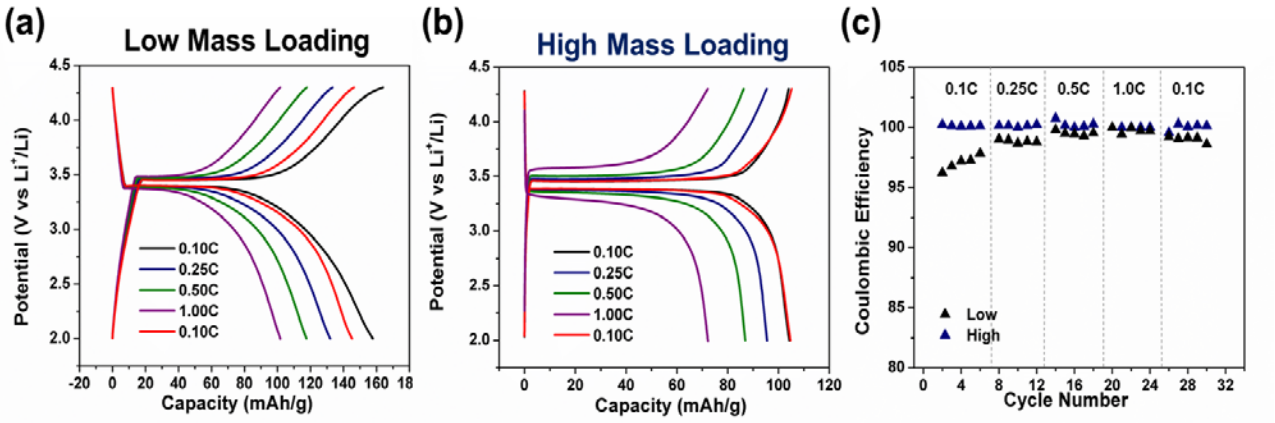

Figure 3.11 Galvanostatic charge discharge of the first cycles of each current density of the rate study for (a) Low and (b) High mass loading films and their (c) Coulombic efficiencies at each specified rate.

Chapter 4

Electrophoretic Deposition as a Manufacturing Strategy for High Areal Capacity Cathodes

Adapted from: K. Moyer, R. Carter, K. Share, T. Hanken, L. Oakes, C.L. Pint, "Electrophoretic Deposition as a Manufacturing Strategy for High Areal Capacity Cathodes," *in preparation.*

4.1 Introduction

Over the past decades, the cost of electrochemical energy storage of lithium ion batteries (LIBs) has dramatically increased along with the annual world energy consumption.[101, 102] More than 90% of the energy and cost required for manufacturing high energy LIBs lies within materials cost and production.[103] While the cost of materials fabrication remains a prominent issue, the standards and performance metrics of LIBs also continue to demand improvement. Among the many requirements for enhanced LIBs, energy density is one of the most critical parameters.[104-107]

In order to achieve the energy density and sustainable performance necessary for the next generation of technology, it is critical to understand how to overcome the current barriers and limitations of electrode design. Several parameters contribute to engineering high energy density battery electrodes, such as mass loading, porosity, and ratio of inactive to active materials within the electrode.[108-110] Electrode mass loading is a critical factor in electrode design that substantially contributes to the energy density of the battery.[111, 112] Higher mass loadings can significantly reduce inactive packaging mass, minimizing the ratio of inactive to active components which consequently increases the energy density of the total battery system.[113-115]

Engineering an approach to produce high energy density batteries while reducing the inactive material in the system is a necessary solution to solve this two-pronged problem. Previous attempts to achieve higher areal loadings for increased energy density have been reported, but are oftentimes labor intensive, incompatible with current manufacturing strategies, and unable to perform at higher rates >0.2 C.[114, 116, 117] Various current collector materials have also been investigated to achieve higher mass loadings to increase energy density, such as three-dimensional metal foams.[105] However, this current collector architecture has proven to be difficult to integrate into calendaring processes and conventional slot die battery casting. Standard battery cathode fabrication typically consists of making a slurry of active material with conductive additive and binder in an organic solvent, usually n-methylpyrrolidone (NMP), which is then processed through a slot die caste onto a planar metal foil current collector and undergoes an energy intensive drying process to yield a positive electrode with mass loading around 10 - 20 mg/cm^2.[118] It is difficult to achieve uniform, crack-free, high mass loading electrodes beyond 10 - 20 mg/cm^2 with current slot die manufacturing capabilities on planar current collectors without the use of multiple additives and surfactants.[119, 120] Consequently, there is a demand for manufacturing strategies that enable high areal loading without sacrificing electrochemical performance.

Electrophoretic deposition (EPD) is an alternative manufacturing technique that allows for simultaneous, uniform deposition of all electrode components directly onto a current collector at various mass loadings.[121] EPD has been previously demonstrated as a means to make many different types of LIB technologies over a range of electrode types and morphologies.[84, 87, 122-124] EPD can be used to produce compact films, as it is analogous to gravity sedimentation, and can be used to make electrodes from thin films[125] to high mass loading architectures[126, 127] that surpass current areal loadings. Not only is EPD highly versatile and can support a range of materials, but

it requires simple equipment and is scalable to allow for a large throughput,[128] making it an excellent route to achieve high areal loading electrodes for high energy density LIBs while maintaining high rate capability.

Driven by an electric field through solution assembly, a variety of different solvents may be used for EPD, ranging from aqueous to alcohol to organic based mediums.[129] Acetone is a common solvent used for EPD and is significantly less expensive and less toxic than NMP, which is used in conventional battery manufacturing.[130, 131] Aqueous processing has been explored as an alternative to using NMP as a solvent, however agglomeration and inferior wetting of the current collector materials make it difficult to yield a uniform, crack-free electrode material.[119] Using acetone as the solvent significantly eliminates the costly and energy intensive recovery step of NMP and the electrode drying time is drastically reduced. The compatibility with a variety of solvents also allows for co-deposition of a variety of materials within the same solution.[132] Several cathode materials, such as lithium cobalt oxide, nickel manganese cobalt, and lithium iron phosphate (LFP), are currently the benchmark positive electrode battery materials, however LFP shows the best compatibility with water based solvents[111] and is nontoxic, stable, environmentally friendly[81] and boasts a theoretical capacity of 170 mAh/g[133]. Unfortunately, one drawback to LFP is its low electrical conductivity,[134] but this challenge is solved through the addition of conductive carbon additive to the electrode.

In this work, we use multiwall carbon nanotubes (MWCNTs) to enhance the electrode conductivity. Carbon nanotubes (CNTs) boast excellent tensile strength, have a low density, and offer desirable electronic properties to create an electronically conductive pathway and porous network throughout the entire electrode,[86, 135-137] enabling high rate capability. A common technique to process CNTs is dispersion in a solvent[138] and EPD of CNTs has repeatedly been

reported as a straightforward method to deposit CNTs on a variety of substrates.[123, 139-141] When deposited in conjunction with LFP, MWCNTs facilitate the formation of high areal loading electrodes on planar current collectors by creating a compact yet porous, electrically conductive electrode network.

Here, we demonstrate EPD as a scalable approach to fabricate LFP cathodes with high areal loadings of ~50 mg/cm^2 on a planar current collector architecture. Acetone is used as the solvent throughout the deposition which eliminates NMP from the fabrication process. This highlights EPD as a route towards aqueous and alternative solvent processing to greatly reduce the cost of electrode manufacturing.[119, 130] In this report, we demonstrate EPD as a manufacturing strategy to fabricate electrodes with high energy density and rate capability.

4.2 Experimental Details

4.2.1 Electrophoretic Deposition

Cathode materials were made from LFP powders (MTI), MWCNT 8-15 nm outer diameter (CheapTubes, > 95 wt%), and xanthan gum (Sigma-Aldrich). 8 mg/mL LFP solutions for EPD were prepared in acetone (Fisher Scientific, 99.8%) with the following ratio of components LFP/MWCNT/XG (100:1.25:2.1875). EPD was performed using a Keithley 2400 Labview-operated sourcemeter by applying a 200 V bias for 10 minutes to a two-electrode arrangement with a separation of 0.5 cm between a 1 cm^2 aluminum foil electrode and a stainless-steel counter electrode. Each 10-minute trial deposited ~10 mg/cm^2 onto the planar Al foil current collector. Electrodes were allowed to dry after each trial and depositions were repeated five times to yield a total areal loading of ~50 mg/cm^2.

4.2.2 Materials Characterization

Deposition solutions were characterized using a Malvern Zetasizer Nano ZS instrument to determine the particle size distribution and zeta potential. Measurements of the LFP/MWCNT/XG deposition solution along with LFP only, and MW only solutions were obtained (Figure S1). The particle size distribution, morphology, and structure were further examined by a Zeiss Merlin scanning electron microscope.

4.2.3 Electrochemical Testing

Coin cells were assembled using the LFP EPD fabricated electrodes as the cathode, 2500 Celgard polypropylene separators, and Li foil (Sigma-Aldrich, 99.9%) as the counter and reference electrode. 1.0 M lithium hexafluorophosphate (Sigma-Aldrich, >99.99%) 1:1 by volume ethylene carbonate (Sigma-Aldrich, 98%) – diethyl carbonate (Sigma-Aldrich, 99%) was used as the electrolyte. Electrochemical testing was performed on an eight-channel MTI battery testing system.

4.3 Results & Discussion

In order to demonstrate EPD as a means to manufacture nanoarchitecture electrodes, LFP cathodes with a high areal loading of ~50 mg/cm^2 were fabricated (Figure 4.1a). Increasing the areal capacity by fabricating electrodes with mass loadings greater than those of conventional manufacturing (>10 mg/cm^2) significantly increases the energy density (Figure 4.1b).[142, 143] In addition, as the active cathode material loading increases, the ratio of inactive to active material within the electrode decreases, specifically the separator, current collectors, and housing (Figure 4.1c). Consequently, this technique is promising to achieve high areal capacity electrodes with the capability to increase the overall energy density.

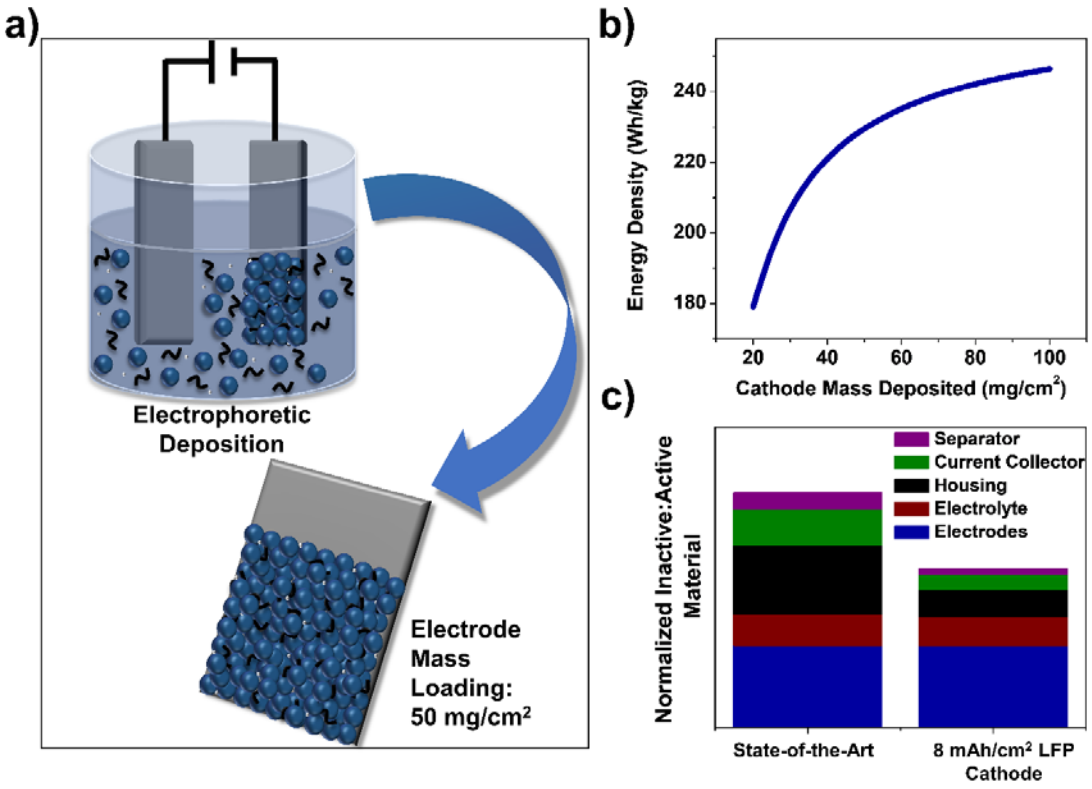

Figure 4.1 a) Scheme demonstrating EPD as a manufacturing strategy that can be used to fabricate high areal loading electrodes, b) relationship between energy density and amount of cathode mass deposited, and c) normalized ratio of inactive:active material for different cathode loadings.

EPD was employed to fabricate high areal capacity electrodes. At the beginning of the EPD process the depositing solution was dark in color, but after the ten-minute deposition in which a voltage bias was applied, the solution was clear, indicating complete deposition of all particles from solution (Figure 4.2a, b). The hydrodynamic particle size distribution of the particles ranges from ~ 0.5 µm for the LFP particles to ~4-6 µm for the MWCNTS (Figure 4.2c). The co-deposition of LFP, MWCNTs, and XG creates an interconnected conductive network in which the MWCNTs wrap around the LFP particles creating an electronically conductive pathway throughout the size distribution of individual and all components in solution, d) SEM image of LFP particles surrounded by an electrically conductive network of MWCNTs.

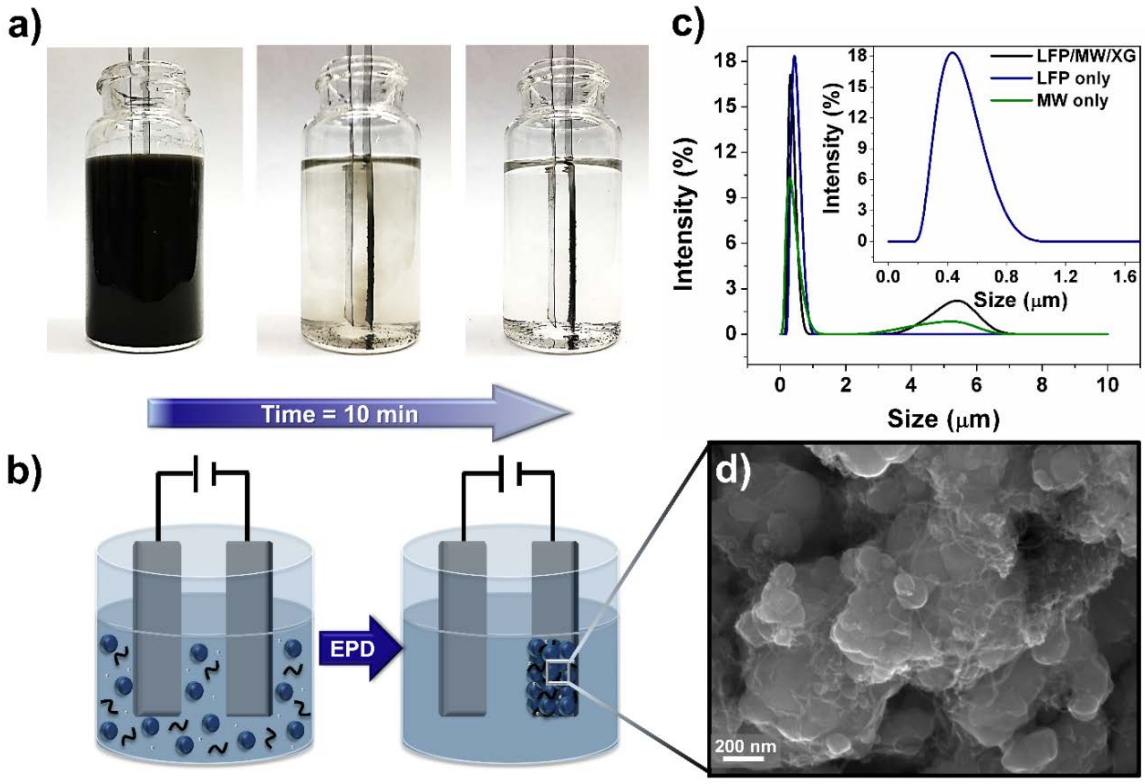

Figure 4.2 a), b) During the EPD process the depositing solution starts out at its respective concentration and appears very dark in color and overtime, the solution turns clear indicating that all particles in solution have been deposited on the working electrode, c) hydrodynamic particle electrode (Figure 4.2d).

The addition of MWCNTs also helps to create a more porous structure throughout the electrode to facilitate ion transport. One limitation of high areal loading is reduced ion transport throughout the entire electrode which often results in the inability for high areal capacity electrodes to perform at high rates.[144, 145] As the mass loading per unit area increases, there is considerably more material to penetrate, making it harder for the ions to access all the material. Therefore, the addition of MWCNTs via EPD is highly desirable to create a more porous structure that aids ion transport throughout the high mass loading electrodes, enabling performance at high rates, up to 2C.[135]

While a porous structure is necessary to achieve ion transport throughout the electrode, optimization of porosity is crucial to maximize energy density.[146] Electrode porosity is commonly reduced through calendaring processes to increase the battery energy density, however it is critical not to over-decrease the porosity of high areal loading electrodes and create a barrier to ion transport. In this work, the total thickness of the electrode is approximately 510 µm, yielding a porosity of ~33%. This porosity is on par with the reported metrics of current battery

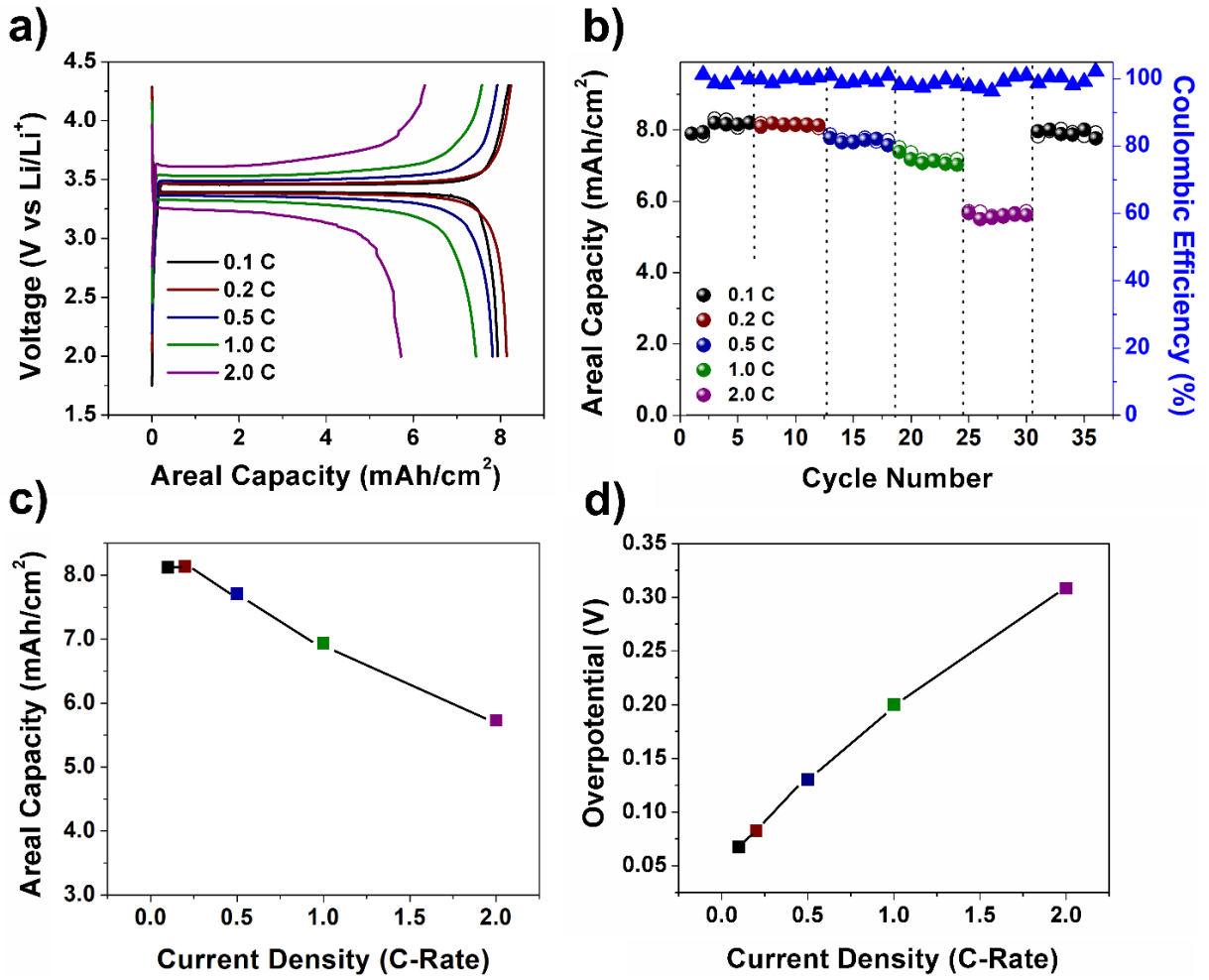

Figure 4.3 Galvanostatic testing of EPD LFP electrodes a) The areal capacities for the first cycles of each specified rate, b) The areal capacities and specific capacities during a rate study, c) The average areal capacity at each tested current density, d) The increasing overpotential with increased current density.

manufacturing and those desirable for high energy density.[104, 146]

To assess the electrochemical performance of the high areal capacity cathodes, a rate study was performed at current densities of 0.1, 0.2, 0.5, 1.0, and 2.0 C (Figure 4.3). The charge-discharge curves of the first cycle at each current density (Figure 4.3a) illustrate areal capacities as high as 8 mAh/cm^2 at rates of 0.1 and 0.2 C and slowly decrease with increased current density; 7.7 mAh/cm^2 at 0.5 C, 6.9 mAh/cm^2 at 1 C and 5.73 mAh/cm^2 at 2 C (Figure 4.3b, c). The high areal capacity is further highlighted over 100 cycles at current densities of 0.1 and 0.5 C (Figure 4.4a-c). The cycling performance shows capacity retention of 88.8% at 0.1 C and 79% at 0.5 C over 100 cycles with areal capacities greater than 7 and 6 mAh/cm^2 after cycling, respectively.

When comparing our work from this study with other fabrication techniques and high areal performances reported to date, it was observed that most of the high areal capacities that had been reported were tested at rates of C/10 (Figure 4.4d). Various techniques such as EPD,[81, 121, 126, 140] and doctorblading,[108, 113, 134, 144] and other methods[115, 131, 147-149] have shown promise as manufacturing techniques to fabricate high areal capacity cathodes, however, when tested electrochemically, these cathodes did not perform at rates as high as 2C. Figure 4.4e is a plot comparing the amount of active material deposited and the corresponding areal capacity at rates at 2C, showing the areal capacity reported in this work, is one of the highest reported to date that comments on the active material loading and areal capacity at rates as high as 2C.[108, 144, 147, 149] Literature has also demonstrated that high mass loadings can be attained by creating cellulose or textile, CNT mixtures as scaffolds for filling with electrochemically active material.[147] While this technique yields high areal capacities due to the large areal loadings, it requires more time and step-intensive processes, such as high pressure cellulose homogenization coupled with vacuum assisted infiltration and the use of NMP as a solvent along with multiple drying steps. The

fabrication technique highlighted in this work uses EPD as a low-cost approach using non-toxic solvent materials to yield cathodes with some of the highest areal capacities while maintaining rate capability at rates as high as 2C.

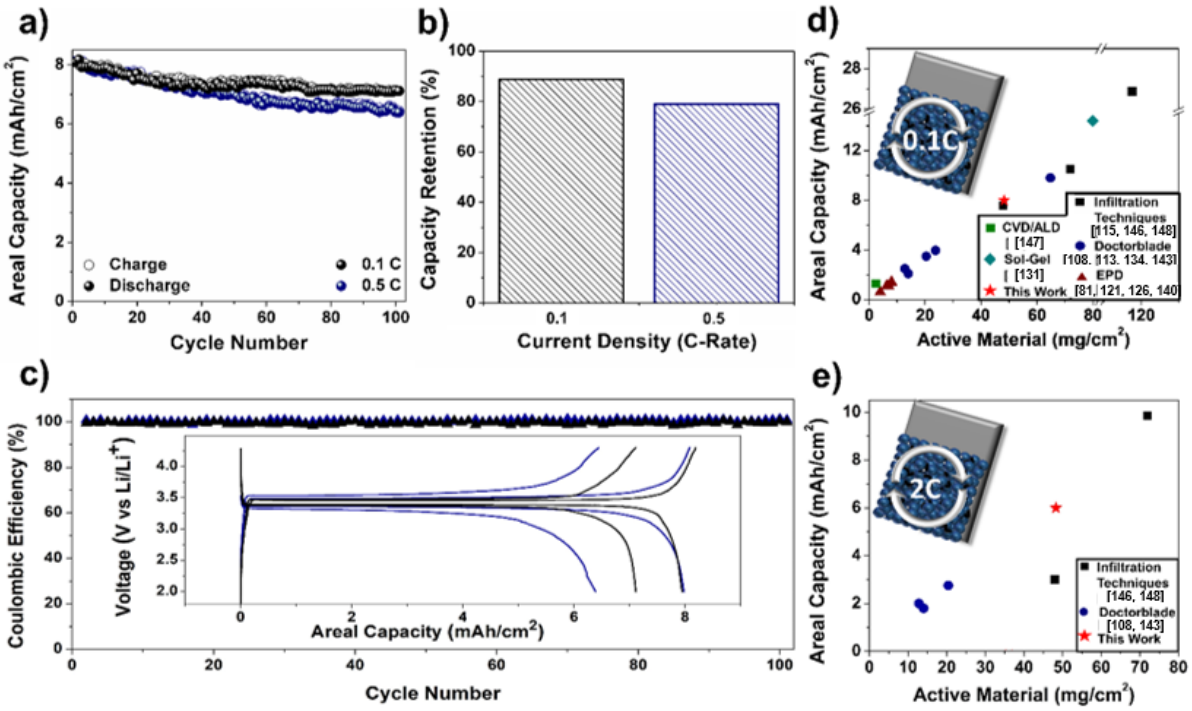

Figure 4.4 a) Extended cycling performance at current densities of 0.1 and 0.5 mA/cm^2, b) Capacity retention of each current density, c) Areal capacity of first and last charge-discharge cycles at current densities of 0.1 and 0.5 mA/cm^2 and corresponding coulombic efficiencies, Literature comparison to date of areal capacity versus electrode mass loading active material at rates of d) 0.1C and e) 2C.

4.4 Conclusion

In this study, EPD offers many benefits to electrode manufacturing and is highly scalable. Using acetone as the solvent minimizes the energy required for the drying steps in-between deposition and increasing the areal loading to ~50 mg/cm^2 significantly reduces the battery materials cost ($/kWh) while simultaneously enhancing the energy density while maintaining rate capability. EPD as a fabrication technique yields high areal loading electrodes with areal capacities

of a resounding 8 mAh/cm^2 that demonstrates cycling stability over a range of current densities while maintaining areal capacities >5.5 mAh/cm^2 at rates as high as 2 C. Overall, EPD is an alternative, cost-effective method to synthesize high energy density cathodes with high areal capacities.

Acknowledgments

The authors acknowledge Adam Cohn, Anna Douglas, Mengya Li, Nitin Muralidiharan, and Kody Wolfe for helpful discussions, Dmitry Koktysh for his training K.M. on the Malvern Zetasizer Nano ZS instrument, and the laboratory facilities of Rizia Bardhan. This work was supported in part by NSF grant CMMI 1400424, K.S. was supported by NSF graduate fellowships under grant 1445197, and R.C. acknowledges support from a graduate fellowship provided by the Vanderbilt Institute of Nanoscale Science and Technology.

4.5 Appendix

Solution Characterization

A Malvern Zetasizer Nano ZS instrument was used to determine the zeta potential of the solutions to optimize the electrophoretic deposition (EPD) conditions. Solutions of combined and individual components were made in acetone. A combined solution of lithium iron phosphate (LFP), multiwall carbon nanotubes (MWCNTs), and xanthan gum (XG), LFP/MWCNT/XG (100:1.25:2.1875) was made, a solution of MWCNT only was made, and a solution of LFP only was made. The xanthan gum particles are soluble in acetone and undetectable by the Malvern Zetasizer so these particles were not tested individually. The concentrations of individual solutions were the same concentration of the individual components in the combined solution. The goal of this experiment was to make sure that the zeta potential of the LFP solution did not change with addition of MWCNT and XG components.

Porosity Calculation

Porosity was calculated by evaluating the difference between the actual electrode density and theoretical electrode density by the following equation:

$$Porosity = \frac{T - S(\frac{W_{LFP}}{D_{LFP}} + \frac{W_{MWCNT}}{D_{MWCNT}} + \frac{W_{XG}}{D_{XG}})}{T}$$

Where T is the electrode thickness (cm), not including the aluminum current collector, S is the weight deposited per unit area (g/cm^2), W is the weight percent of material, D is the density of each material (g/cm^3).

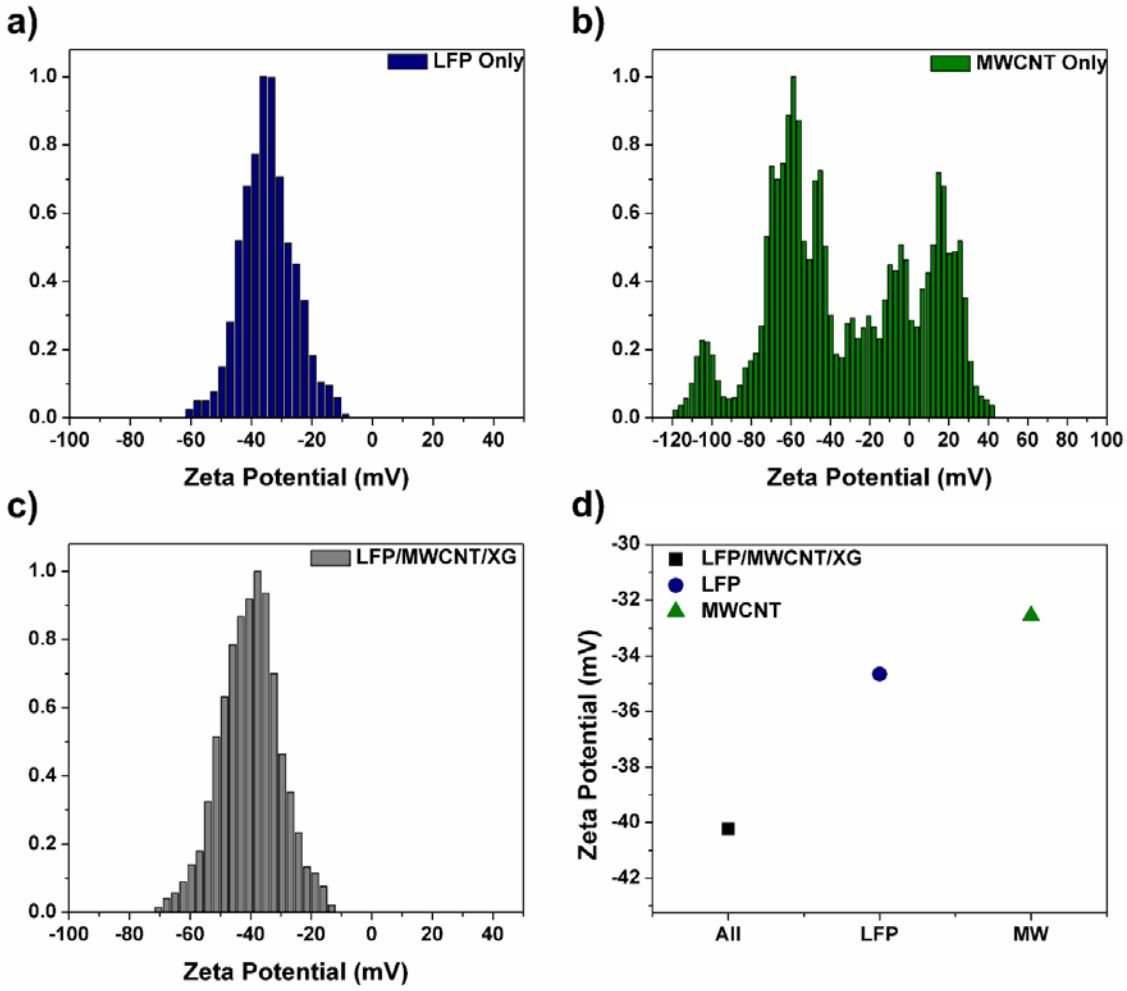

Figure 4.5 Zeta potential of a) LFP only solution, b) MWCNT only solution, c) LFP/MWCNT/XG combined solution, and d) summary of zeta potentials.

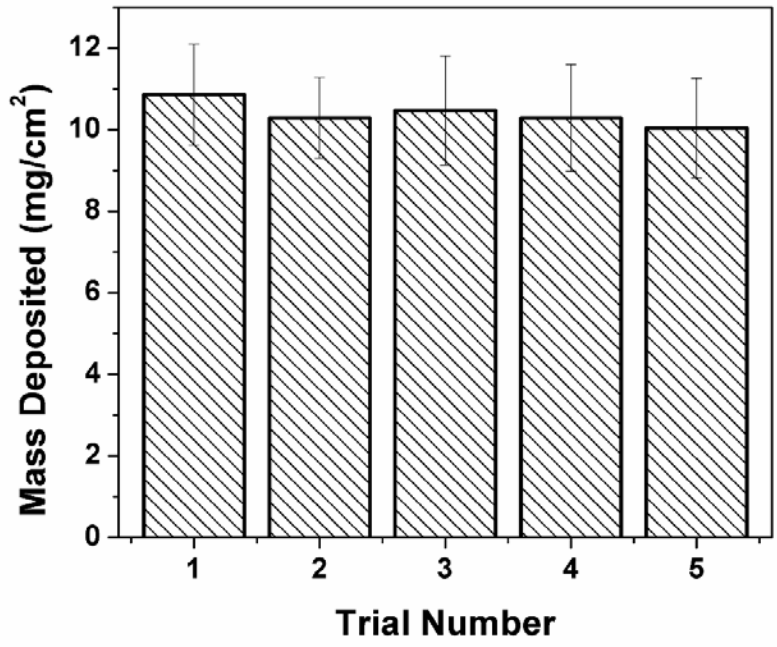

Figure 4.6 Mass deposited of LFP/MWCNT/XG solution on working electrode during each EPD trial to achieve a total mass loading of 50 mg/cm^2.

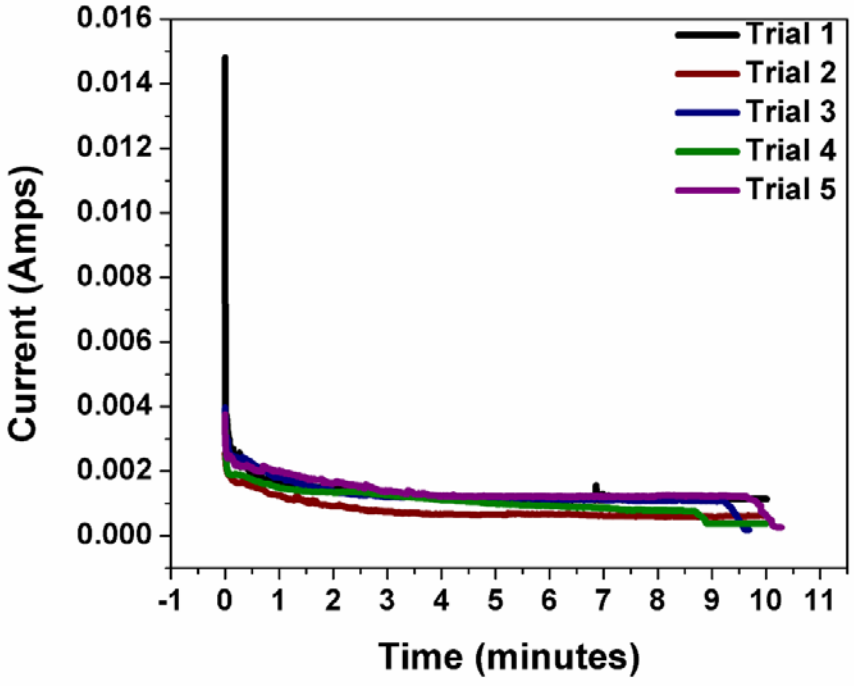

Figure 4.7 Current profile of each 10 minute EPD trial of LFP/MWCNT/XG solution.

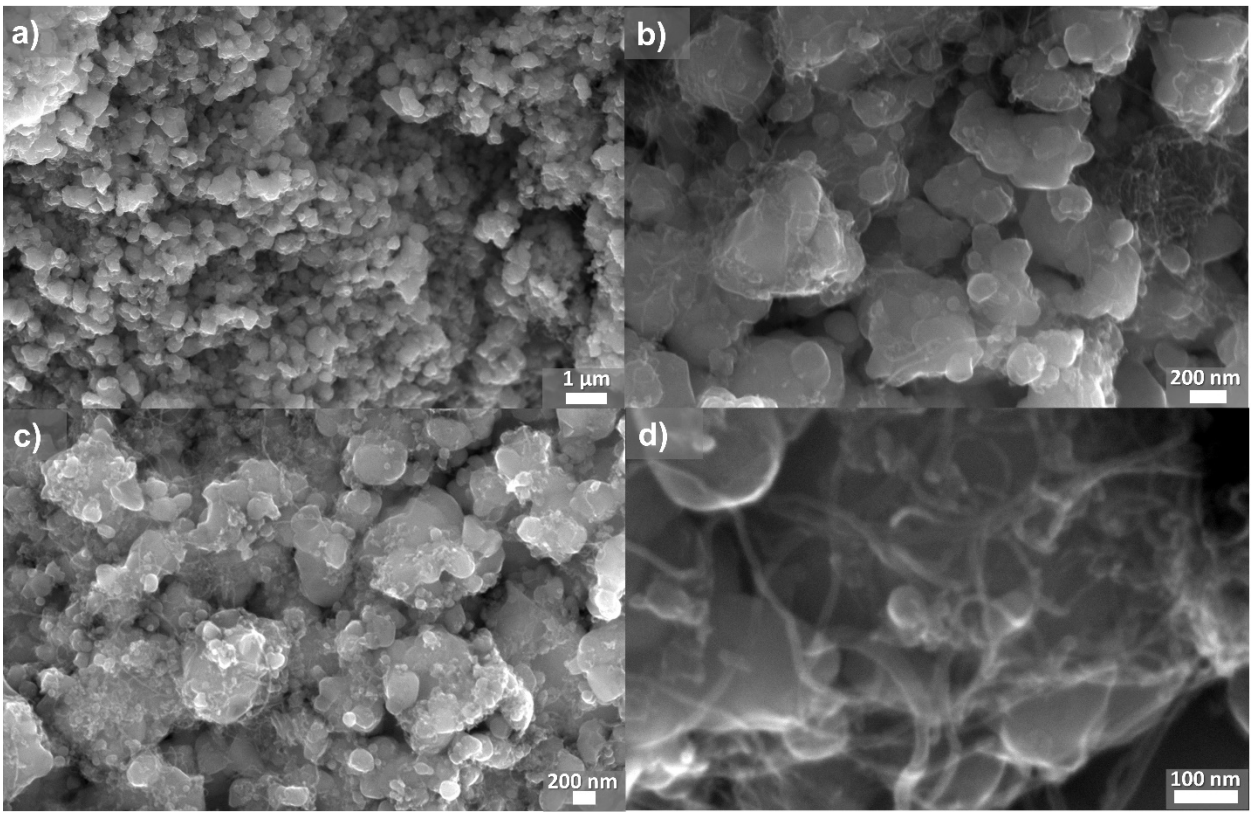

Figure 4.8 SEM images of deposited LFP/MWCNT/XG at different magnifications.

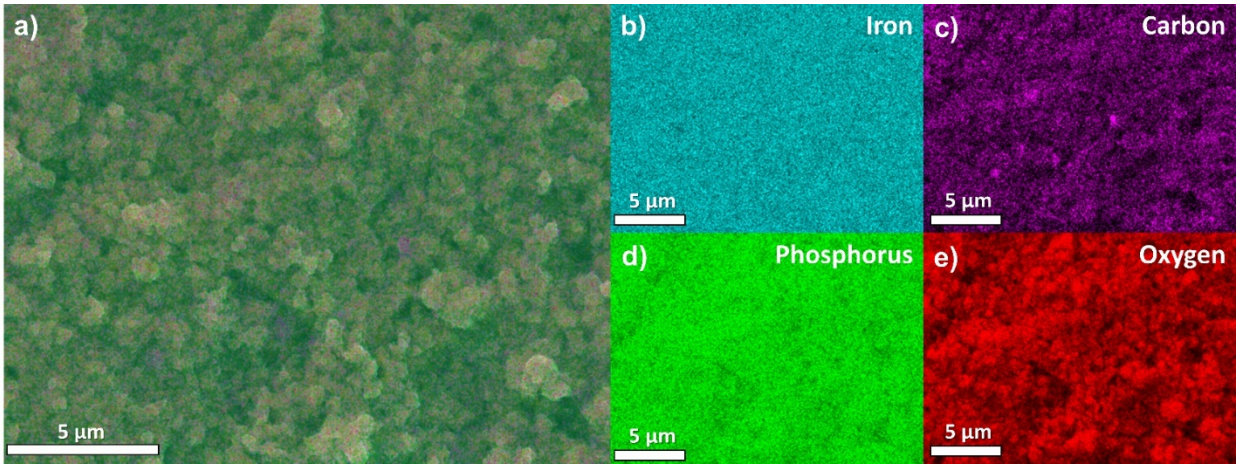

Figure 4.9 Deposited LFP/MWCNT/XG a) EDS elemental map and corresponding elements, b) iron, c) carbon, d) phosphorus, e) oxygen.

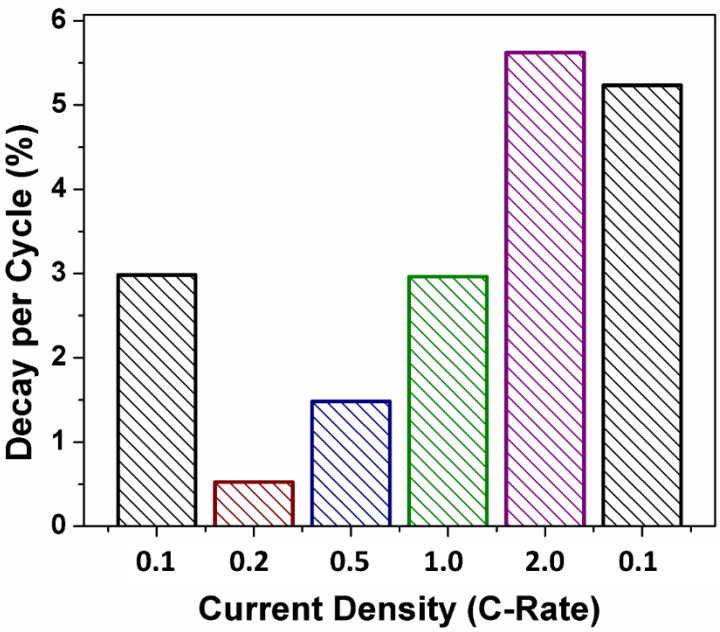

Figure 4.10 Decay per cycle of each current density of the rate study in Figure 4.3.

Chapter 5

High-Rate Potassium Ion and Sodium Ion Batteries by Co-Intercalation Anodes and Open Framework Cathodes

Adapted from: K. Moyer, J. Donohue, N. Ramanna, A.P. Cohn, N. Muralidharan, J. Eaves, C.L.Pint, "High-Rate Potassium Ion and Sodium Ion Batteries by Co-Intercalation Anodes and Open Framework Cathodes," Nanoscale, 10, 13335-13342 (2018).

5.1 Introduction

Whereas many applications, such as consumer electronics, can suffice with the energy and power density of conventional lithium-ion batteries, many future applications that will pivot on battery technology will demand faster charging times. This is especially true for numerous areas such as high power weaponry, EVs or drones conducting long distance travel, and robotics or other high power machinery.[150-152] To this regard, fast recharging and high power density is the focus of high power electrochemical supercapacitors, although even the most novel approaches in such systems remain limited to energy density many times lower than a battery due to electrolyte, cell packaging, and the nature in which charge is stored.[153-159] The energy stored per active site for a supercapacitor is much less compared to the energy stored per active site for a faradaic system. Similarly, pseudocapacitors and hybrid capacitors are largely centered on the use of aqueous electrolytes that may enable high power, but at the cost of energy density and commercially viable materials in a packaged device.[160-168] Therefore, there remains a significant need to design devices

that can boast the energy density competitive with a battery, but with fast charging capability and durability.

One of the key challenges in fast charging batteries is the diffusion kinetics of ions across the liquid-solid interface, and through the host insertion materials where they are stored. In the first case, this is associated with the de-solvation step of ion insertion into the host material, and in some cases, the diffusion of the ion through the solid-electrolyte interphase (SEI) region.[169] In anode materials such as graphite, the de-solvation of an alkali ion is the rate-limiting step for high power capability.[170] To address this, recent work has highlighted the mechanism of co-intercalation for both sodium (Na) and potassium (K) ions that leverages a solvent which chelates with the alkali metal ion where the solvent forms a shell around the ion.[171-179] This enables the insertion of the ion and solvent shell into a layered anode, such as graphite or multi-layered graphene, where the rate-limiting de-solvation process is mitigated and the weak ion-host lattice interactions facilitate ultrafast diffusion.[180, 181] Recent work has demonstrated extraordinary results for half-cell devices that utilize co-intercalation, with sodium boasting capacities exceeding 100 mAh/g for over 8000 cycles in nanostructured carbons, and charge times as low as 12 seconds,[182] and potassium demonstrating capacities up to 100 mAh/g with rate capability up to 30 second charge.[183] Whereas researchers have emphasized this mechanism to be transferrable across different ions and different high quality graphite-like materials, the bottleneck of co-intercalation studies to date remains the challenge of combining these half-cell studies into full-cell configuration that can exploit this high rate performance.

In this regard, separate research efforts have been focused on improving the performance of cathode materials. Prussian blue (PB) has been lauded as a promising battery cathode for high rate capability alternative ion chemistries due to its high theoretical capacity (170 mAh/g),[184] rigid,

open structure with large interstitial sites,[90, 185] and nontoxic nature and low cost,[186] which is advantageous for large scale applications. This metal organic framework[187] has a hexacyanometalate structure[188] with chemical formula $A_xM[M(CN)_6)]_{1-y}{\cdot}zH20$,[175] where A represents alkali ions (Na, K), $0<x<2$, and M represents transition metals. As observed by previous work, the use of iron as the transition metal to synthesize sodium/potassium hexacyanoferrate yields higher capacity and cycling stability compared with other PB analogues.[189] The rigid, open framework cathode structure[190, 191] has large interstitial sites which aid in accommodating corresponding changes in volume during cycling with low lattice strain,[192] and tunable, three-dimensional channels that allow for ion, and even molecule, insertion/extraction.[90, 193] As a result of the electrochemical practicality, there is a strong correlation between the structure of Prussian blue and performance making it an ideal cathode for high rate battery systems.[194-198]

In this work, we build from previous studies with an aim toward a synergistic cathode – electrolyte- anode battery configuration that leverages the open framework cathode structure and co-intercalation anodic mechanism into a high rate battery device. Our work demonstrates a broadly adaptable design strategy to tailor the performance of a battery to perform with energy density and cycling performance characteristic of a battery, but at high rates often limited to supercapacitors or pseudocapacitors. This enables a class of energy storage systems optimized for higher power applications, such as grid-storage, weaponry, power beaming, electric vehicles, among other next-generation application areas.

5.2 Experimental Details

5.2.1 Prussian Blue Synthesis

Sodium Hexacyanoferrate – Sodium Prussian Blue (NaPB): 3 mmol $FeCl_2 \cdot 4H_2O$ (Sigma-Aldrich, >99%) and 2.0 g $Na_3C_6H_5O_7 \cdot 2H_2O$ (Fisher Scientific) were added to 100 mL deionized water to make solution A and stirred until dissolved. 2 mmol $Na_4Fe(CN)_6 \cdot 10H_2O$ (Sigma-Aldrich, >99%) and excess of NaCl (Fisher Scientific, 99.8%) were added to 100 mL deionized water to make solution B and stirred until dissolved. Potassium Hexacyannoferrate – Potassium Prussian Blue (KPB): 3 mmol $FeCl_2 \cdot 4H_2O$ (Sigma-Aldrich, >99%) and 2.0 g $C_6H_5K_3O_7 \cdot H_2O$ (Sigma-Aldrich, >98%) were added to 100 mL deionized water to make solution A and stirred until dissolved. 2 mmol $K_4Fe(CN)_6 \cdot 3H_2O$ (Sigma-Aldrich, 98.5-102.0%) and excess of KCl (Sigma-Aldrich, 99.0-100.5%) were added to 100 mL deionized water to make solution B and stirred until dissolved. In both cases solution B was added to solution A and stirred for 4 hours. The composite solution was collected by centrifugation and the precipitate was dried at 100˚C overnight. Particle size, morphology, and composition was examined using SEM and EDS with a Zeiss Merlin scanning electron microscope. Material crystal structure was examined by x-ray diffraction using a Rigaku Smart Lab with a Cu Kα radiation source.

5.2.2 Electrode Fabrication

Graphite electrodes were fabricated by making a slurry of natural graphite powder (Alfa Aesar, 99.9995%), conductive carbon black (MTI), and PVDF binder (MTI, >99.5%) in the ratio of (80:10:10) and coated onto carbon coated aluminum (MTI, >99.9%). Similarly, Prussian blue electrodes were fabricated by making a slurry of the synthesized Prussian blue powder (either K- or Na- hexacyanoferrate), multi wall carbon nanotubes (CheapTubes, >95%), and sodium carboxymethyl cellulose (Sigma-Aldrich) in the ratio of (80:10:10) and coated onto carbon coated aluminum (MTI, >99.9%).

5.2.3 Coin Cell Assembly & Electrochemical Testing

Graphite half-cells were fabricated using the graphite electrodes as the working electrode with either Na (Strem Chemicals, 99.95%) or K (Sigma-Aldrich, 99.95%) metal as the counter and reference electrode. Prussian blue half-cells were made using the Prussian blue electrodes as the working electrode with either Na or K metal as the counter and reference electrode. Full-cells were assembled using the graphite electrodes as the anode and Prussian blue electrode as the cathode with a cathode to anode ratio of 1.6:1 by mass with cathode of 1.00 mg and anode of 0.625 mg. A 2325 Celgard separator and whatman glass fiber separator were used to fabricate all coin cells. The electrolytes used for all coin cells were 1 M $NaPF_6$ (Alfa Aesar, >99%) in diglyme (Sigma-Aldrich, 99.5%) for Na chemistries and 1 M KPF_6 (Sigma-Aldrich, 99.5%) in diglyme (Sigma-Aldrich, 99.5%) for K chemistries. Electrochemical testing was performed on a multichannel Metrohm Autolab testing apparatus and MTI 8 Channel Battery tester.

5.3 Results and Discussion

To develop a fast charging battery that relies upon co-intercalation at the anode, and an open framework cathode architecture, we first characterized each type of electrode material in a half-cell configuration (Figure 6.1). Both Na^+ and K^+ charge storage in natural graphite *via* co-intercalation was explored using diglyme (DEGDME) solvent using half-cells: Na|$NaPF_6$ in DEGDME|GR and K|KPF_6 in DEGDME|GR. As the coordinated alkali ions and solvent molecule co-intercalate into the graphite, the spacing between the graphene sheets in the c-direction increases and reversibly restores its original structure upon extraction[177] (Figure 5.1a). Galvanostatic cycling can be observed in Fig. 6.1b as the half-cells are charged and discharged and the alkali ions are inserted and extracted into the graphite, respectively. The rate capability of natural graphite as a co-intercalation anode was galvanostatically tested and the results can be

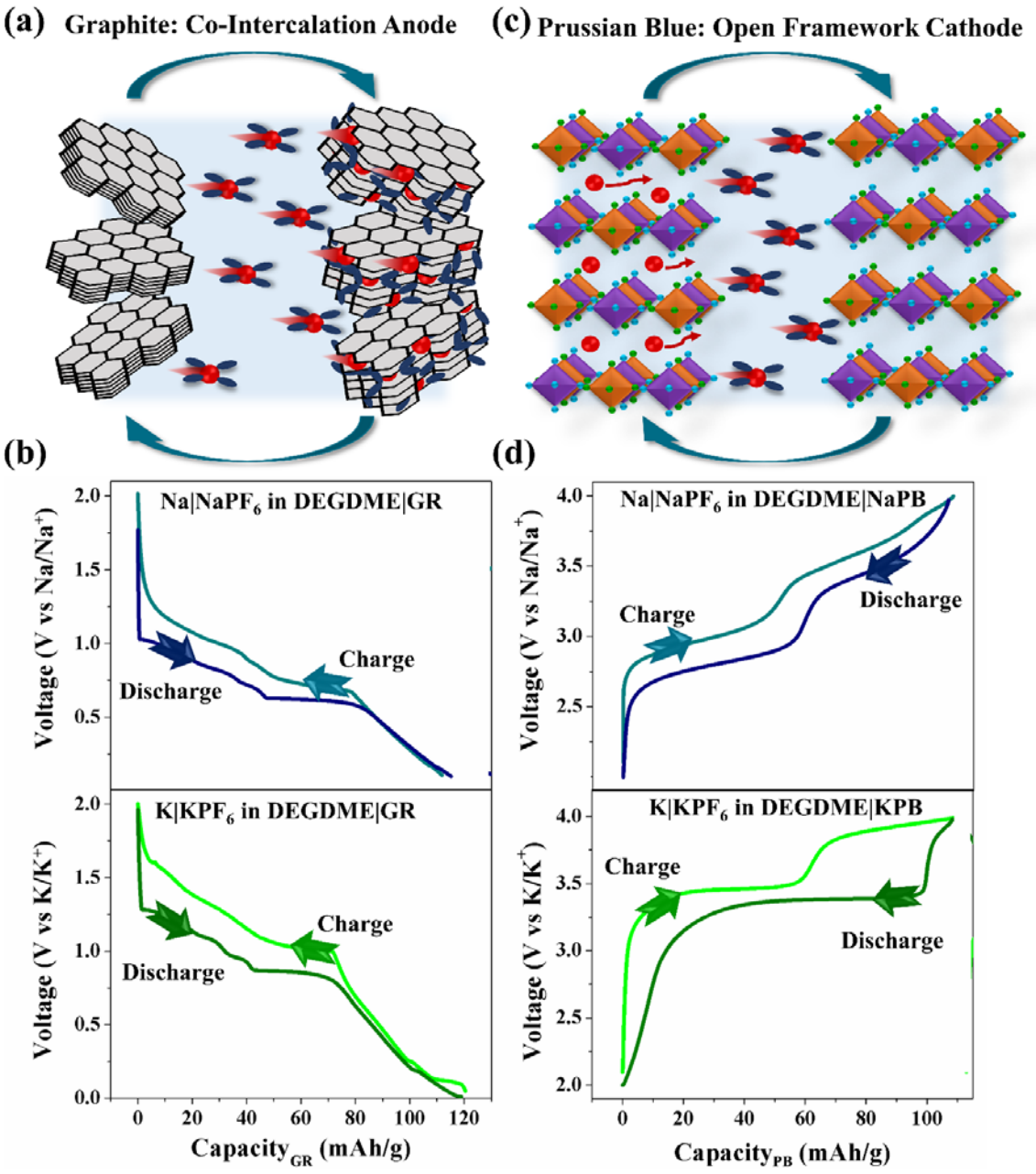

Figure 5.1 Diglyme electrolyte solvent is compatible with both anode and cathode chemistries, confirmed by galvanostatic charge-discharge curves of both Na and K chemistries of (b) natural graphite and (d) Prussian blue.

found in Figure 5.13. Similarly, half-cells of alkali metal Na or K and the respective PB electrode, $Na|NaPF_6$ in DEGDME|NaPB (NaPB) and $K|KPF_6$ in DEGDME|KPB (KPB), were made to study

the synthesized Prussian blue in the diglyme system. Figure 5.1c and galvanostatic charge-discharge curves for both the NaPB and KPB electrode materials illustrate the alkali ions moving out of the PB structure on charge and back into the PB open framework on discharge for both Na and K chemistries (Figure 5.1c, d). The rigid structure and large interstitial sites[186] of this perovskite-type structure[184] metal organic framework facilitate the intercalation process, allowing for high rate capability, as further demonstrated in this study.

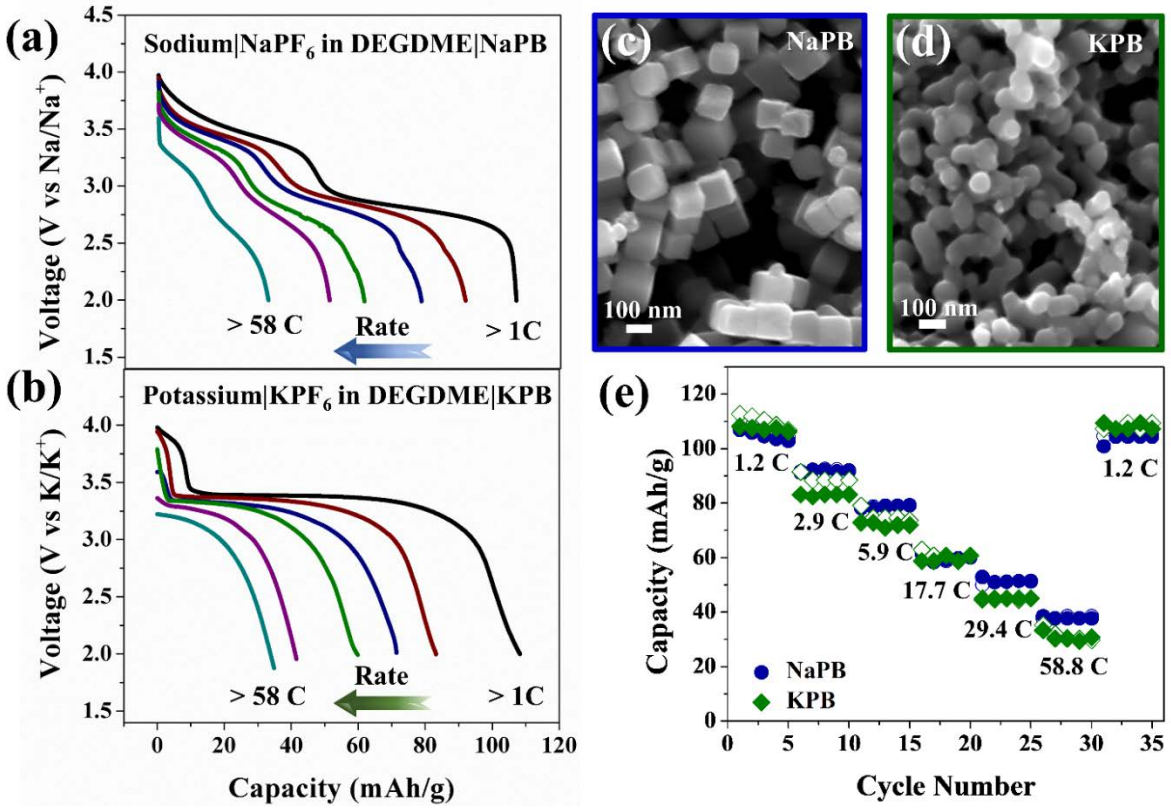

Figure 5.2 Prussian blue cathode supports both Na and K chemistries for high rate capability demonstrated by the synthesized (c) NaPB and (d) KPB nanoparticles and their corresponding electrochemical performance (a, b, e).

Further, scanning electron microscopy (SEM) of the as-synthesized PB particles are shown in Figure 5.2c and 5.2d. KPB particles are more spherical in morphology (Figure 5.2d) compared with the NaPB (Figure 5.2c) which are more cubic, corresponding to past literature

observations.[184, 186, 189, 190] Both NaPB and KPB particles are ~100 nm in diameter with the particle size of NaPB is ~100nm in diameter while that of KPB is < 100nm, yielding capacities consistent with those from previous work.[199] In this work, we use XRD ad EDS along with analysis of the electrochemical performance to qualify the composition of the Prussian Blue analogues. XRD analysis (Figure 5.7) shows that the NaPB is rhombohedral in structure while KPB has a monoclinic crystal structure. Both atomic arrangements are a result of the higher Na and K content, respectively, as the higher alkali ion concentrations force the lattices to shift into lower symmetry structures. This shift is consistent with that observed for NaPBs[184-186] and KPBs[199] intentionally synthesized with high sodium and potassium content for battery cathodes. EDS spectra and mapping (Figure 5.8-5.10) supports electrochemical observations to suggest that the composition of the Prussian Blue analogues are Na_xPB, $x > 1.9$ and K_xPB, $x < 1.7$.

A rate study was conducted for both NaPB and KPB half cells to probe the rate-capability of the individual working electrodes (Figure 5.2 a, b, e). Both NaPB and KPB were tested at C rates spanning between 1 C to ~ 60 C, which yields charging times of ~1 minute (Figure 5.2e). At rates near 1 C, both NaPB and KPB exhibit storage capacity of ~110 mAh/g, while at the highest rate (58.8 C) the NaPB maintains a capacity of ~38 mAh/g and the KPB exhibits ~31 mAh/g.

As half-cell performance confirms material stability of both the NaPB and KPB and reflects the stability of the electrode material over a certain set of testing conditions, full-cell batteries require a combination of electrode/electrolyte compatibility, high Coulombic efficiency, and minimal first cycle loss such that the alkali metal shuttling between the electrodes actively participate in the intercalation reactions. In this spirit, we tested Na and K full-cells, GR|$NaPF_6$ in DEGDME|NaPB and GR|KPF_6 in DEGDME|KPB. A rate study with the full-cells was conducted to examine the electrochemical performance at high rates and corresponding capacities.

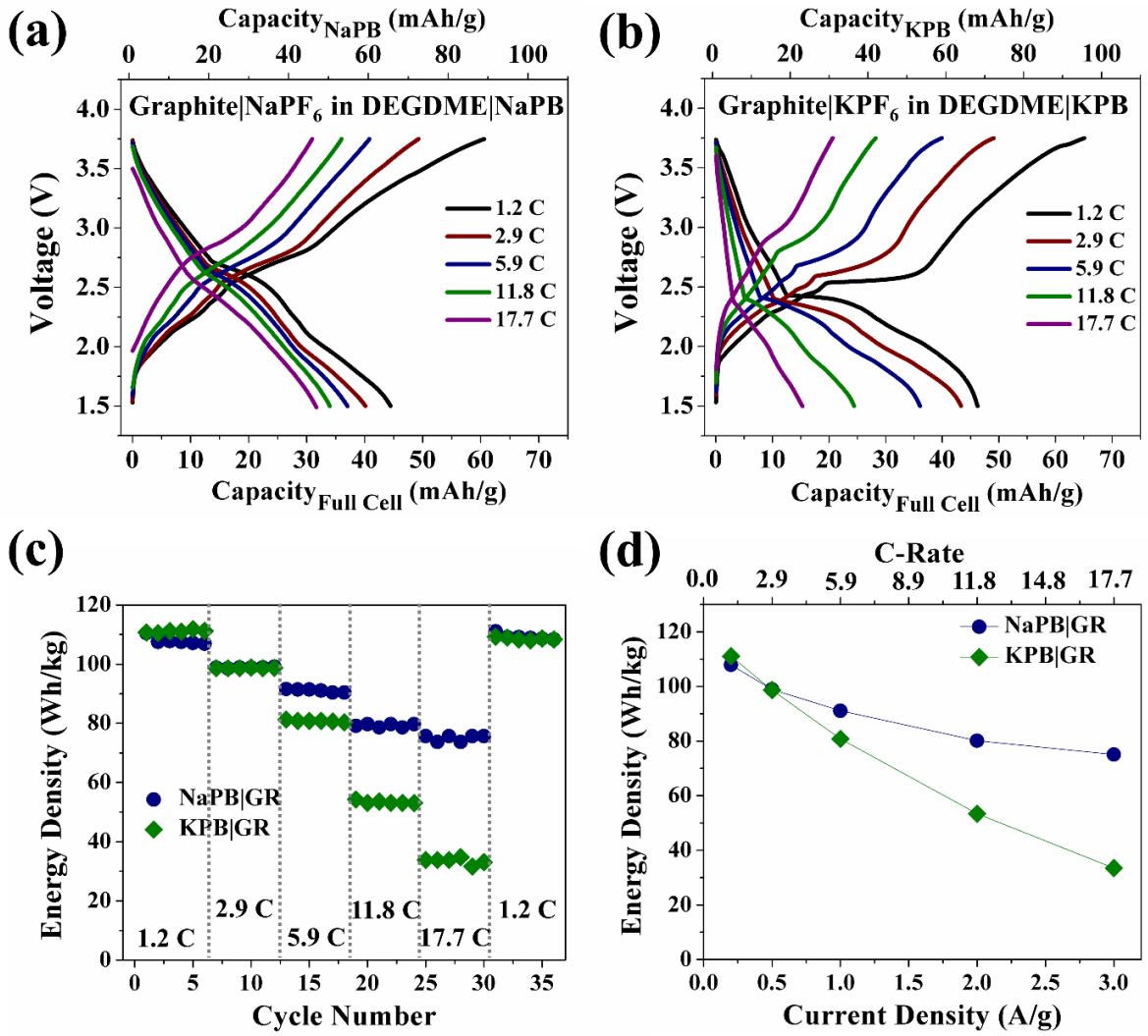

Figure 5.3 Electrochemical performance of rate study of GR|PB full cell, galvanostatic charge-discharge curves of 1st cycle of each rate for (a) Na and (b) K chemistries, (c) corresponding plot of energy density at cycle, and (d) average energy density at each rate.

Galvanostatic charge-discharge curves (Figure 5.3 a, b) represent the measured cell capacity with respect to the cathode (NaPB) and both electrodes (FullCell). The latter case represents the actual full-cell capacity of the device, even though the former is commonly reported in the literature. As has been reported with the Prussian blue system[185, 190, 191] even with other commercially viable battery systems such as the lithium nickel manganese oxide and graphite cells,[200] the compatibility between half-cells and full-cells differ. This is most likely due to the

increased number of active material interfaces in a full-cell, such as those between the active materials and current collectors and active materials with each other. In a half-cell there is a surplus of alkali ions, in this work either Na or K, however when introducing another active material interface, different types of SEI layers form with diverse SEI layers which can impede kinetics and diffusion in the full-cell.[201]

All batteries were cycled between rates of 1.2 C to 17.7 C, with the applied current calculated with respect to the cathode material. The energy density (*E*) was assessed based on the relation:

$$E = \mathrm{I}/M \int_0^{\mathrm{t}} V(t)dt$$

where M is the total combined electrode mass, V(t) is the voltage during galvanostatic testing, and I is the (constant) current used for the galvanostatic measurement. The energy density is shown in Figure 5.3c at different charging/discharging rates. From this data, we observe the energy density of the Na and K batteries to be ~ 110 Wh/kg at rates of 1.2 C to energy density of ~ 75 Wh/kg for NaPB|GR and ~30 Wh/kg for KPB|GR at the fastest charging rate of 17.7 C. Cycling coulombic efficiencies and first cycle decay can be found in Figure 5.15 and 5.16, respectively. Although there are many factors that contribute to the rate capability of the system,[202, 203] we attribute the lower reversible capacity, and consequently lower energy density, of the KPB|GR battery at high rates to larger charge transfer resistance (Figure 5.18). Especially at high rates, there can be additional electrolyte consumption as a result of joule heating due to oxygen reactions that occur at the end of fully charging the device.[204] While understanding the mechanisms that influence the coulombic efficiencies is very important and a good platform for future work, this study demonstrates promise of this open framework/co-intercalation architecture design for full cell batteries.

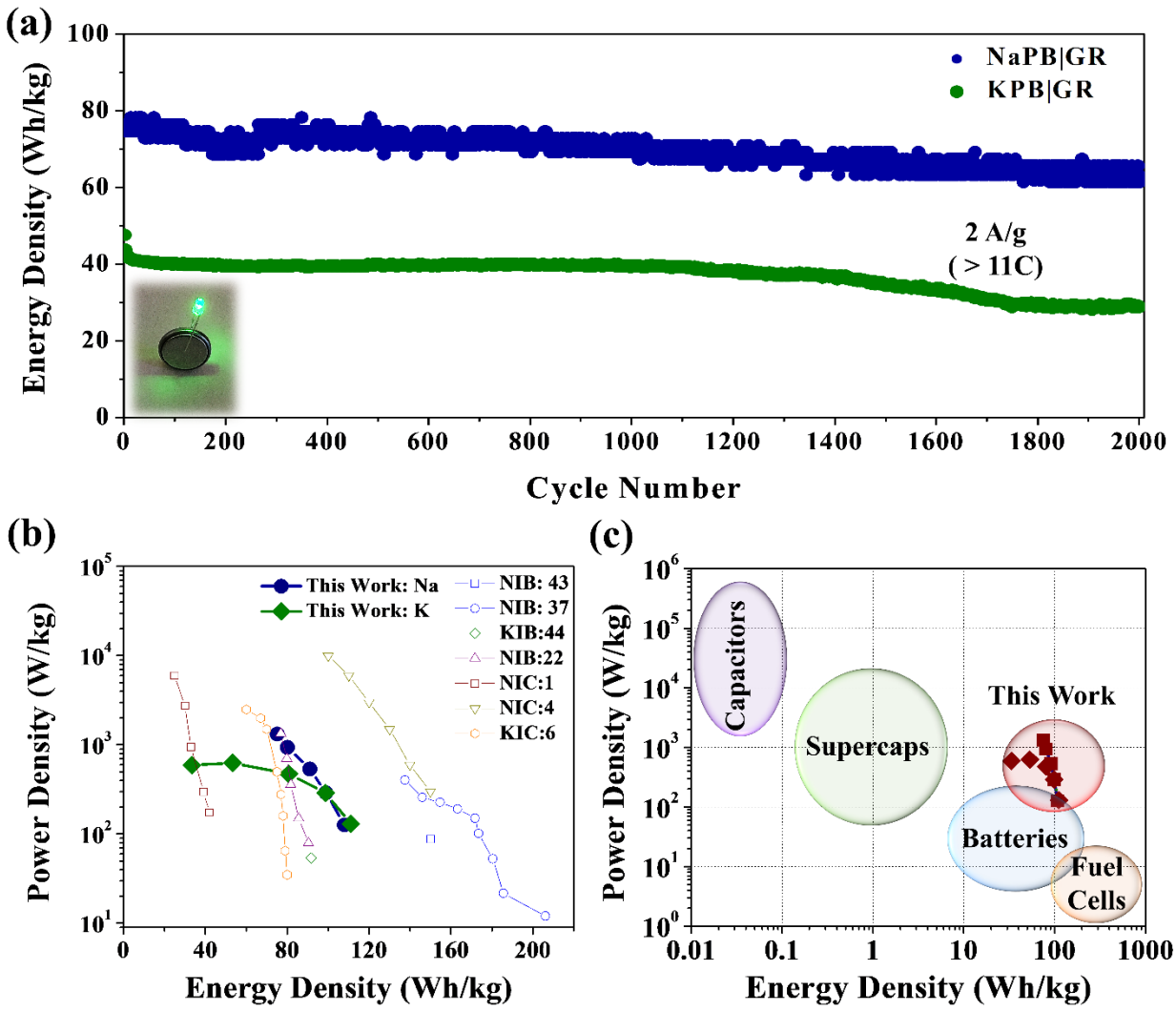

Figure 5.4 Full cell high rate capability for extended cycling at (a) 2 A/g for 2000 cycles with an inset of a lit green light LED, (b) this work compared to literature, and (c) this work compared with other electrochemical energy storage devices.

To characterize the durability of these fast-charging batteries, each of these devices were subjected to extended high rates of 2 A/g, or ~ 11 C (Figure 5.4a). The NaPB|GR full-cell maintained a capacity retention approaching ~ 80% over 2000 cycles and the KPB|GR full-cell retained nearly 60% capacity. This emphasizes cycling performance, especially for the NaPB|GR, promising for technological applications where augmented power capability can be achieved with comparable cycling duration to existing battery systems. It should also be noted

that safety is often highlighted as a challenge in high power operation of Li batteries, with one reason for this being the non-uniform deposition of Li that occurs under high currents. In such systems, dendrite formation originates from the anode as the local host insertion lattice achieves full capacity and Li metal plating occurs on the anode surface. Whereas this is problematic for Li cells since Li metal plating in liquid electrolytes is unstable, leading to dendrite formation, the less negative electrochemical potential of Na/Na+ compared to Li/Li+ leads to dendrite-free and stable plating processes that occur within the electrochemical window of glyme electrolytes.[182, 205] This implies that, at least for fast-charging Na batteries, such non-uniform deposition will not lead to adverse safety concerns that remain problematic for fast charging Li batteries, even though this could be a concern for the fast charging K batteries since K metal plating is similarly unstable.[206, 207]

To understand how our results compare to other high power approaches discussed in the literature, we have plotted our results compared to others who have reported full-cell battery performance (Figure 5.4b). Recent reports by Jiang et al. (blue squares, Figure 5.4b) and Wang et al. (blue circles, Figure 5.4b) have demonstrated Prussian blue and Prussian white cells with energy densities of 150 Wh/kg and 206 Wh/kg, respectively. However, in both cases the cell performance remains limited to rates less than 0.5 A/g. Alternatively, Le Comte et al. (Orange hexagons, Figure 5.4b) reported long term cycling for over 60,000 cycles at 5 C but with lower energy densities of ~11 Wh/kg and power densities on par with those reported in this work. Other works reporting NIC and KIC performance sandwich the power and energy density values in this study. When comparing the devices from this study with other electrochemical energy storage devices (Figure 5.4c), it is evident that the energy density is on par with and the power density is higher than that of battery technologies. Even when considering the mass contributions

from packaging, the power and energy densities are still improved over current battery technologies. In our study, we demonstrate the feasibility for a battery system to enable both high rate performance and moderate energy densities with the possibility to further tune and optimize both the open framework cathode structure, as well as the electrode-electrolyte interface that enables co-intercalation to engineer the performance characteristics in the framework of this general fast-charging battery design scheme.

5.4 Conclusion

In summary, here we have demonstrated how a co-intercalation natural graphite anode and an open framework Prussian blue cathode can enable high-power batteries with moderate energy density >100 Wh/kg and power density > 1000 W/kg. Using a co-intercalation anode, 1) eliminates the rate-limiting step of alkali ion de-solvation at the electrode-electrolyte interface, allowing for high rate capability and 2) allows for alternative ion intercalation into graphitic carbon. Prussian blue as a cathode material offers a rigid, open framework with large interstitial sites for ease of rapid ion extraction and insertion, supporting both Na and K chemistries.

The synergy of these electrode materials holds great promise for high-power batteries for electric vehicles and efficient storage of renewable energy. Further investigation into refining the cathode material allows for tunability to access a broad range of power and energy densities currently outside the scope of traditional supercapacitor and battery systems. This study lays the groundwork for engineering an electrode/electrolyte system for fast-charging, energy-dense batteries that overcome the limitations of supercapacitors and enable performance as a battery at high currents or under fast-charging conditions.

Acknowledgments

The authors acknowledge Mengya Li, Keith Share, and Kody Wolfe for helpful discussions, and the laboratory facilities of Rizia Bardhan. This work was supported in part by NSF grant CMMI 1400424, and A.P.C. was supported by NSF graduate fellowships under grant 1445197.

5.5 Appendix

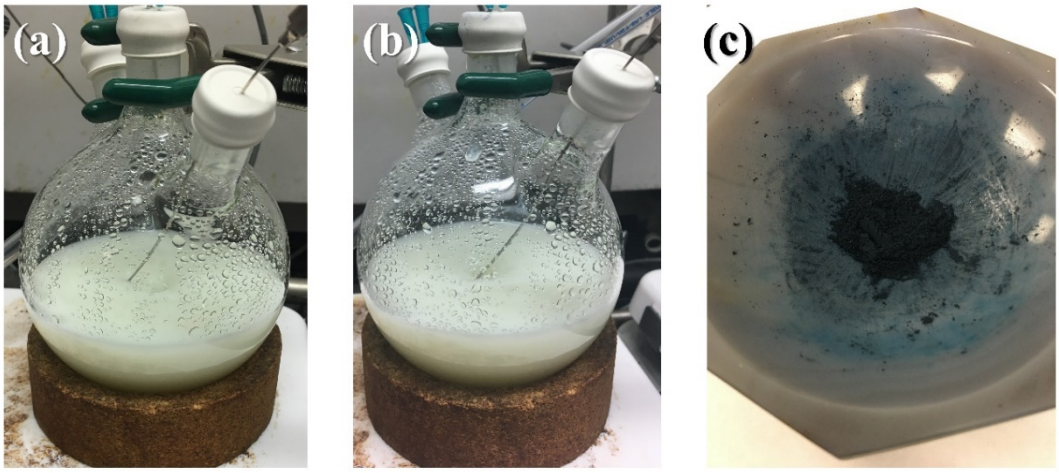

Figure 5.5 Experimental images of NaPB synthesis after all precursors were added at (a) t = 0 hours, (b) t = 4 hours, (c) and the resulting product.

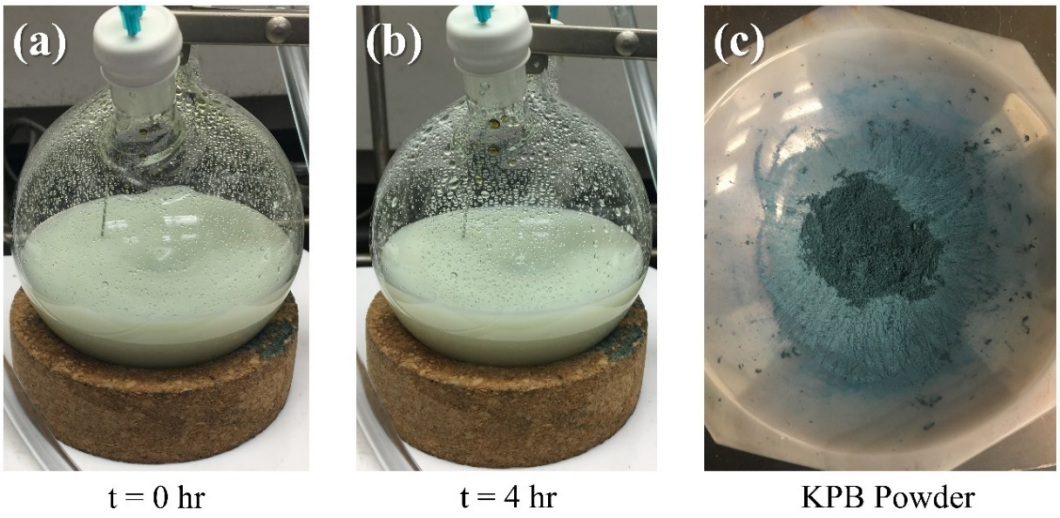

Figure 5.6 Experimental images of KPB synthesis after all precursors were added at (a) t = 0 hours, (b) t = 4 hours, (c) and the resulting product.

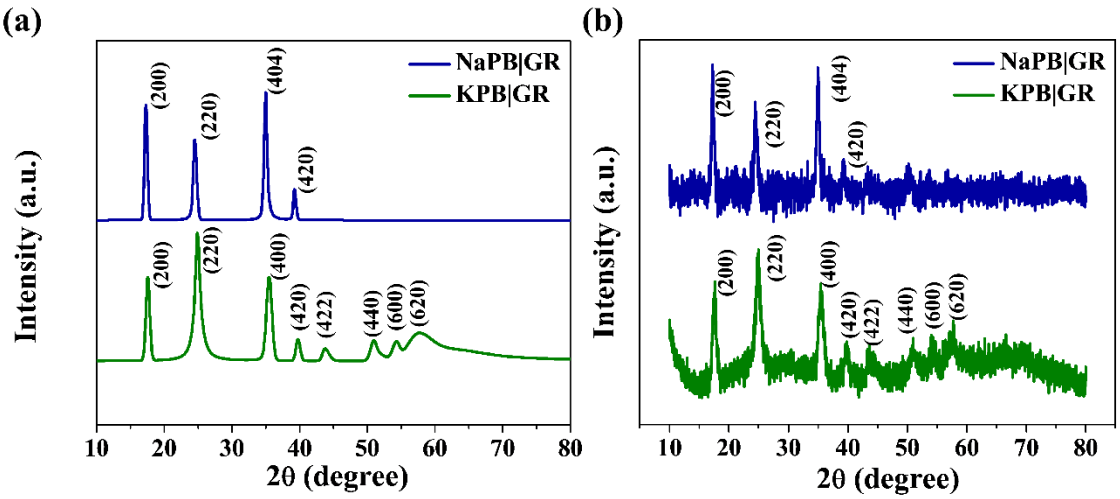

Figure 5.7 XRD of synthesized NaPB and KPB: (a) smoothed and (b) unsmoothed data.

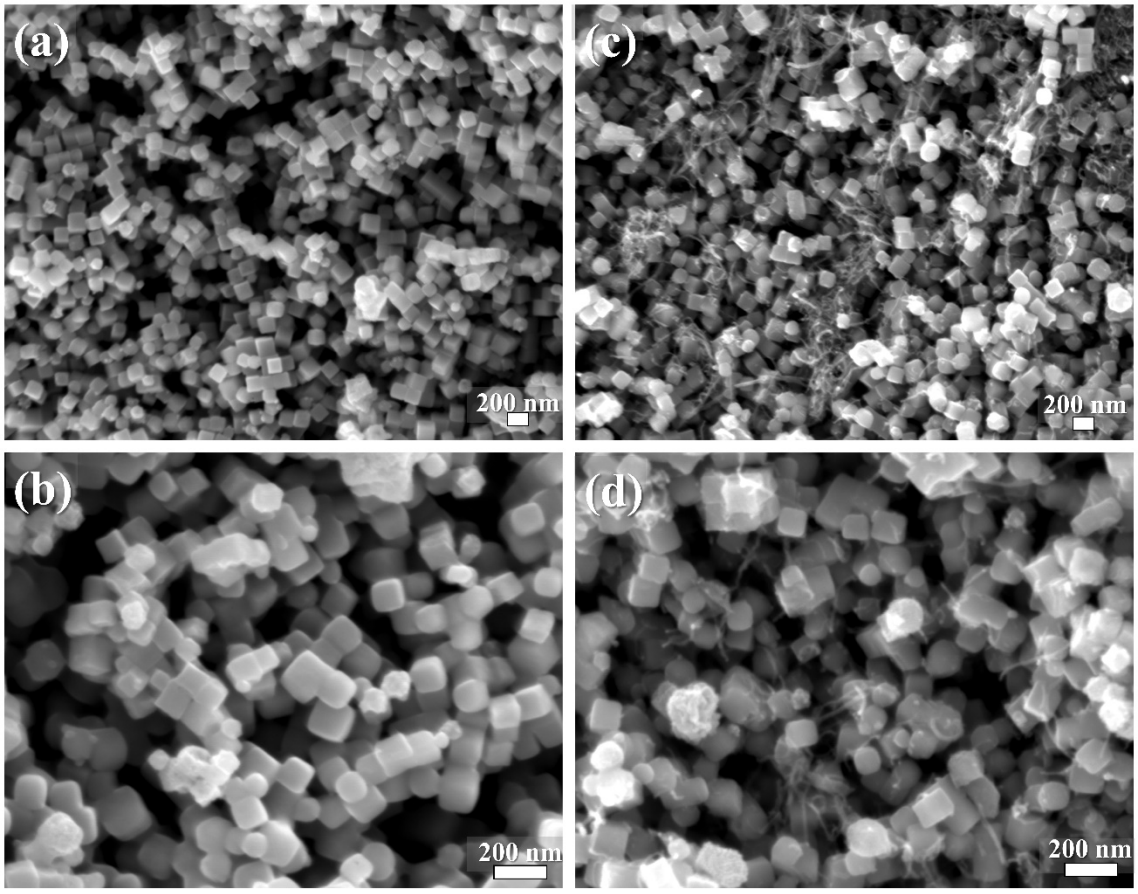

Figure 5.8 Scanning electron microscopy images of (a), (b) synthesized NaPB and (c), (d) synthesized NaPB with multiwall carbon nanotubes.

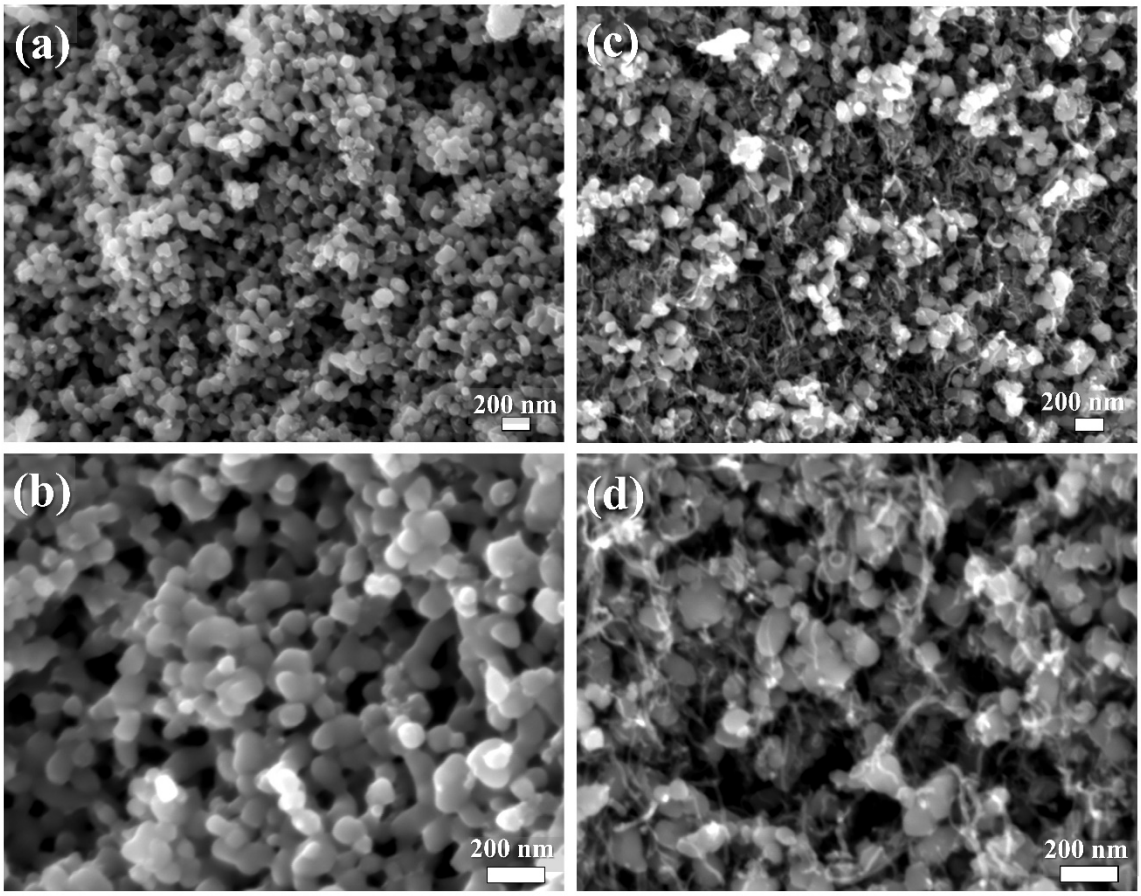

Figure 5.9 Scanning electron microscopy images of (a), (b) synthesized KPB and (c), (d) synthesized KPB with multiwall carbon nanotubes.

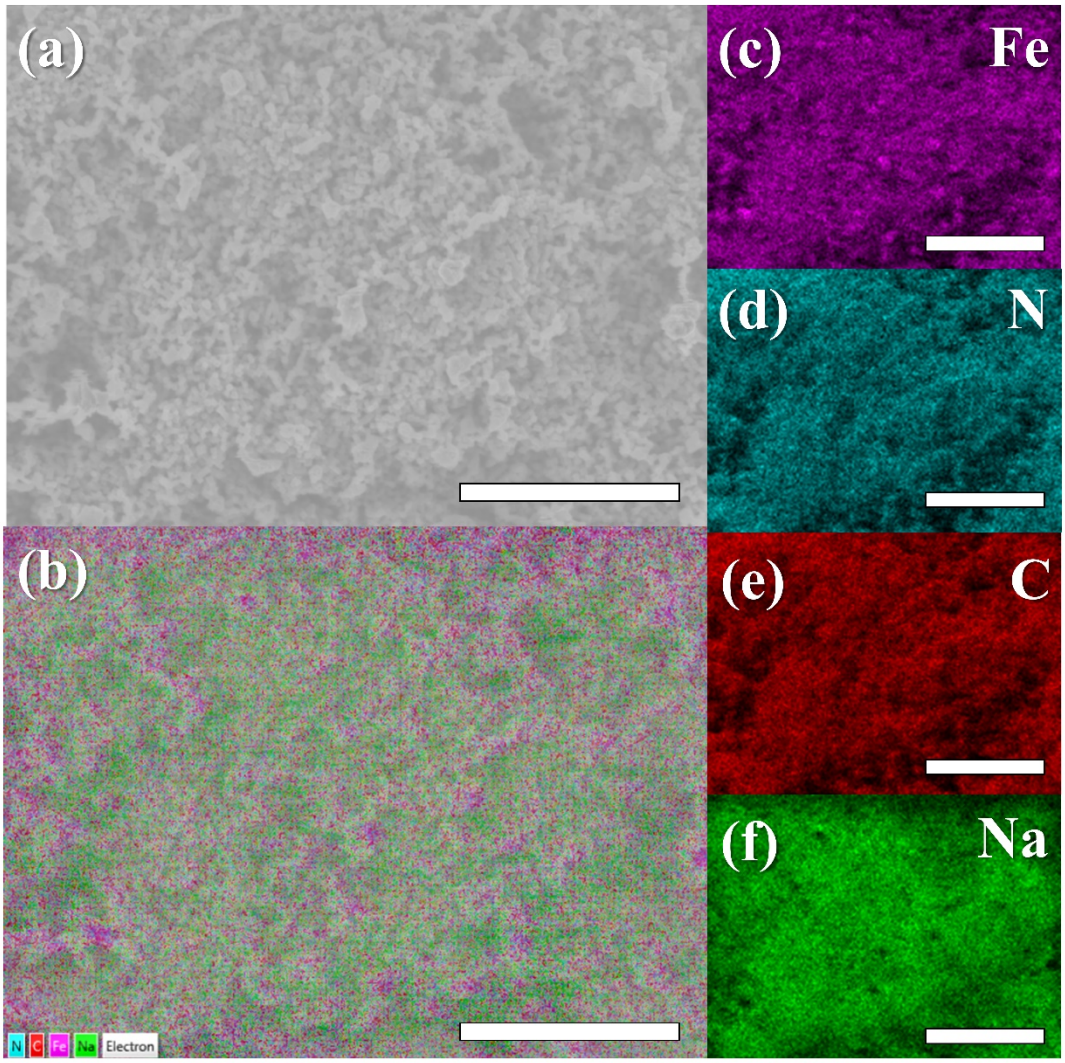

Figure 5.10 Elemental analysis of synthesized NaPB all with scale bar of 5 µm (a) electron image, (b) all elements, (c) iron, (d) nitrogen, (e) carbon, (f) sodium.

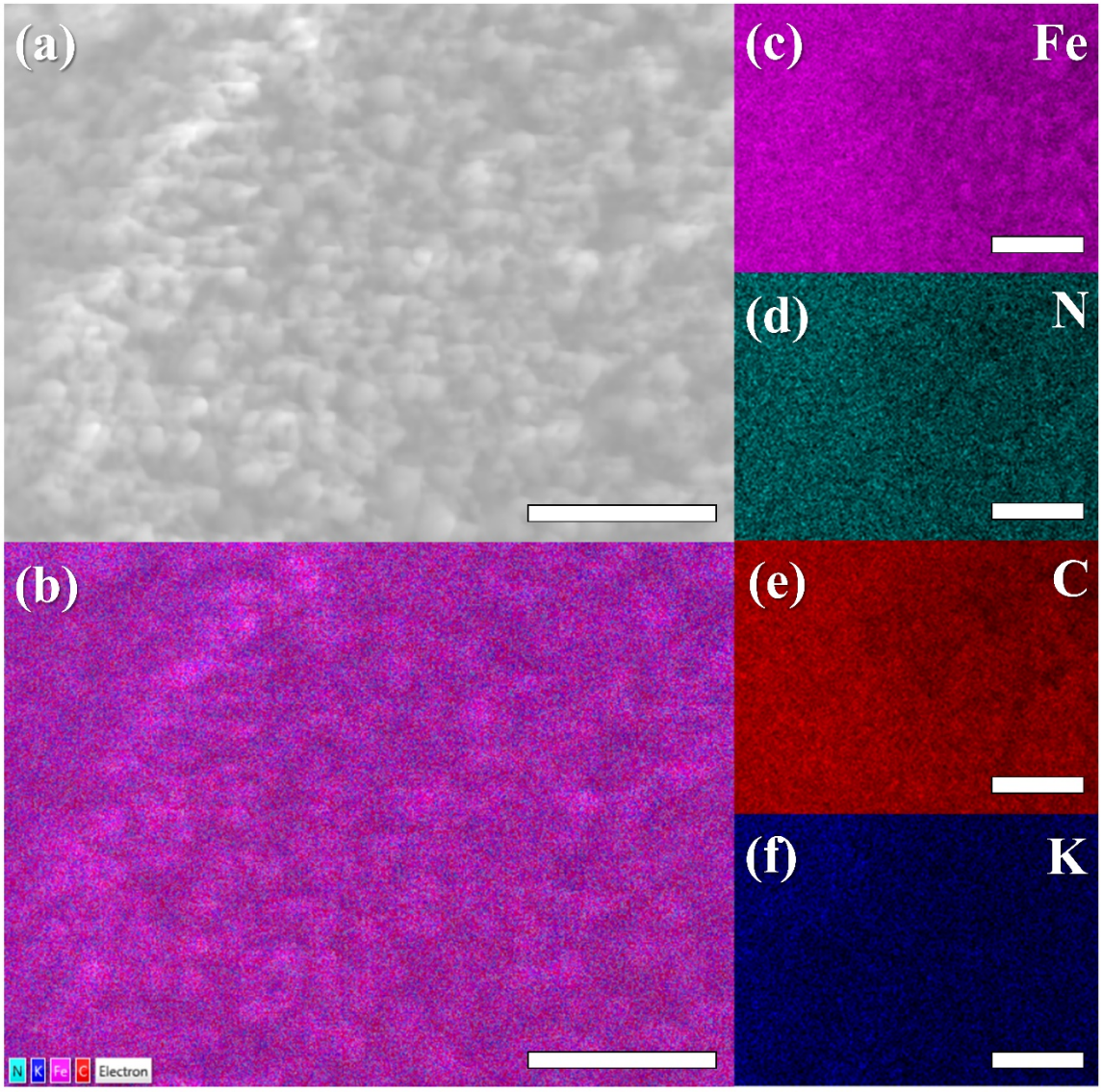

Figure 5.11 Elemental analysis of synthesized KPB all with scale bat of 1 µm (a) electron image, (b) all elements, (c) iron, (d) nitrogen, (e) carbon, (f) potassium.

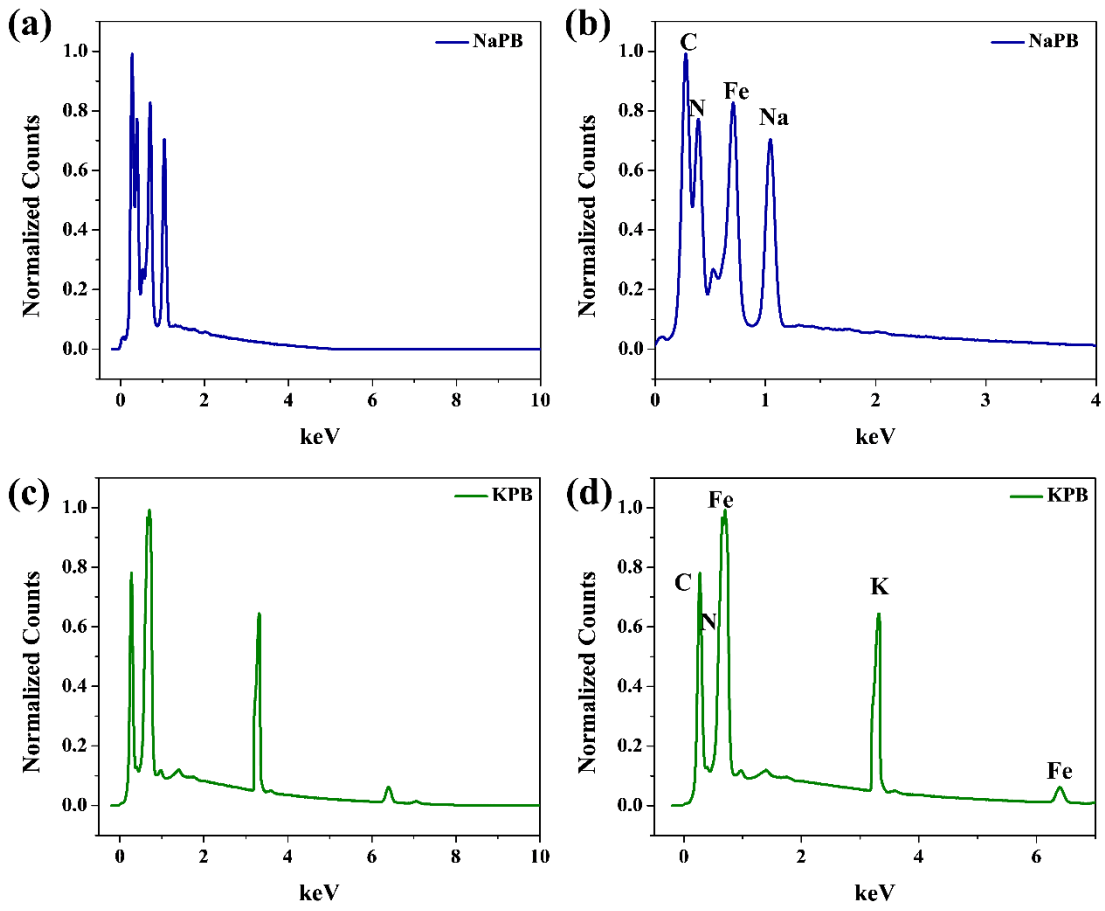

Figure 5.12 Energy dispersive x-ray spectroscopy for elemental analysis of the Prussian blue analogues (a), (b) NaPB and (c), (d) KPB.

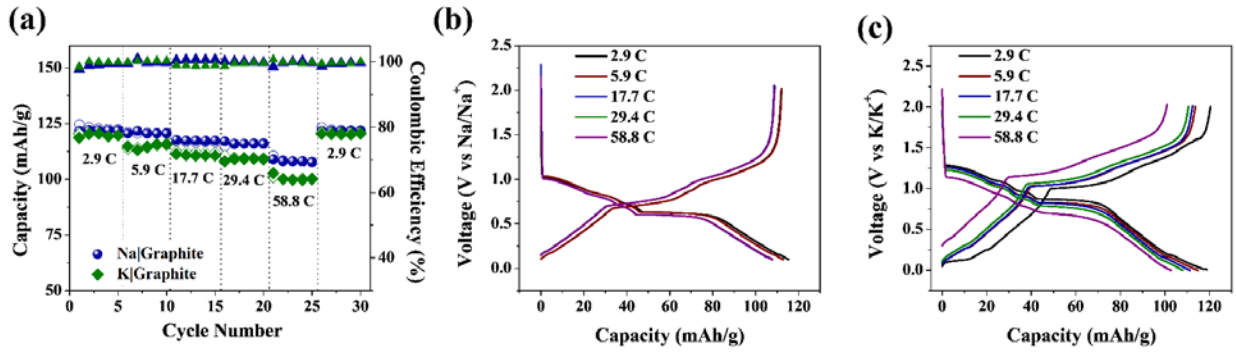

Figure 5.13 Electrochemical data from Na|GR and K|GR half cells (a) rate study, and galvanostatic charge discharge curves of the first cycle at each rate of the rate study for (b) Na|GR, and (c) K|GR.

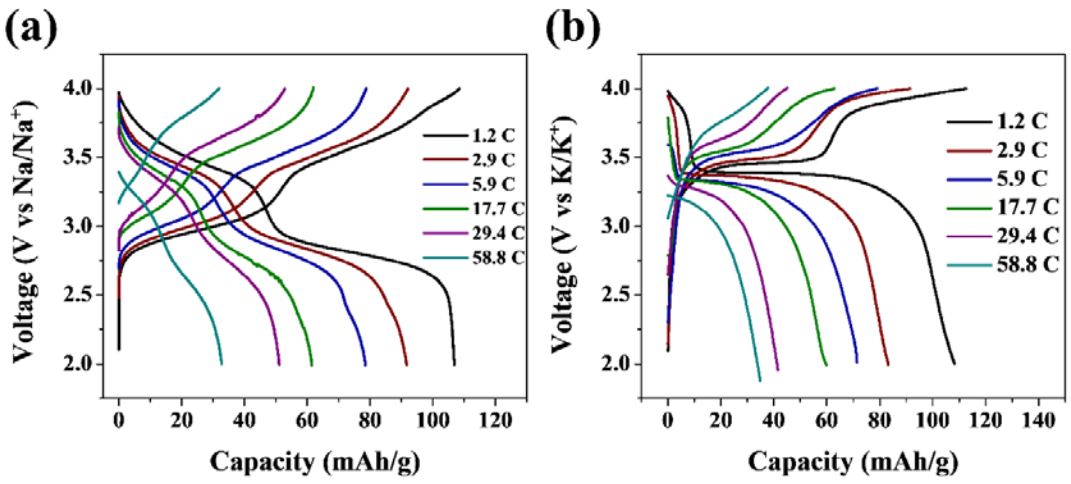

Figure 5.14 Electrochemical data from Na|PB and K|PB half cells, galvanostatic charge discharge curves of the first cycle at each rate of the rate study for (a) Na|PB, and (b) K|PB.

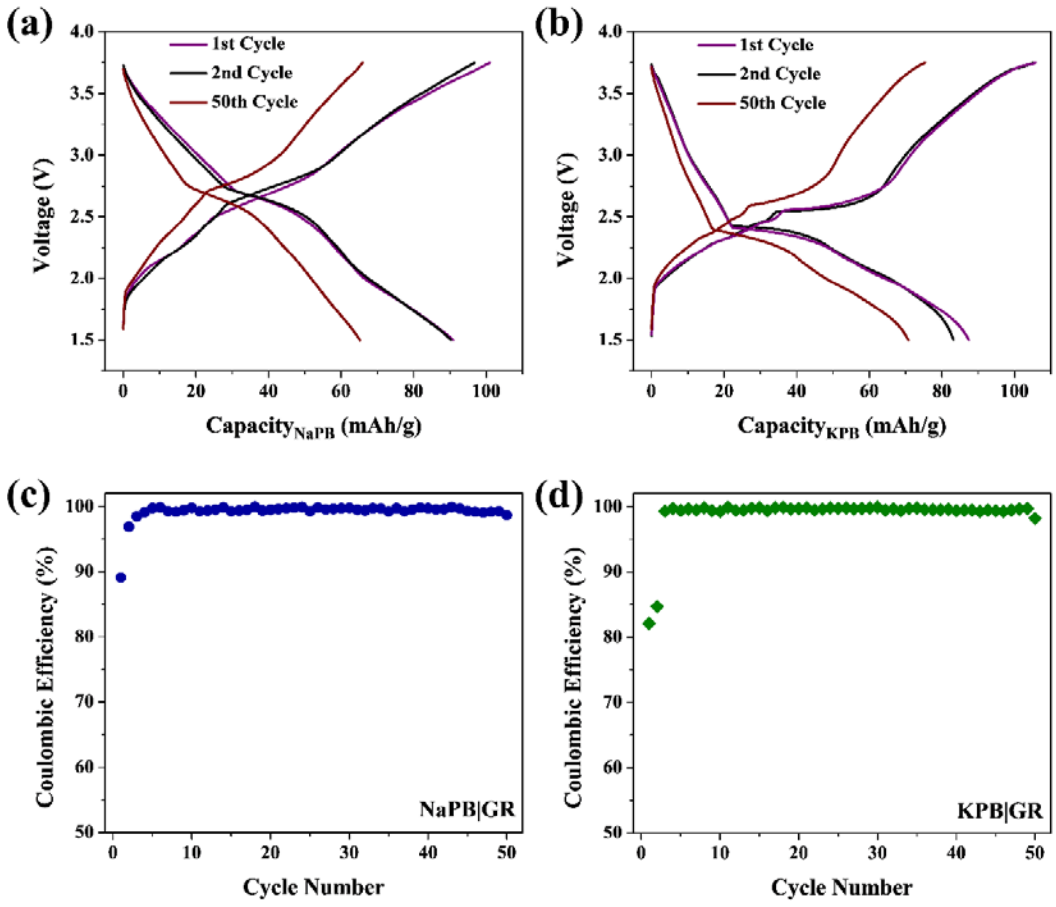

Figure 5.15 Electrochemical data from NaPB|GR and KPB|GR full cells, galvanostatic charge discharge curves of the first, second, and last (50^{th}) cycles at 1.2 C for (a) NaPB|GR, and (b) KPB|GR, and corresponding coulombic efficiencies for (c) NaPB|GR, and (d) KPB|GR.

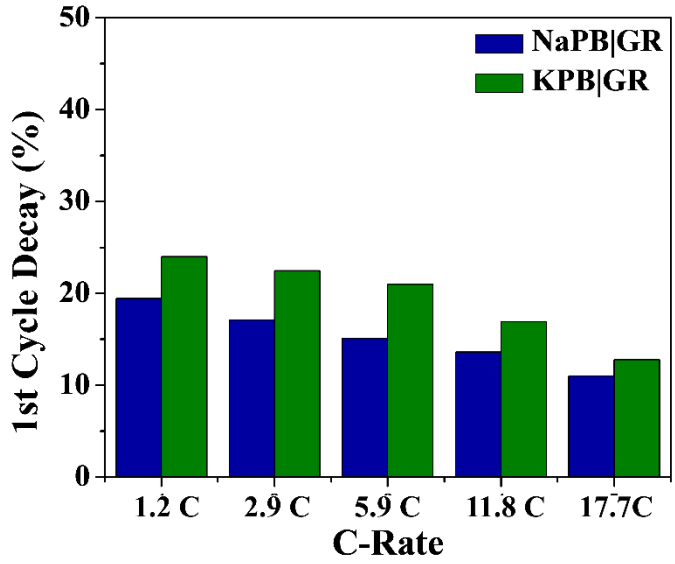

Figure 5.16 1st cycle decay for both NaPB|GR and KPB|GR full-cells.

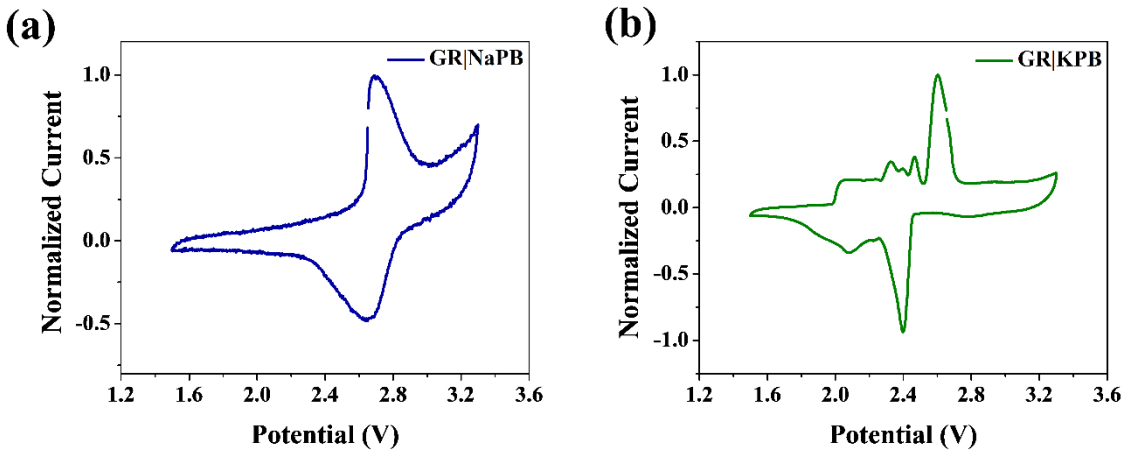

Figure 5.17 Cyclic voltammetry of (a) GR|NaPB and (b) GR|KPB full-cells.

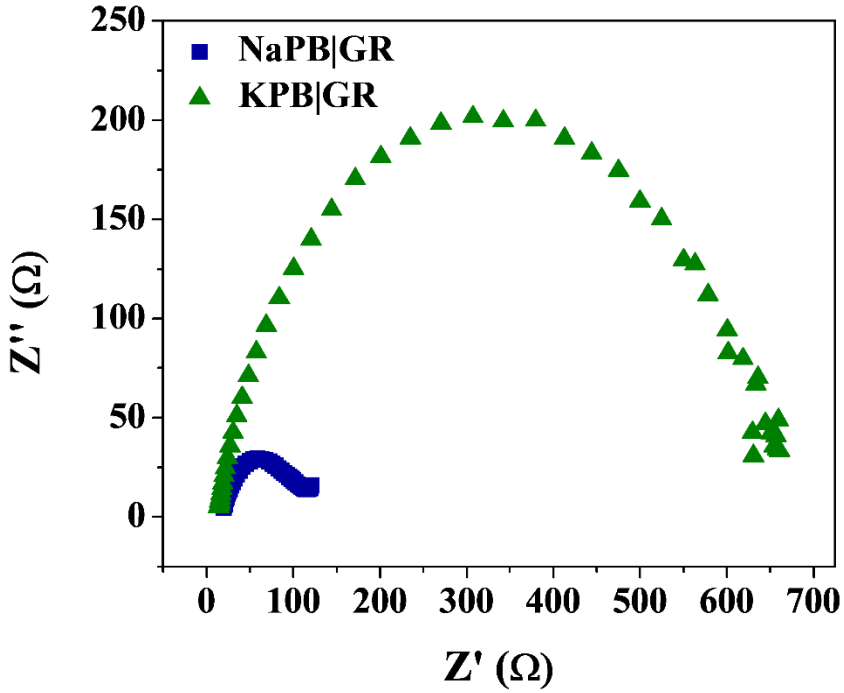

Figure 5.18 EIS data of full cells NaPB|GR and KPB|GR.

Chapter 6

Carbon Fiber Reinforced Structural Lithium-Ion Battery Composite: Multifunctional Power Integration for CubeSats

Adapted from: K. Moyer, C. Meng, B. Marshall, O. Assal, J. Eaves, D. Perez, R. Karkkainen, L. Roberson, C.L.Pint, "Carbon Fiber Reinforced Structural Lithium-Ion Battery Composite: Multifunctional Power Integration for CubeSats," Energy Storage Materials, (2019) doi.org/10.1016/j.ensm.2019.08.003.

6.1 Introduction

The developmental trend for electricity use over the past several decades has shifted from systems dependent upon a centralized source of electricity to systems fully supported by portable batteries. In this regard, the boom in portable technology has been primarily enabled by the commercial development of lithium-ion (Li-ion) battery electricity storage media. Simply extrapolating this development forward, batteries and energy systems will likely evolve from externally situated systems to integrated flexible, structural, wearable, and multifunctional materials.[208, 209] Similarly, such a transition in the form factor of the energy storage platform can enable a new leg of technology development focused on power-integrated systems and materials. Despite this vision, there are critical fundamental challenges posed in efforts to increase the functionality of battery systems.[210-212] Most notably, Li-ion batteries require operation in the absence of air exposure due to electrolyte and/or electrode sensitivity to air.[213] Additionally, Li-ion batteries are packaged under compression to mitigate mechanical failure mechanisms.[214, 215]

In turn, any efforts to un-package a Li-ion battery into a multifunctional platform must clearly address these challenges.

In this regard, numerous reports have emerged in the past few years focused on the conception and design of structural energy storage systems. This includes efforts both in supercapacitors[216-221] and batteries[222-227] where the energy storage material is situated into a solid-state composite matrix without compromising the mechanical properties of the matrix material. Current approaches are generally divided into two separate thrusts: (1) the integration of commercially packaged energy storage systems into composite structures,[228-230] and (2) the design of multifunctional materials that can be processed much like traditional composite materials, but exhibit both structural and energy storage properties.[227, 231-234] In the former case, Periera *et al.* embedded pre-manufactured Li-ion cells into a carbon fiber matrix, but discontinuity at the matrix-battery interface in this approach detracts from the intrinsic mechanical advantages of carbon fiber composites.[229] In the latter case, researchers have taken steps to evolve packaged lithium battery materials into structural templates. Early work by P. Liu *et al.* replaced particulate fillers in electrodes with carbon fibers, but this structure lacked external reinforcement and required additional packaging for mechanical performance.[235] Other approaches in this direction have demonstrated battery performance in solid materials, but routes to sustain multifunctional performance and packaging remain challenging. Most recently, efforts by G. Fredi[236] et al. and E. Jacques et al.[237, 238] showed that carbon fiber materials can be used for lithium battery anodes, and emphasize this as a step toward a structural battery. However, despite a persistent vision toward a Li-ion battery fabricated along with and into a structural composite, no reports yet have shown a successful path to achieve this, despite progress on modular structural elements including electrolytes and electrodes that could be useful for such a battery system. Further, whereas

multifunctional energy materials have broadly garnered some attention, current advances in this area do not clearly delineate the system-level advantage for integrated energy storage systems.

In this letter, we demonstrate the direct integration of a pouch-free full cell Li-ion battery materials into a carbon fiber containing composite matrix to produce a high-performance structural battery. This strategy provides a clear system-level performance advantage for integration since the inactive materials for the Li-ion battery are the active materials for the carbon fiber epoxy composite matrix. We utilize carbon fiber as the current collector with graphite/carbon fiber anodes and LFP/carbon fiber cathodes, which are directly integrated into the carbon fiber panels via a traditional composite layup process. We demonstrate total energy density above 35 Wh/kg relative to all active and composite packaging materials and specifically show how this pouch-free battery composite material can be used to fabricate the walls of a 1U CubeSat to absorb the electrical energy storage capability into the CubeSat structural walls and increase the utility of interior CubeSat volume.

6.2 Experimental Details

6.2.1 Electrode Fabrication

All electrodes were slurry cast onto 6 cm x 6 cm de-sized carbon fiber current collectors (NASA, Prototype Lab). To make the graphite electrodes, the slurry consisted of graphite powder < 20 μm (Sigma-Aldrich), conductive carbon black (MTI), and PVDF binder (MTI, >99.5%) in the respective ratio of (80:10:10). To make the $LiFePO_4$ electrodes, the slurry consisted of $LiFePO_4$ powder (MTI), conductive carbon black (MTI), multiwall carbon nanotubes (CheapTubes, >95%) and PVDF binder (MTI, >99.5%) in the respective ratio of (65:20:5:10). A Zeiss Merlin scanning electron microscope was used to examine the materials used for fabricating the battery electrodes.

6.2.2 Carbon Fiber Composite Battery Assembly & Electrochemical Testing

To begin the layup process to make one composite battery panel, 4 pieces of 8.4 cm x 8.4 cm PAN based carbon fiber (NASA, Prototype Lab) were cut. Using a roller and squeegee, all 4 carbon fiber squares were impregnated with epoxy (Fibre Glast Developments Corp., System 1000 Laminating Epoxy Resin Standard Part Kit 1000/1025). The carbon fiber battery was assembled with the following architecture; two epoxy-impregnated carbon fiber pieces|graphite electrode along with a copper foil tab|whatman glass fiber separator|$LiFePO_4$ electrode with an aluminum foil tab|two epoxy-impregnated carbon fiber pieces. To attach the tabs to the graphite and $LiFePO_4$ electrodes, copper and aluminum pieces, respectively, were cut in an "L" shape and then attached to the carbon fiber using hot melt adhesive (polymer tape) for heat sealing pouch cell tabs (MTI) Figure S4a). Before placing the separator in the battery system, it was soaked in 1 M LiTFSI (Sigma-Aldrich, 99.95%) in $EMIMBF_4$ (Sigma-Aldrich, >=99%) electrolyte. After soaking the separator in the electrolyte, it was observed that the ionic liquid easily wet the carbon fiber and entire electrode material. This architecture was then allowed to cure under vacuum overnight. To evaluate electrochemical performance cyclic voltammetry and galvanostatic charge/discharge measurements were performed using a Metrohm Autolab 8 channel battery testing system.

6.2.3 Mechano-Electrochemical Testing

An Instron mechanical tester and Autolab PGSTAT101 were used to perfom mechano-electrochemical tests. All samples underwent tensile tests at a strain rate of 2 mm/min.

6.3 Results & Discussion

A key challenge in structural energy storage is the requirement for (1) structural integrity of the energy storing composite, (2) meaningful energy density relative to total composite mass,

and (3) invariant energy storage capability under mechanical loading. Recently, efforts have demonstrated a structural ultrabattery platform, but the energy density relative to all active and packaging materials remains limited to ~ 1 Wh/kg due to the use of heavy laminate materials and a mostly air-stable but lower energy density Ni-Fe battery chemistry.[222] To produce a more practical structural battery composite material, we instead focus on lightweight conductive carbon fibers as a reinforcing material and Li-ion battery chemistries which offer higher achievable energy density. The strength of this approach is that the packaging (or inactive) materials for the Li-ion battery provide a secondary role as the primary materials for the structural carbon fiber composite. This means that unlike the case of an externally situated battery, which requires liquid electrolyte, heavy metal current collectors, and additional packaging materials, the integrated structural battery provides a system-level performance advantage in terms of gravimetric energy storage capability. To assemble these materials into a packaging-free carbon fiber battery composite, we used Li-ion battery materials integrated into a vacuum infusion composite layup process, illustrated in Figure 6.1. In this process, we use carbon fiber as the current collector for both the lithium iron phosphate cathode and graphite anode (Figure 6.1a). Whereas carbon fiber has been previously reported as a potential anode material for Li-ion intercalation, graphitic sheaths on the fibers were used due to the low capacity of the fibers, significant first cycle losses, and non-uniformities that lead to fibers swelling and areas of additional mechanical stresses.[239, 240] Here, we used graphite as the anode material, CF GR (Figure 6.1b) and used a lithium iron phosphate cathode, CF LFP, (Figure 6.1c) incorporated with carbon nanotube (CNT) conductive additives. These active materials were coated onto thermally processed carbon fiber weave materials, which acted as a current collector and structural component in this design. Furthermore, using carbon fiber as the current collectors in a battery can increase the duration of safe zero-volt state of charge.[241]

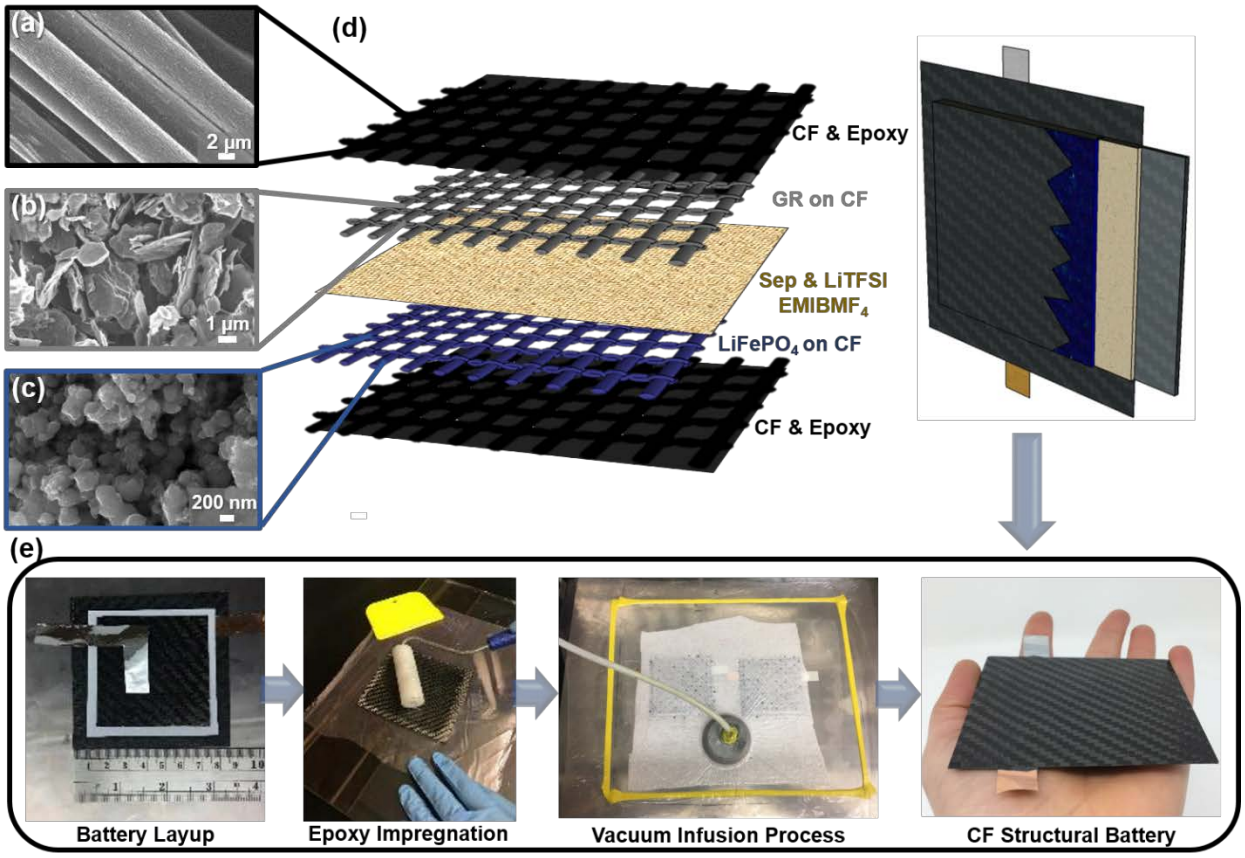

Figure 6.1 Carbon fiber battery composite fabrication as shown by SEMs of a) carbon fiber, b) graphite, and c) lithium iron phosphate, d) a scheme showing the stacking of the individual layers of the composite battery along a picture of these layers cured into a composite material and e) composite layup process along with a picture of a carbon fiber composite structural battery panel being held.

To prepare the electrolyte interface between the electrodes, we overcome air stability issues through the direct assembly of the battery components and electrolyte in the carbon fiber composite layup process. 1 M LiTFSI in $EMIMBF_4$ ionic liquid was infiltrated into the separator between the carbon fiber electrodes and integrated into the Li-ion battery matrix. This electrolyte remains stable within operational voltage window, Figure 6.5, with no observed corrosion at the metal tab connection to the carbon current collector, even though this could be a relevant point to evaluate for studies to evaluate the shelf life/durability of this structural battery.[242] The battery

layup of CF GR|LiTFSI in $EMIMBF_4$|CF LFP was then sandwiched between epoxy-impregnated carbon fiber and then placed under vacuum to cure overnight (Figure 6.1d,e). The electrodes on carbon fiber current collectors were 6 cm x 6 cm in size, resulting in a carbon fiber battery composite with dimensions of 8.4 cm x 8.4 cm.

The entire 8.4 cm x 8.4 cm carbon fiber battery panel was then evaluated electrochemically to characterize energy storage performance (Figure 6.2a, b, c). Galvanostatic charge discharge measurements were performed at a series of rates from 0.10 C to 1.0 C, which yields charging times of 10 hours to 1 hour, respectively. The applied current was calculated with respect to the active mass of LFP cathode material, but the capacity was calculated with respect to the mass of the entire battery composite. The corresponding energy density was calculated by integrating the area under each discharge curve in Figure 3a according to the following equation:

$$Energy\ Density = \frac{I}{M}\int_0^t V(t)dt$$

Here, *I* is the constant current applied during the galvanostatic measurements, *M* is the total structural battery composite mass, and *V(t)* is the voltage as a function of time throughout the galvanostatic test. At rates of 0.1 C, the carbon fiber battery composite exhibited capacity of ~30 mAh/g, which results in total energy density of 36 Wh/kg. Despite the higher resistivity of carbon fiber current collectors compared to traditional Cu or Al current collectors, the entire battery panel was cycled up to rates as high as 1.0 C, and displayed a capacity of 7 mAh/g with an energy density of 10 Wh/kg at the highest rates. The composite structural battery panel was also subjected to extended cycling at a rate of C/2 and had an energy density of 18 Wh/kg, even after 50 cycles (Figure 6.2d).

A key characteristic of a structural battery is the need for the material to exhibit reversible battery performance under mechanical loading that is the hallmark of a multifunctional material.

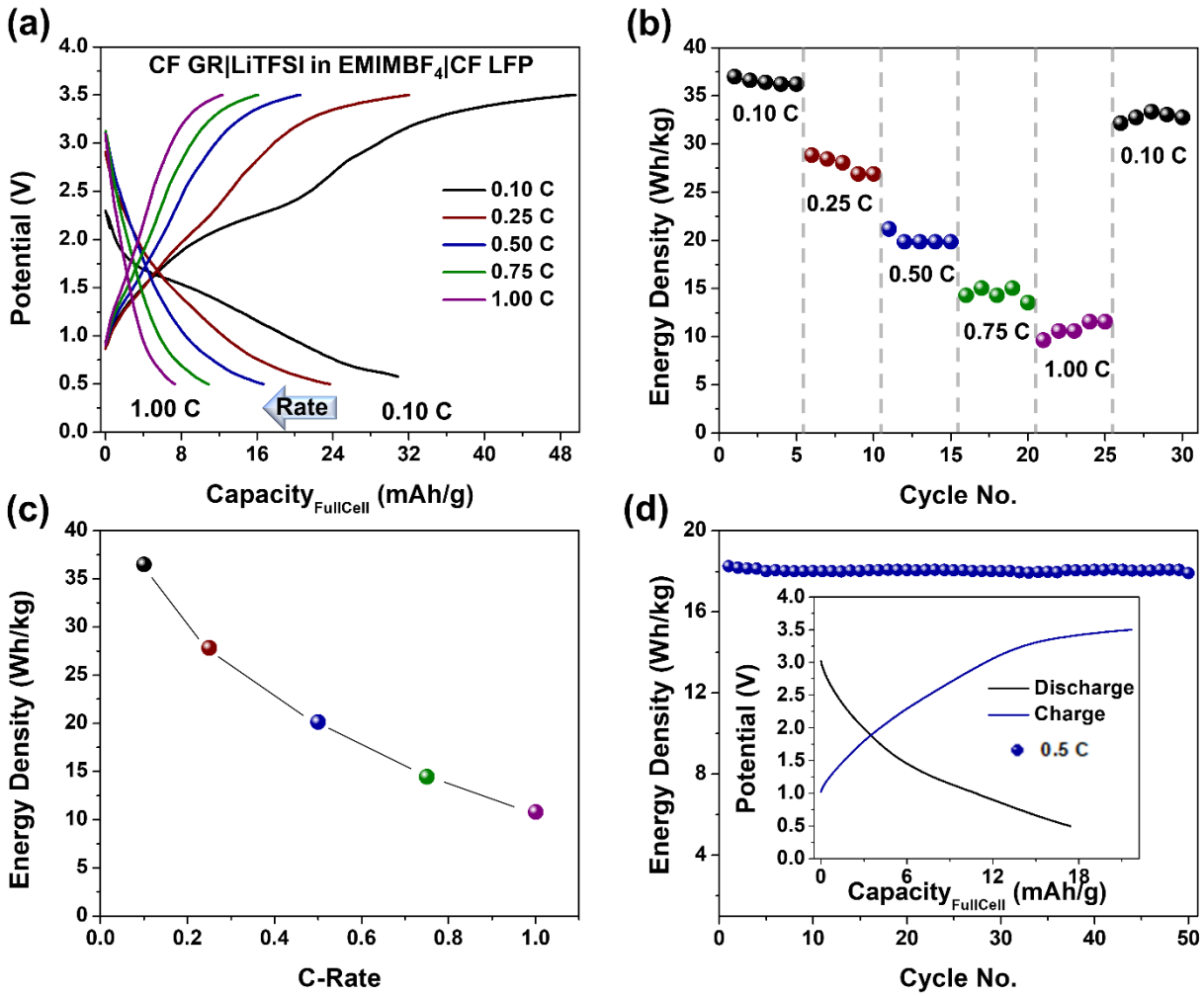

Figure 6.2 Galvanostatic testing of carbon fiber composite battery panel, rate study a) first cycle charge discharge curves at each rate, b) corresponding energy density at each rate, c) average energy density at each rate, d) and extended cycling at a rate of 0.50 C with inset of characteristic charge discharge curve after system stabilizes.

To study this we first tested the mechanical integrity of the composite structural battery panel by tensile testing at a strain rate of 2 mm/min (Figure 6.3a). These results support an ultimate tensile stress of 213 MPa with Young's modulus of ~1.8 MPa/(Δl/l). The mechano-electrochemical properties, or the simultaneous testing of mechanical properties and battery electrochemistry, of the composite structural battery panel were also examined through performing galvanostatic charge discharge measurements at a rate of 0.10 C at various points throughout the tensile test.

Charge discharge measurements were initially performed before tensile testing with no applied stress (Figure 6.3d). Then, the composite was loaded to 100 MPa at which point the tensile testing was stopped and galvanostatic charge discharge cycling was performed (Figure 6.3e).

Subsequently, the composite was loaded to near-failure, 200 MPa. Again, charge discharge measurements were taken at 200 MPa (Figure 6.3f). Prior to tensile tests, the galvanostatic curves exhibit a first discharge capacity of 28 mAh/g and energy density of 37 Wh/kg, as summarized in Figure 6.2b, c. After being stressed to 100 MPa, polarization due to stresses in the structural material result in steeper and less well-defined galvanostatic charge-discharge profiles, and the first discharge capacity and energy density decrease to 16 mAh/g and 20 Wh/kg, respectively. Finally, at 200 MPa of tensile stress the polarization due to localized stresses applied to the structural battery composite greatly reduce the performance, yielding sloping charge/discharge curves and a first discharge capacity of 8 mAh/g and energy density of 12 Wh/kg. Importantly, measurements of the performance of these devices after releasing the load resulted in no significant recovery of the performance. We therefore conclude that mechanical stress applied to a structural battery can dictate the resulting capacity and energy density likely due to shear-stress induced delamination at interfaces. As the basic role of a carbon fiber additive to a reinforced composite is to facilitate load-transfer between the epoxy matrix and carbon fiber, the presence of a coated battery material on the carbon fiber that itself is subject to volume changes during charging and discharging presents a new challenge for a stable structural battery material. Specifically, these results emphasize the need for mechano-chemical testing combined with reinforcement strategies across the carbon-battery material-epoxy interface are critical to realize full battery performance under significant mechanical stress. However, our approach that uses coated active material layers on carbon fibers without such reinforcement strategies can be appropriate for structural batteries

exhibiting low-levels of mechanical loading, where mechano-chemical and electrochemical cycling performance are both stable. Nonetheless, this study emphasizes the need for ongoing efforts to propose and design novel interface reinforcement strategies which can facilitate high performing multifunctional materials.

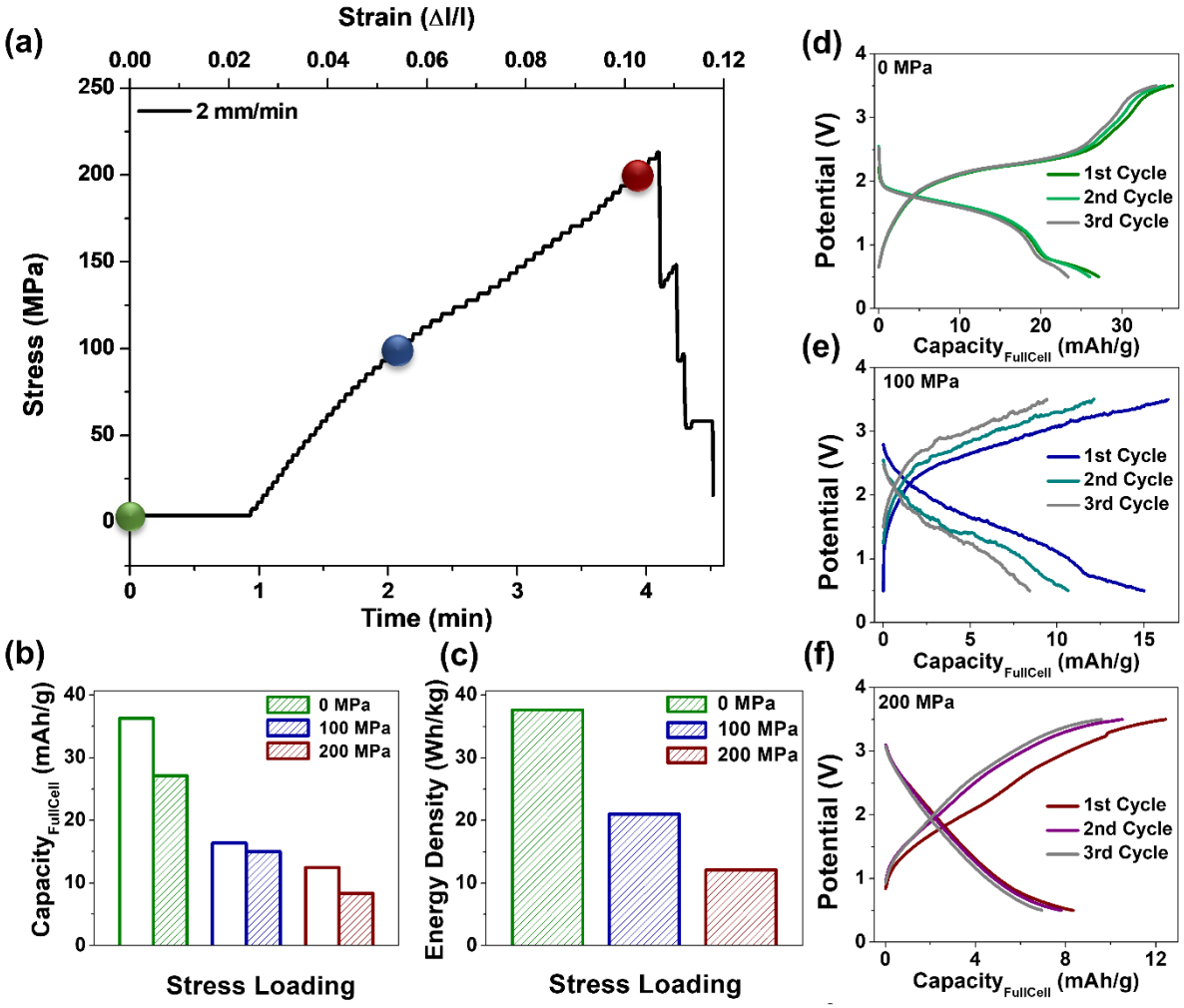

Figure 6.3 Mechano-electrochemical performance of carbon fiber composite battery panels a) stress strain curve of tensile testing, b) charge (outlined bar) and discharge (striped bar) capacity at different stress loadings, c) energy density at different stress loadings, and galvanostatic charge discharge curves at stress loadings of d) 0 MPa, e) 100 MPa, f) 200 MPa.

As the focus of our efforts so far have been around the use of common materials (graphite and LFP) for Li-ion batteries, the novelty in our approach lies in the idea that not only is this the

first air-stable, full-cell structural Li-ion battery reported to date, but the design of this battery provides quantifiable gravimetric performance enhancement to a system it is integrated into. Here, our design leverages the structural composite materials (carbon fibers, epoxy, etc.) to replace the inactive packaging materials in an externally (or internally) situated Li-ion battery pouch cell, such as current collectors, liquid electrolyte, and the pouch. This means that when benchmarking energy storage performance against the *system*, where the system includes structural materials plus the battery, our approach yields a significant gravimetric performance enhancement to the system that comes from this integration strategy. We estimate the maximum gravimetric performance enhancement based on the known energy density and packaging mass of a standard LFP/graphite cell (1.35 Ah cell, Harding Energy) to be ~ 30% in our configuration. Whereas many researchers are focused on strategies to improve the energy densities of batteries, which is proving increasingly more difficulty, this approach shows that effective integration methods can yield improvements to the energy densities of systems containing externally situated batteries.

To further validate this idea, we focused on demonstrating an idealized testbed for this structural battery integration strategy by using these materials as components of a structural frame for a 1 U CubeSat. As shown in Fig. 6.4a, this addresses a key challenge for CubeSat systems as external Li-ion battery packs occupy a significant volume of a 1 U CubeSat assembly. By integrating energy storage into the CubeSat structural frame, the improved gravimetric and volumetric performance of the system allows more volume and mass for additional contents into the CubeSat assembly, enabling improved value for an individual CubeSat mission. Specifically, for the case of 4 structural battery panels assembled into the 1 U CubeSat, each with energy density of 35 Wh/kg, this produces a total energy of ~ 10 Wh, which decreases the total required mass of

external batteries by ~ 30% in this configuration and creates free volume in the CubeSat chassis, pushing closer towards NASA's operational requirements for mission infusion, as illustrated in Figure 6.4a. To demonstrate this approach, we connected 4 - 8.4 cm x 8.4 cm composite battery panels in series in a prototype 3-D printed 1 U CubeSat frame with outer dimensions of 10 cm x 10 cm. The batteries in the panels were connected in series and shown through supporting videos (still shots in Fig. 6.4b and 6.4c) to provide power to both a small industrial fan (Figure 6.4c) and an LED (Figure 6.4b). Whereas CubeSats provide a clear value-driven approach for structural energy storage composites due to the high cost of payload materials (~ $10,000/lb), this approach can be realized in other aerospace or structural systems as well,[243, 244] such as in drones, small

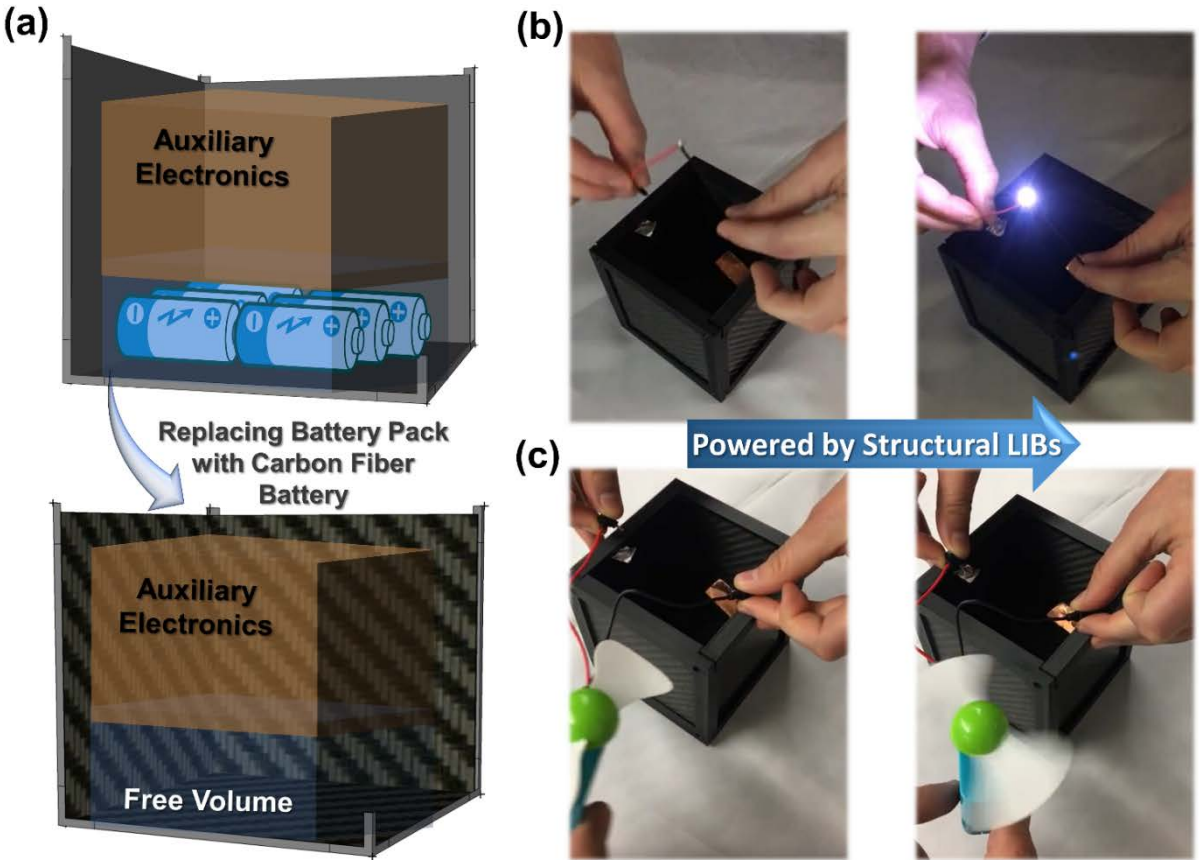

Figure 6.4 Replacing interior external battery pack with structural battery creates free volume within the CubeSat chassis; a). Electrochemical performance of 4 composite structural battery panels in series in a 1U prototype CubeSat frame, b) lighting a LED and c) operating a fan.

UAVs, and microscale robots – all of which are lightweight structural systems which are often bottlenecked by the challenge of integrating external energy storing payloads into the systems.

6.4 Conclusion

In summary, we have demonstrated an approach to directly combine battery processing and composite layup processing into a single step that produces a pouch-free carbon fiber reinforced structural Li-ion battery with energy density relative to all active and inactive battery components > 35 Wh/kg. This is achieved by resourcing the components of the carbon fiber epoxy composite matrix to be the inactive packaging materials for the Li-ion battery, providing a distinct energy storage performance improvement to a system (structural materials + energy storage). This approach, which is the first to demonstrate structural energy storage using Li-ion battery chemistries having practical energy density and cycling durability, gives promise to an alternative pathway to improve the energy density of systems by carefully designed integration strategies, rather than improving the energy density of state-of-the-art commercial battery systems. Our findings in studying the mechano-electrochemical performance of these materials highlights the fundamental ongoing challenge for structural energy storage materials, namely the reinforcement of interfaces spanning carbon fiber – battery material – epoxy resin layers during charging and discharging processes. We further show how these structural battery panels can be coordinated in series into a 1 U CubeSat frame to provide integrated power delivery and reduce the need for heavy on-board battery systems, providing a key value-driven approach for structural energy storage that leverages the performance enhancement of this approach. Looking forward, the processing of structural composite materials that incorporate energy storage capability can change the

technology of the future at a system-level in a manner analogous to how batteries have changed the technology that we use today. Despite ongoing fundamental challenges related to interface design for these materials, our results give promise to practical, lightweight multifunctional structural composites that can be used for the design of next-generation power-integrated technologies.

Acknowledgments

The authors acknowledge Philip Johnson, Nitin Muralidharan, Shaun Daly, Paul Mackey, Lawrence Batterson, Thomas Miller, Charles Langoni, Robert DeVor, Michael Galluzzi, Jose Nunez, Robin Midgett, Melanie Pickett, John Waugh, and Murtaza Zohair for helpful discussions and their assistance during this project. The authors also thank Gary Turner for helping design the CubeSat frame and Mike Lane, Dave McLoughlin, and the NASA prototype shop for their time and assistance. This work was supported by NASA grant number NNX16AT48A, K.M. was also supported by NSF graduate fellowship under grant 1445197.

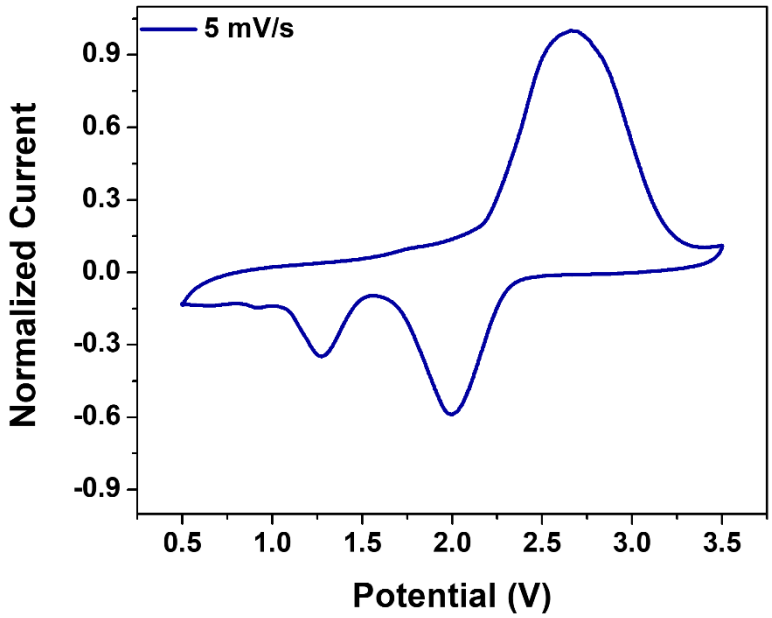

Figure 6.5 Cyclic voltammogram of a CF GR | LiTFSI in $EMIMBF_4$ | CF LFP carbon fiber battery composite.

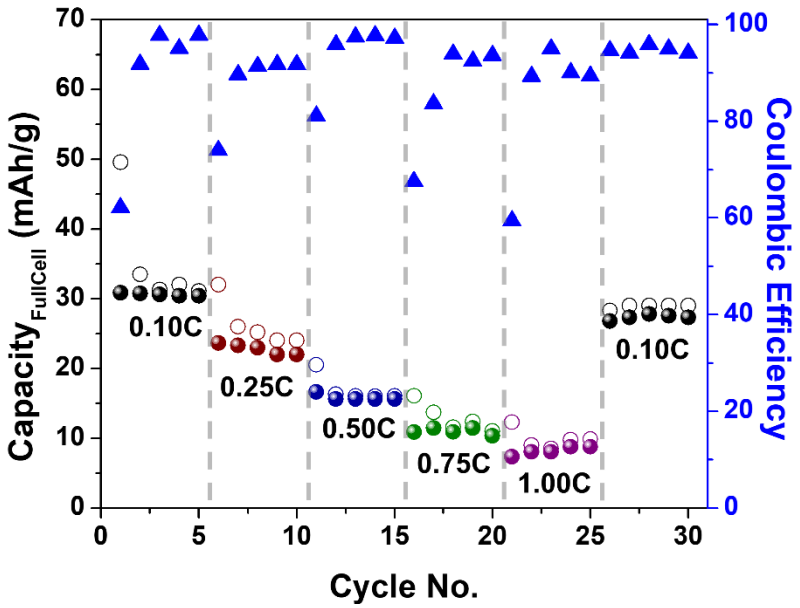

Figure 6.6 Galvanoststic rate study of carbon fiber composite battery panel, capacity at each rate for charge (open circles) and discharge (closed spheres) and corresponding coulombic efficiency.

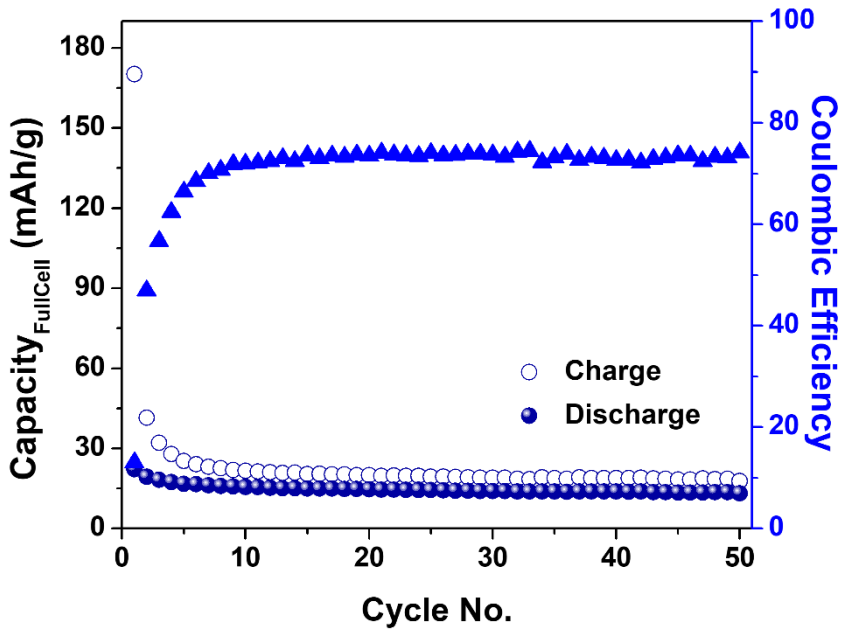

Figure 6.7 Galvanostatic testing at a rate of 0.50 C. Charge (open circles) and discharge (closed spheres) capacity and corresponding coulombic efficiency for each cycle.

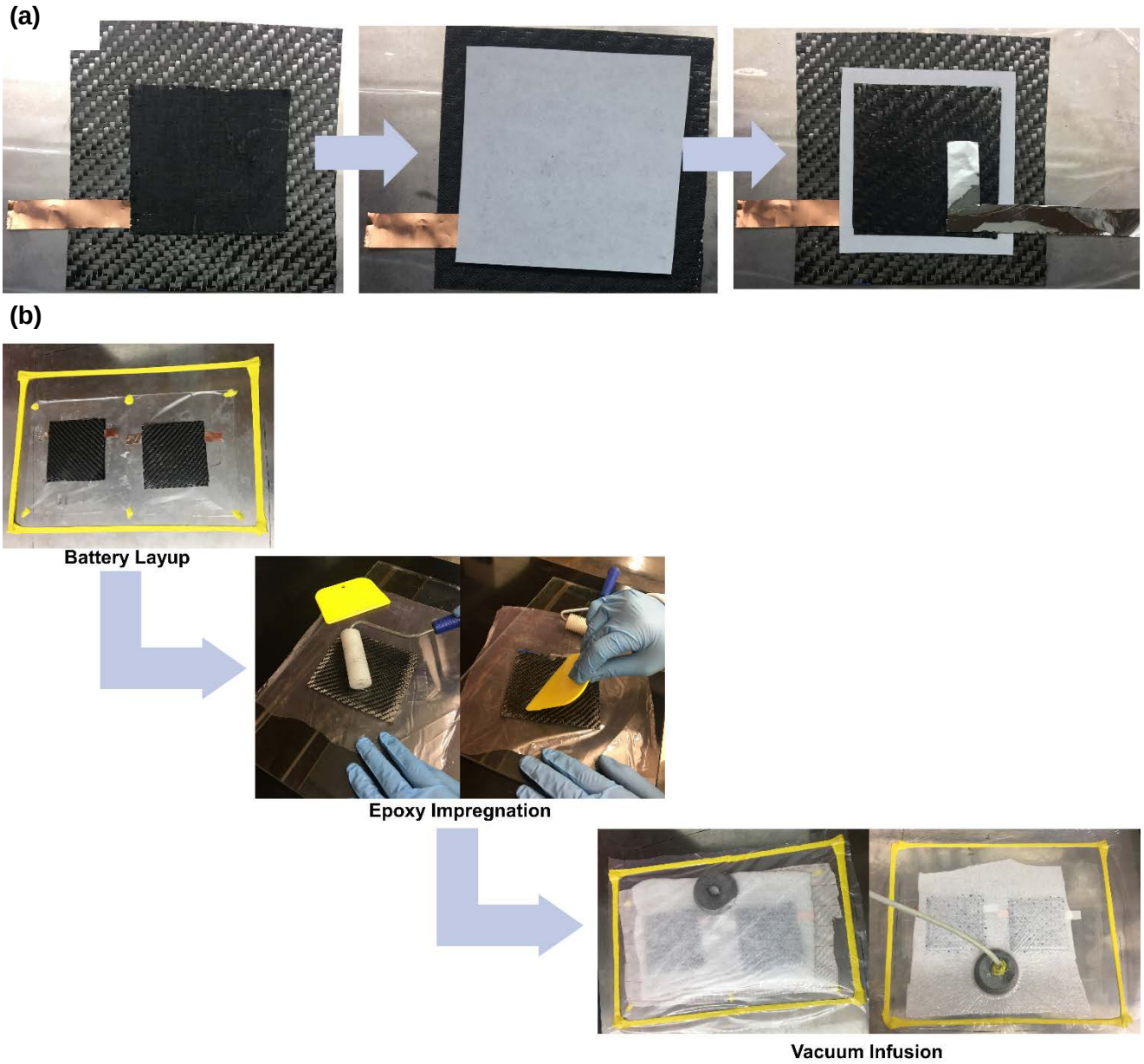

Figure 6.8 Illustration of a) tab integration into pouch cell showing graphite on carbon fiber with copper tab, Whatman glass fiber separator, and $LiFePO_4$ on carbon fiber with aluminum tab and b) carbon fiber battery composite fabrication process.

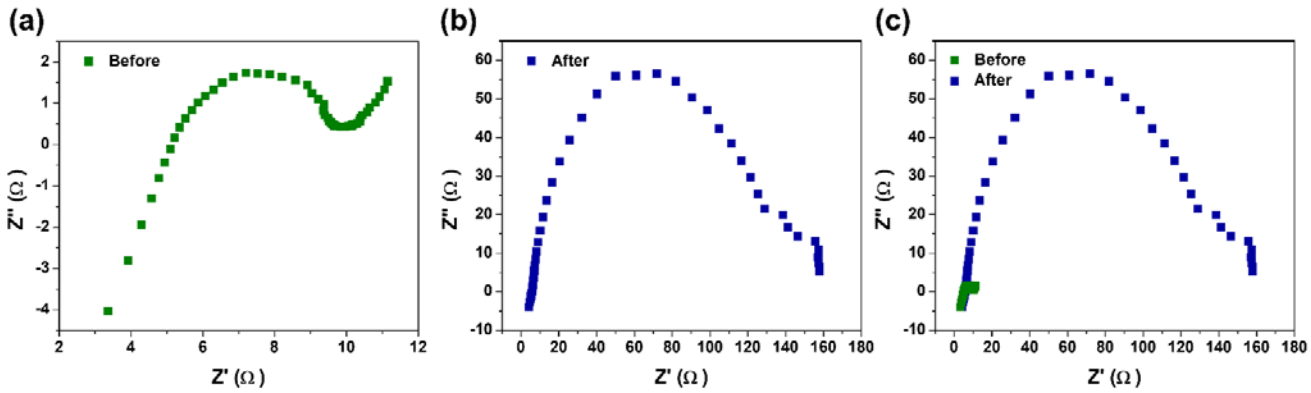

Figure 6.9 Electrochemical impedance spectroscopy of carbon fiber battery composite panels a) before tensile testing, b) after being stressed to 213 MPa, and c) a direct comparison of before and after.

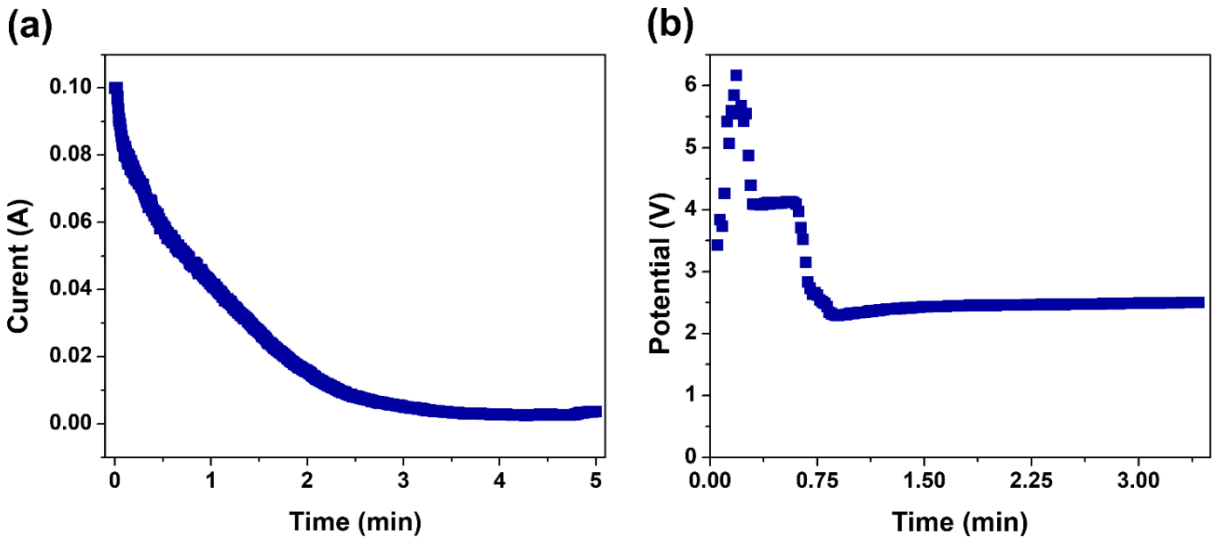

Figure 6.10 In-situ mechano-electrochemical testing a) current response of a potentiostatic test at 3.5 V during tensile testing and b) voltage response after galvanostatically charging to 3.5 V during tensile testing.

Supplementary Video 1

Lighting an LED

CubeSat_LED_compressed.avi

Supplementary Video 2

CubeSat_Fan_compressed.avi

Chapter 7

Polymer Film Stabilized Carbon Fiber Battery Electrode Interfaces for Stable and High Energy Density Structural Lithium-Ion Batteries

Adapted from: K. Moyer, N. Ait Boucherbil, M. Zohair, J. Eaves-Rathert, C.L. Pint, "Polymer Film Stabilized Carbon Fiber Battery Electrode Interfaces for Stable and High Energy Density Structural Lithium-Ion Batteries," *in preparation.*

7.1 Introduction

Whereas the lithium battery has been an enabling device for mobile applications, the basic method for combining the lithium-ion battery into systems has remained unchanged over the past thirty years.[5] This involves materials and electrolytes packaged into self-contained cells, which are then added externally to a system that requires power input. Despite great strides since the conception of the lithium-ion battery to reduce inactive mass,[9] minimize packaging,[11, 245] and streamline manufacturing,[6, 8] performance improvements in batteries have been historically slow. Whereas improved anodes give promise to higher cell capacity,[10, 246, 247] the push to reduce or eliminate cobalt from cathodes as battery production volume scales higher means lower cell voltage,[13, 14] and this brings a push-pull competition toward improved battery performance at the cell level. One alternative idea is to instead focus on the improvement for battery integration into systems, such as designing structural materials that are imbued with capability to store electrical energy.

With this said, structural energy storage represents a growing field of research over the past years. Early studies in this area primarily focused on supercapacitors due to the simplicity of design with two symmetric electrodes, and inspiration building from work on polymer and/or solid battery architectures.[217-219, 248-253] Challenges among these early studies included a lack of clear justification for multifunctional operation and/or performance, and extremely low areal and gravimetric energy storage capability on the order of a few to tens of mF/cm2. Whereas many of these problems continue in this area, recent work by Sun et al.[170] introduce a methodology to benchmark multifunctional advantage of structural energy storage materials, and show an rGO/Kevlar supercapacitor to exhibit improved multifunctional efficiency compared to carbon aerogel/epoxy materials. Moving toward batteries, the challenges for structural batteries become more significant since useful anode or cathode materials exhibit moderate levels of volume change during charging and discharging.[254] This means that interfaces between active materials and current collectors, which are already problematic in commercial cells packaged under compression, are a limiting aspect for the design methodology of structural batteries. Early studies in this area simply encapsulated packaged lithium-ion battery pouch cells into the composite layup process.[228, 255-257] However, such an approach bears no gravimetric advantage to a system, and brings a mechanical disadvantage due to a smooth battery packaging/epoxy interface. Only recently have approaches been demonstrated for direct integration of battery materials into structural composites, but these approaches so far have been limited to either low energy density (relative to *all* active and composite materials) and moderate cycling stability,[226, 230, 237, 258-264] or moderate energy density and low cycling stability.[35] Efforts moving forward in this area require identification and mitigation of mechanically induced degradation mechanisms that arise from

operation without compressive stress due to packaging and with the introduction to external forces on the composite materials.

In this spirit, one effective approach in stabilizing active battery materials from degradation under stresses caused by charging and discharging has been the use of ultrathin coatings. A common way to achieve such coatings has been the use of atomic layer deposition (ALD),[265-268] which additionally provides control on the solid electrolyte interphase formation at the electrode-electrolyte interface. Outside of this, there have been other studies on the utilization of polymer films for battery electrodes.[269-272] Recent work by Shen et al.[273] demonstrates an initiated chemical vapor deposition coating of polycyclosiloxane polymer films onto silicon anodes to facilitate in overall better stability owing in part to mechanical and chemical stabilization at the electrode-electrolyte interface. Moving away from conventional battery configurations that are packaged under compressive stress toward structural battery configurations requiring the battery materials to withstand external stresses is likely to place a greater demand on such methodologies and their role in electrode mechanics.

In this work, we show that for active battery materials coated onto carbon fiber current collectors, a thin PAN coating is effective to "lock-in" the active materials onto the carbon fibers and more effectively distribute stresses in the composite to prevent battery material delamination. We demonstrate the effectiveness of this approach by comparison of structural batteries with and without the PAN polymer coating on the electrodes, where PAN-based electrodes exhibit significantly improved energy density up to 52 Wh/kg relative to active and inactive composite materials as well as cycling performance up to 100 cycles while maintaining > 80% capacity. This work highlights a broad and effective approach to stabilize the mechanical interfaces of battery

electrodes in multifunctional or novel platforms that do not involve external compressive packaging, such as in structural batteries.

7.2 Experimental Details

7.2.1 Electrode Fabrication and Battery Assembly

Carbon fiber (Fibre Glast) was used as the current collector for all electrodes. Lithium iron phosphate (LFP) electrodes consisted of LFP (MTI), conductive carbon black (MTI), multiwall carbon nanotubes (CheapTubes, >95%), and PVDF binder (MTI, >99.5%) in a ratio of 65:20:5:10, respectively. Carbon nanotubes were used as a conductive additive to offset the insulating nature of the carbon fiber current collector and increase the conductivity throughout the cathode.[274] Graphite (GR) electrodes were made with graphite powder < 20 μm (Sigma-Aldrich), conductive carbon black (MTI), and PVDF binder (MTI, >99.5%) in a ratio of 80:10:10, respectively. A polyacrylonitrile (PAN) coating was made by dissolving 2.5 wt% PAN in dimethylformamide (Sigma-Aldrich, 99.8%) and stirring at 70˚C. PAN GR and PAN LFP electrodes were made by coating the GR and LFP electrodes, respectively, with PAN. Celgard 2525 separators were used with 1 M $LiPF_6$ (Sigma-Aldrich, 98%) in ethylene carbonate (sigma-Aldrich, 98%):diethyl carbonate (Sigma-Aldrich, 99%) in a 1:1 volume ratio as the electrolyte. Carbonate solvents were chosen as a control to minimize water contamination issues more heavily associated with other solvents like ionic liquids. Galvanostatic testing was performed on an 8 channel MTI battery testing system and cyclic voltammetry and electrochemical impedance spectroscopy were conducted using a Metrohm Autolab potentiostat/galvanostat.

7.2.2 Carbon Fiber Composite Battery Assembly

The carbon fiber layup process used epoxy (Fibre Glast Developments Corp., System 1000 Laminating Epoxy Resin Standard Part Kit 1000/1025), a roller, squeegee, and carbon fiber (Fibre Glast). 4 pieces of 6 cm x 6 cm carbon fiber were impregnated with epoxy. The composite battery was then assembled similarly to;[35] two of the epoxy-impregnated carbon fiber squares GR|CF electrode with and without PAN, separator, LFP|PAN electrode with and without PAN, and two-epoxy impregnated carbon fiber squares. Nickel tabs (MTI, 99.99%) were used for the GR|LFP electrode and aluminum tabs (MTI, 99.99%) were used for the LFP|PAN electrode.

7.2.3 Electrode Characterization and Mechanical Testing

All electrode materials were examined by scanning electron microscopy using a Zeiss Merlin SEM. An Instron mechanical tester was used to perform lap shear tensile tests and carbon fiber composite tensile tests. All samples underwent tensile tests at a strain rate of 2 mm/min.

7.3 Results & Discussion

In order to assess the interface properties of the electrode design, full-cells using carbon fiber current collectors with graphite anodes and lithium iron phosphate cathodes (GR|LFP) were made with and without the addition of a PAN interface (Figure 7.1a). Material selection is fundamental for both the mechanical structure and electrochemical properties. Carbon fiber is an excellent structural material due to its lightness and mechanical strength and the way in which the weave architecture evenly distributes stress throughout the matrix.[226, 230, 249] Furthermore, carbon fiber can also function as an energy storage material and current collector.[248, 262, 263, 275] There are reports of polyacrylonitrile (PAN) based carbon fiber as anodes for structural batteries that resulted in mass and volume savings.[237, 260, 261] Using carbon fiber as a current collector in a Li-ion battery reduces up to 15% of the cell mass compared to metal current collectors which is advantageous

for offsetting the mass penalty of incorporating battery systems in composites.[143] While plain carbon fiber has low electrochemical cycling reversibility,[258, 259] it is an excellent platform for mechano-electrochemical energy storage and cyclability can be enhanced by adding graphite as an anode material on the carbon fiber current collector.[35] This study focused on electrode design that has the promise to be integrated into a mechano-electrochemical system.

When carbon fiber is subjected to a mechanical force, shear stress is transferred from the carbon fiber to the active battery material, resulting in material delamination. If the electrode is

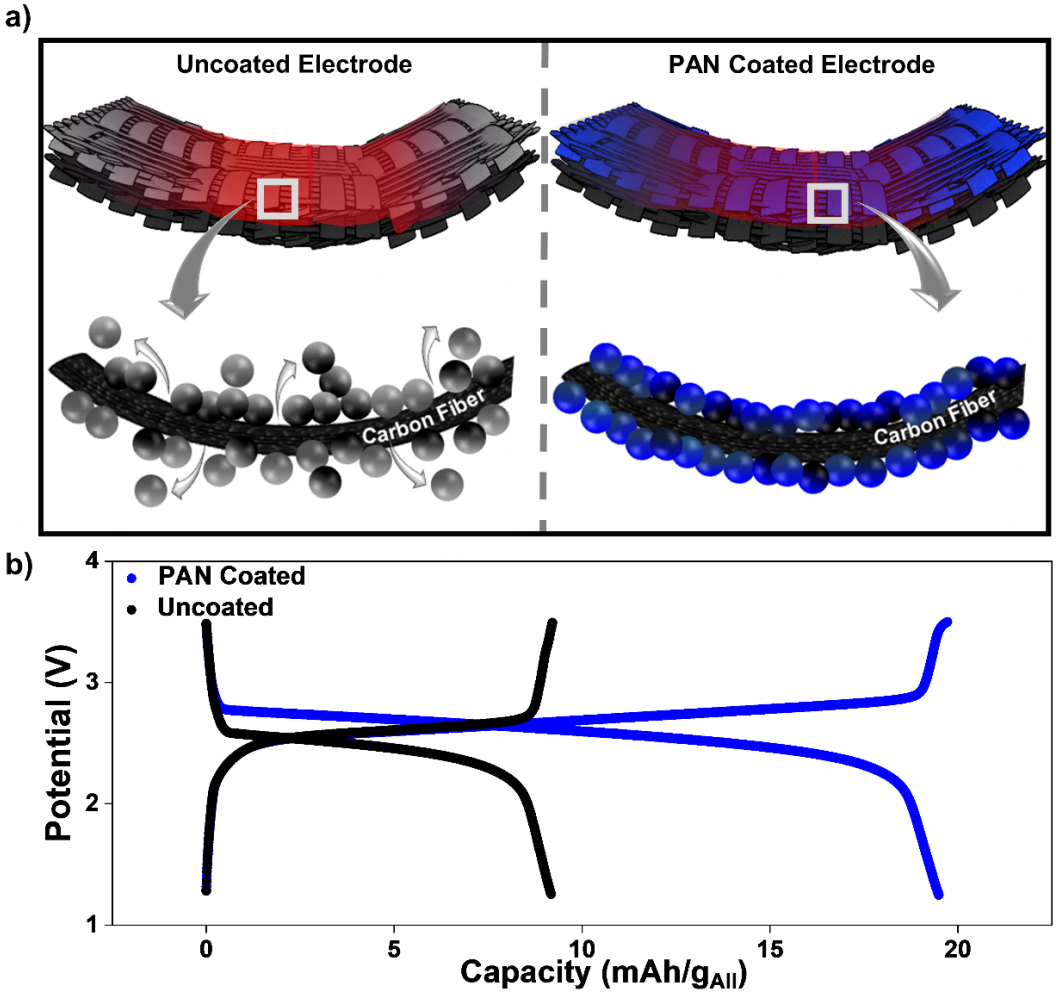

Figure 7.1 a) Scheme illustrating stress distribution and material delamination in carbon fiber structural battery electrode with and without a PAN coating and b) 100th galvanostatic charge discharge cycle at 0.1 C for uncoated (black) and PAN coated (blue) carbon fiber GR|LFP full cells.

subjected to a concentrated stress upon bending (Figure 7.1a), active electrode material delaminates from an uncoated electrode surface and electrochemical performance significantly degrades over the course of 100 cycles, the 100th cycle at 0.1 C is shown in Figure 7.1b. The addition of a PAN coating helps increase the adhesion strength between the carbon fiber and electrode material,[276] minimizing electrode material delamination from the carbon fiber and facilitating contact of the active electrode material with the carbon fiber (Figure 7.1a). Enhanced contact between the interphase more evenly distributes stress throughout the woven network which also improves electrochemical cycling. The 100th cycle at 0.1 C for PAN GR|LFP electrodes is shown in Figure 7.1b and is ~2 times the capacity with respect to total mass compared to the GR|LFP electrodes.

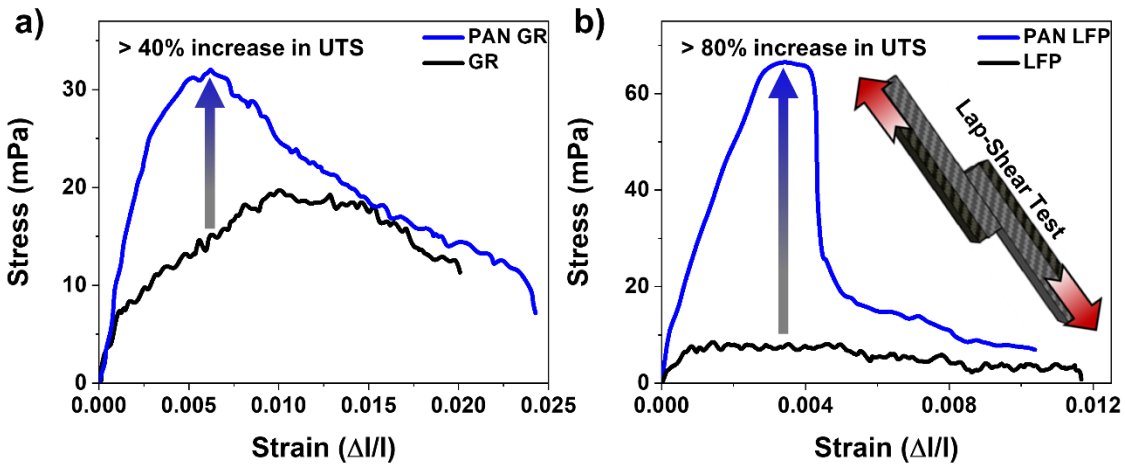

Figure 7.2 Lap shear tests at rate of 2mm/min for a) GR and b) LFP electrodes with and without PAN, and inset of lap-shear test scheme.

The addition of PAN improves the interfacial structure by helping transfer mechanical forces to the fiber and improving the interlaminar shear stress which minimizes material delamination. Lap-shear tests were performed for both GR and LFP electrodes with and without PAN (Figure 7.2a-b). The addition of PAN for the GR electrode increased the ultimate tensile

strength by >40% and that of the LFP electrode by >80%. The interface properties between the carbon fiber and surrounding composite matrix are significantly affected by the interfacial structure.[277] The properties are primarily based on microstructure and performance of an interphase between the fiber and matrix, an area where the fiber and matrix phases are chemically or mechanically combined.[278] In the case of a structural battery, the active battery materials both chemically and mechanically interact with the carbon fiber current collector as intercalation reactions and ion diffusion occurs within that area. The interphase between the fiber and matrix provides a critical role in binding and transferring forces to the fiber which, in turn, determines the mechanical properties of the composite. There are countless modes of failure, but most begin by initial uniform elastic deformation followed by local fracture of the electrode coating at which point the stress is transferred from the carbon fiber to the electrode coating in shear.[279] Consequently, the electrode strain is produced mainly at the carbon fiber surface with a non-uniform distribution leading to failure.[280] The addition of a PAN interface helps minimize areas of concentrated stress by uniformly distributing mechanical forces throughout the system. To examine the electrochemical performance of the electrodes with and without PAN, cyclic

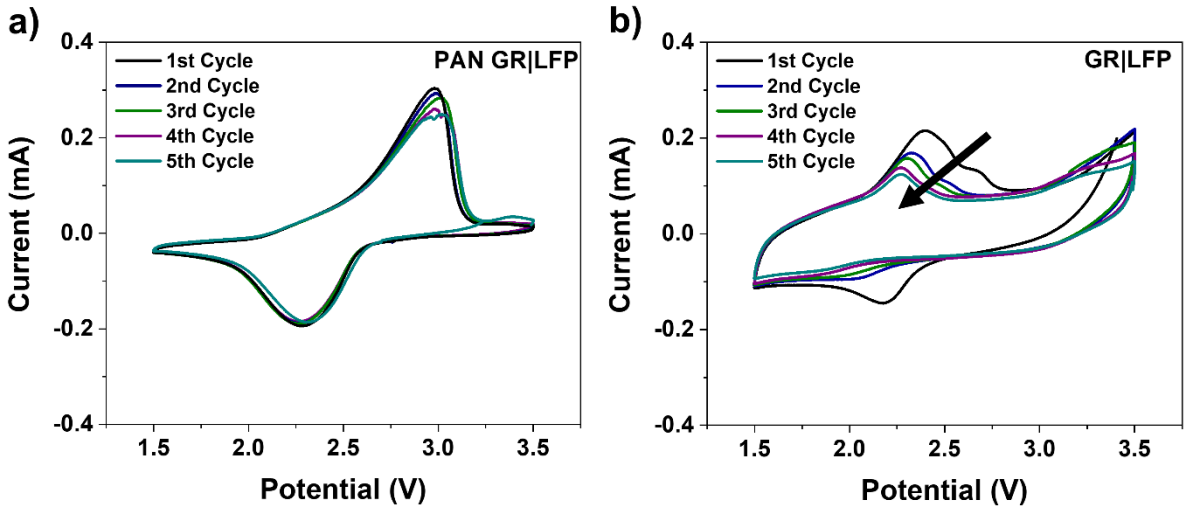

Figure 7.3 Cyclic voltammograms of a) PAN GR|LFP and b) GR|LFP full cells.

voltammograms (CVs) were conducted at 5 mV/s for both PAN GR|LFP (Figure 7.3a) and GR|LFP electrodes (Figure 7.3b). There are distinct reversible peaks that resemble a faradaic reaction with minimal degradation over 5 cycles for the PAN GR|LFP whereas the redox peaks are less reversible and there is a significant peak shift indicating material delamination for GR|LFP electrodes. After, the 1st cycle, the reduction peak for the GR|LFP electrodes is less pronounced, which indicates that the Li-ions cannot as easily access the host LFP structure. Consequently, this CV appears more capacitive in nature and less reversible as there are fewer available sites for charge to be stored within the LFP cathode due to material delamination over the course of cycling. Material delamination is further evident by the magnitude in the peak shift for each electrode.[281] Between the 1st and 5th cycles, the peaks only shifted by 6% for the PAN GR|LFP but shifted >75% for the GR|LFP electrodes. This peak shift is also accompanied by a reduction in peak current associated with a decrease in electroactive surface area, further confirming loss of electrode material throughout cycling.

Electrochemical data further supports the influence of PAN on the electrode design (Figure 8.4). When PAN is added to the electrodes (Figure 7.4a), the initial capacity is greater than without PAN (Figure 7.4b). The material adhesion to the carbon fiber is enhanced with the addition of PAN, and consequently, less material is lost during cell assembly and during initial solid electrolyte interphase formation, leading to a larger initial capacity. The capacity retention of the PAN GR|LFP is >80% whereas that of the GR|LFP is <64% after 100 cycles at 0.1 C (Figure 7.4f). Similar trends in performance were observed during half-cell cycling and can be found in Figures 7.5-7.11. GR|Li and LFP|Li half-cells with the addition of PAN had improved capacity retention and cycling compared to those without the addition of a polymer layer.

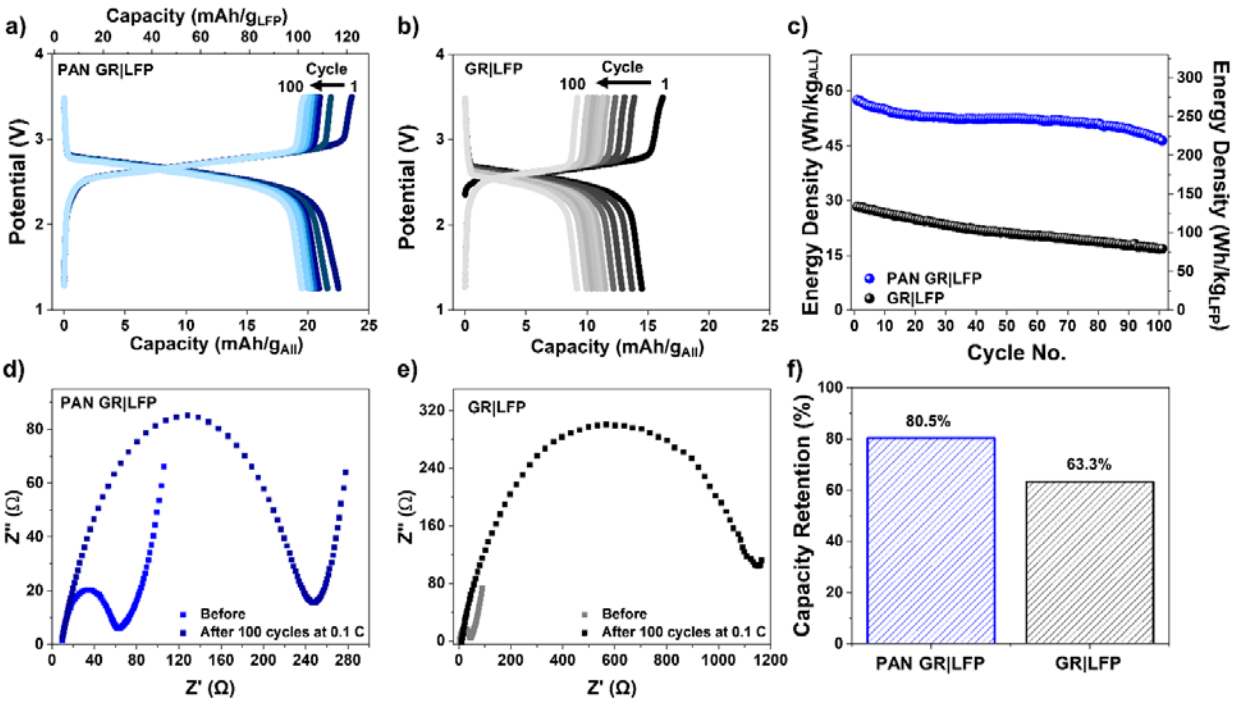

Figure 7.4 Charge discharge curves of every 10th cycle of galvanostatic cycling at 0.1 C for a) PAN GR|LFP and b) GR|LFP full cells, c) energy density vs cycle number with respect to total mass (left y-axis) and LFP active material (right y-axis), electrochemical impedance spectroscopy of d) PAN GR|LFP and e) GR|LFP full cells before and after 100 cycles at 0.1 C, and f) capacity retention over 100 cycles at 0.1 C.

The average energy density with respect to all components over 100 cycles for PAN GR|LFP electrodes was 52 Wh/kg, more than two times greater than the GR|LFP electrodes with an energy density of 21 Wh/kg. The energy density was calculated with respect to the mass of all components, inactive and active material including the carbon fiber (Figure 7.4c). Electrochemical impedance spectroscopy was also performed to probe the kinetics of the electrode process and interface properties with and without PAN before and after cycling. PAN containing electrodes have been shown to have the lowest charge transfer resistance R_{CT} compared with other polymer binders due to the polar nitrile groups which have increased material adhesion and lower charge transfer resistance.[276] The initial R_{CT} with PAN was 60 Ω while that without PAN was 45 Ω, a

slight increase in comparison to the change in charge transfer resistance after cycling. The change in interfacial resistance after cycling with no PAN (R_{CT} ~ 1160 Ω) (Figure 7.4e) was 83% greater than with the addition of PAN (R_{CT} ~ 250 Ω) (Figure 7.4d) further proving material delamination. This increase in charge transfer resistance after cycling is commonly observed in Li-ion battery systems and is attributed to cell aging and material delamination.[282] PAN improves the interphase

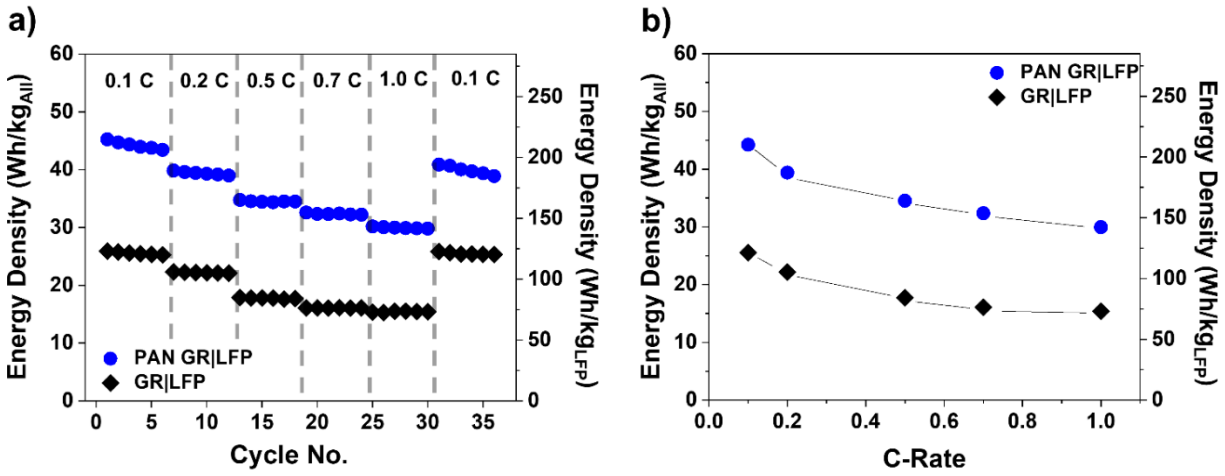

Figure 7.5 Rate study a) energy density with respect to total mass at each rate (left y-axis) and with respect to LFP active material (right y-axis) and d) average energy density with respect to total mass at each rate (left y-axis) and with respect to LFP active material (right y-axis).

between the fibers and the matrix which minimizes material delamination, resulting in a lower R_{CT} after cycling and enhanced electrochemical performance.

Further, a rate study was performed to probe the extent of the rate capability of the electrode design. The capacity and energy density were calculated with respect to all electrode components; active materials, carbon fiber, separator, and are greater at each rate for PAN GR|LFP than GR|LFP Energy density versus cycle number is shown in Figure 7.5a for six cycles at each rate for both PAN GR|LFP and GR|LFP electrodes. The energy density for each electrode chemistry is summarized in Figure 7.5b. For the PAN GR|LFP electrodes the energy density was 44 Wh/kg at

0.1 C, 39 Wh/kg at 0.2 C, 34 Wh/kg at 0.5 C, 32 Wh/kg at 0.7 C, and 30 Wh/kg at 1C. The energy density of the GR|LFP electrodes was 25 Wh/kg at 0.1 C, 22 Wh/kg at 0.2 C, 17 Wh/kg at 0.5 C, 16 Wh/kg at 0.7 C, and 15 Wh/kg at 1C. The charge discharge curves for the 2nd cycle at each rate are shown in Figure 7.14. For the GR|LFP electrodes, there is a lower capacity retention between each rate compared to the PAN GR|LFP electrodes due to the increased material delamination without PAN. Adding a PAN layer to the active material/carbon fiber interface helps reduce material delamination and enhances the ability to store more charge and energy per unit mass with respect to all material, inactive and active components. Overall, this electrode design is a platform enhancing the interface properties of structural battery composites. To evaluate the mechanical properties of these electrodes for a structural battery, composites were fabricated using PAN coated electrodes and tensile tests were performed (Figure 7.17).

7.4 Conclusion

In summary, here we have demonstrated how the addition of a PAN surface coating on carbon fiber electrodes with active battery material can improve electrodes with capacity retention >80% over 100 cycles. These electrodes also boast meaningful energy densities with respect to all active and inactive materials of 52 Wh/kg. The addition of PAN to the electrodes helps improve the distribution of stress within the interphase between the fibers and battery material, enhancing mechanical and electrochemical performance. Interfacial engineering of the electrode is a platform for improving structural battery design for applications ranging from drones, load-bearing infrastructure, satellites, and electric vehicles.

Acknowledgments

The authors thank Alex Stephens, Jacob Fine, Elyssa Ferguson, and Ezra Brody for helpful discussions, Robin Midgett for use of the Instron mechanical tester, and the VINSE laboratory facilities for use of the SEM. K.M. is supported by NSF 1445197.

7.5 Appendix

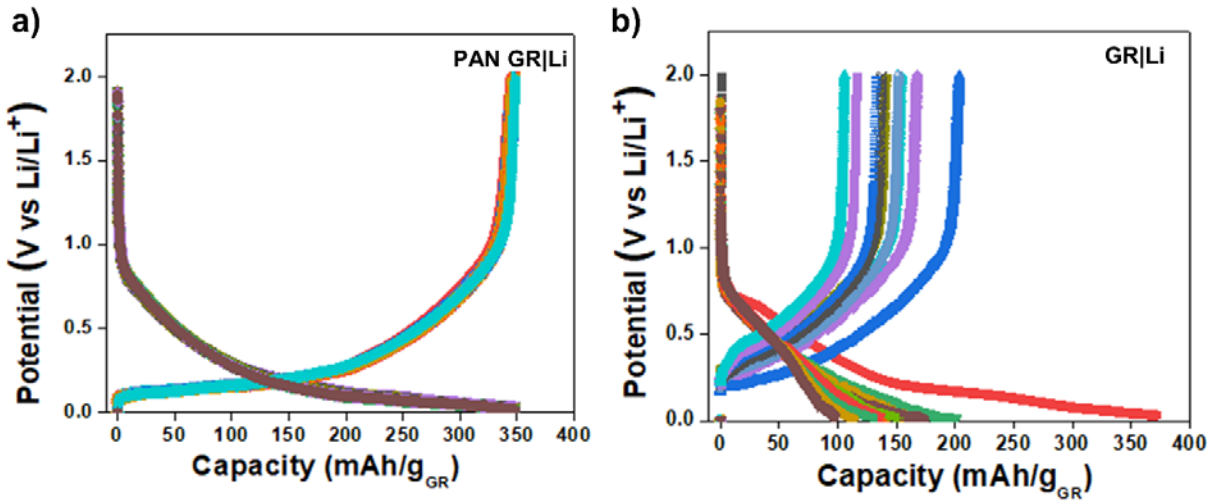

Figure 7.6 Galvanostatic half-cell cycling at 0.1 C for 100 cycles. Every 10th cycle is shown for a) PAN GR|Li and b) GR|Li electrodes. Capacity is with respect to GR active material

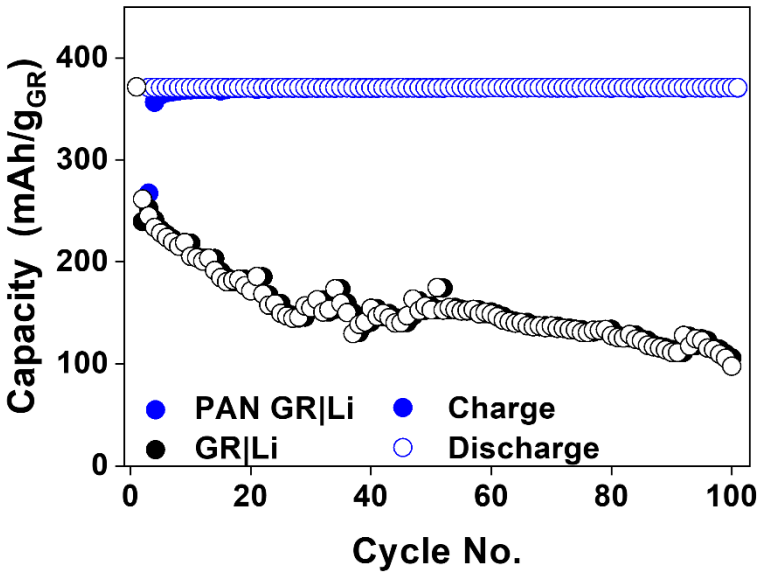

Figure 7.7 Half-cell capacity vs cycle number for 100 cycles at 0.1 C for PAN GR|Li and GR|Li electrodes. Capacity is with respect to GR active material.

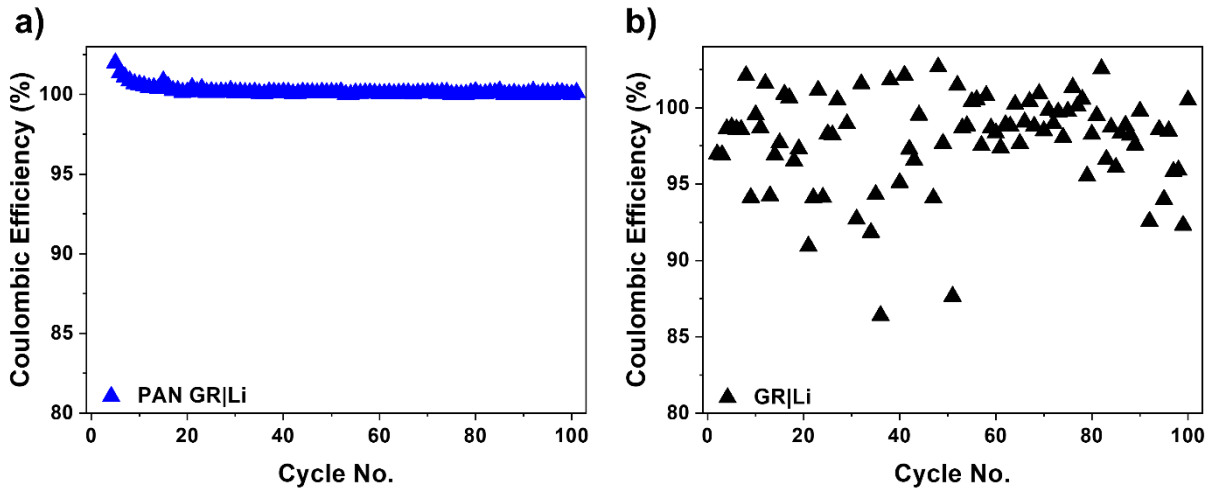

Figure 7.8 Coulombic efficiency vs cycle number for 100 cycles at 0.1 C of a) PAN GR|Li and b) GR|Li half-cells.

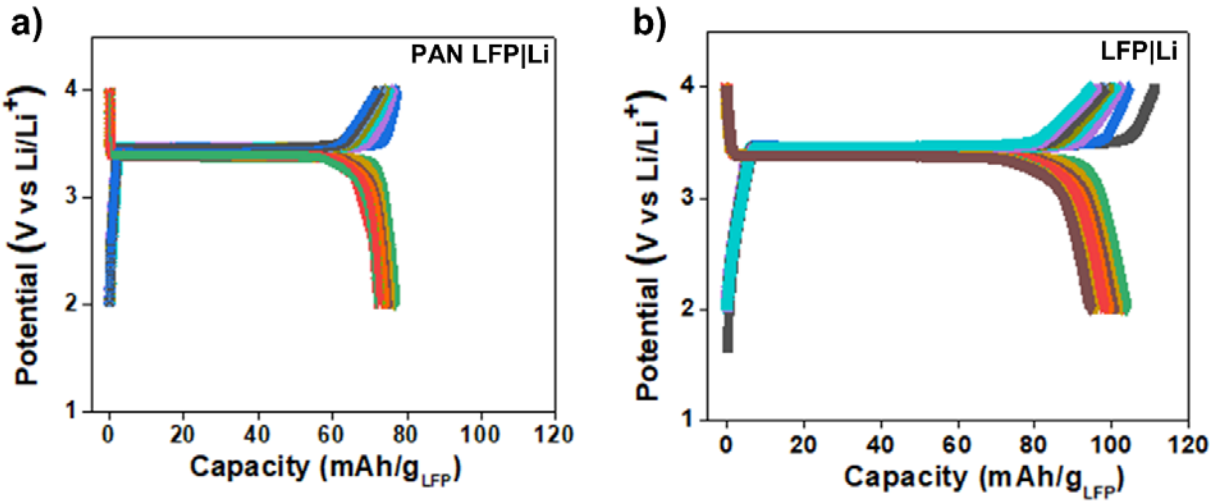

Figure 7.9 Galvanostatic charge-discharge curves of every 10th cycle for half-cells cycled at 0.1 C for 100 cycles for a) PAN LFP|LI and b) LFP|Li electrodes. Capacity is with respect to active material of LFP.

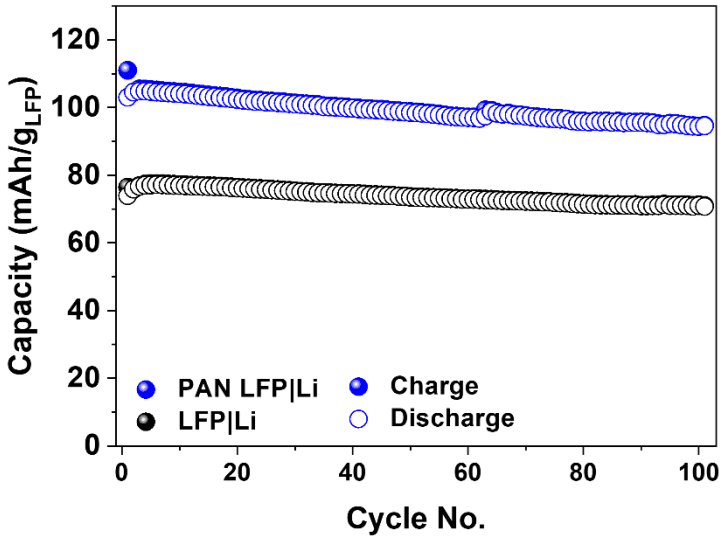

Figure 7.10 Capacity with respect to LFP active material vs. cycle number for 100 cycles at 0.1C for PAN LFP|Li and LFP|Li half-cells.

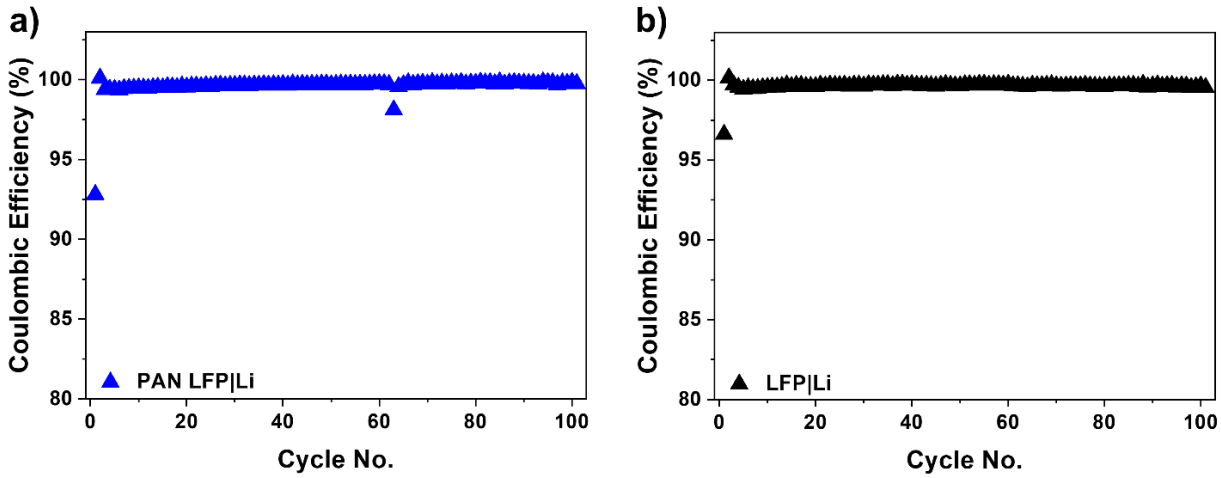

Figure 7.11 Coulombic efficiency for half-cells tested at 0.1 C for 100 cycles for a) PAN LFP|Li and b) LFP|Li electrodes.

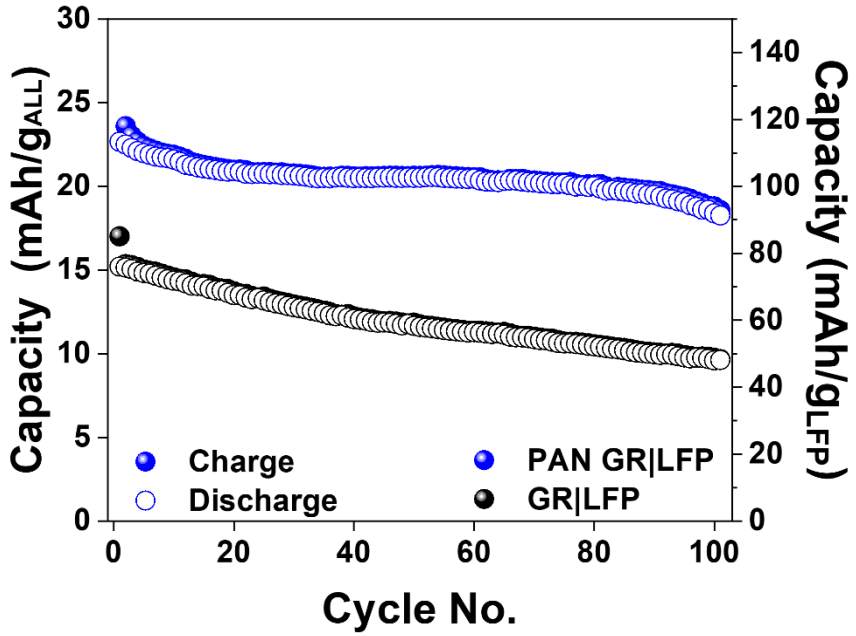

Figure 7.12 Coulombic efficiency for half-cells tested at 0.1 C for 100 cycles for a) PAN GR|LFP and b) GR|LFP electrodes.

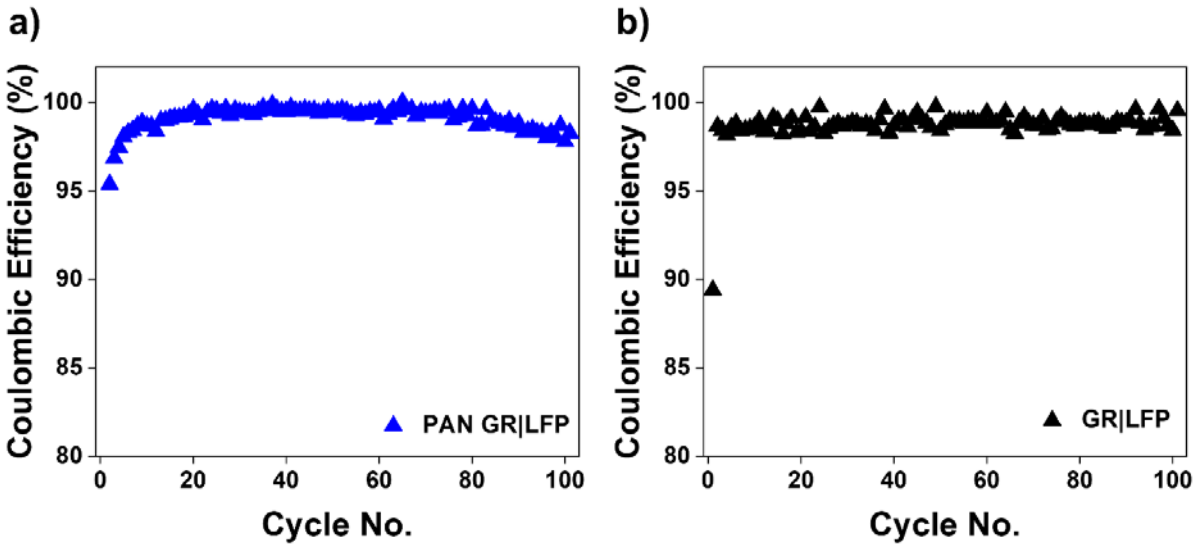

Figure 7.13 Coulombic efficiency vs cycle number for galvanostatic cycling of a) PAN GR|LFP and b) GR|LFP electrodes at 0.1 C for 100 cycles.

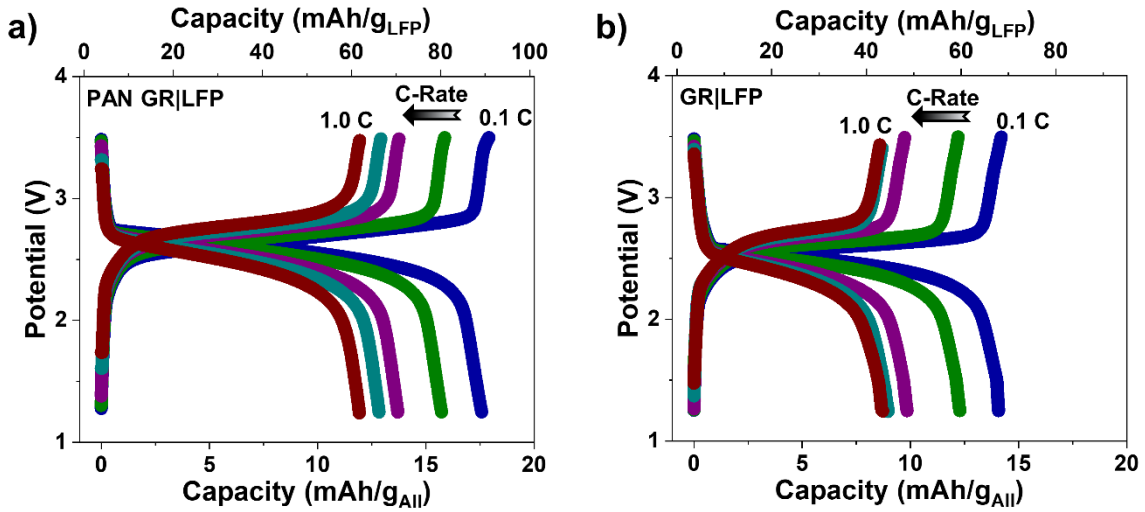

Figure 7.14 Rate study at rates of 0.1, 0.2, 0.5, 0.7, 0.1 C. 2nd cycle charge-discharge curves at each rate for a) PAN GR|LFP and b) GR|LFP.

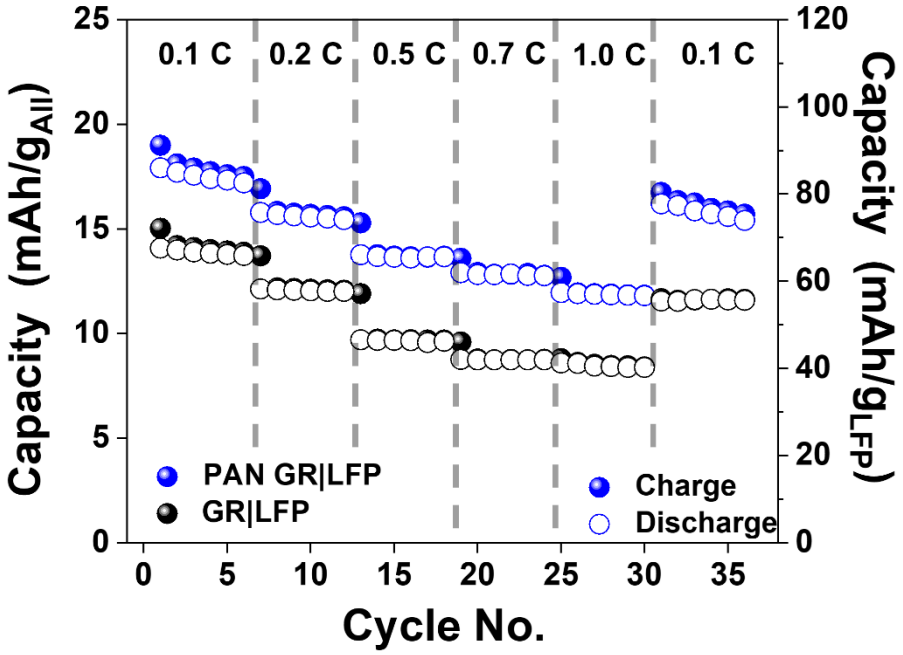

Figure 7.15 Rate study for PAN GR|LFP and GR|LFP full-cell electrodes at 0.1 C, 0.2 C, 0.5 C, 0.7 C, and 1.0 C. Capacity with respect to all mass, inactive and active material, (left y-axis) and with respect to LFP active material (right y-axis).

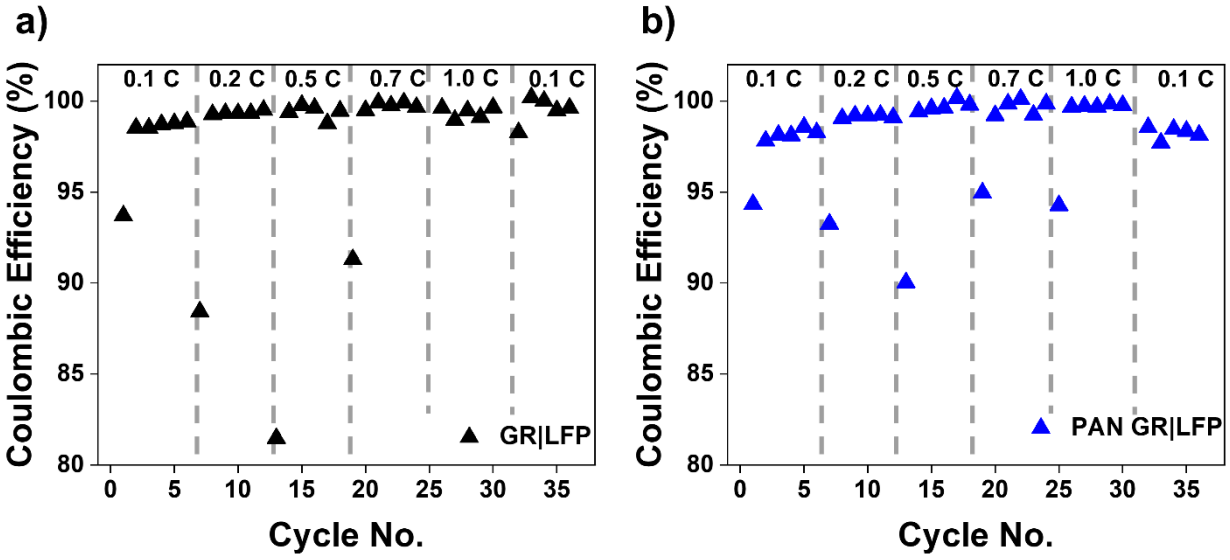

Figure 7.16 Coulombic efficiency vs cycle number for rate study of a) PAN GR|LFP and b) GR|LFP full-cell electrodes.

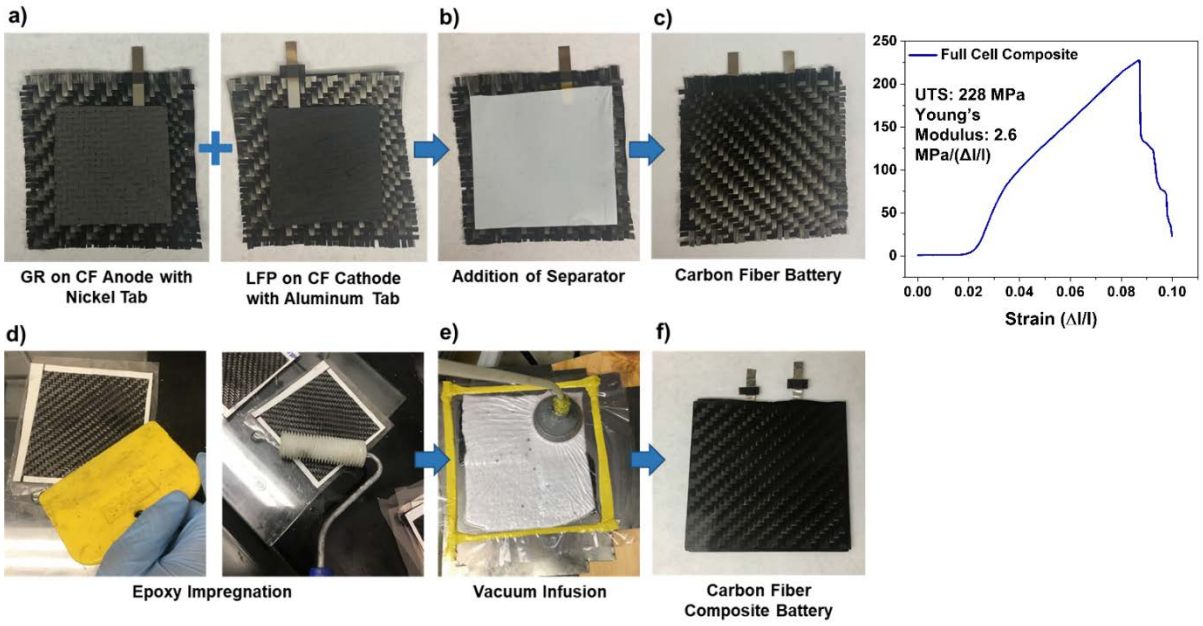

Figure 7.17 Composite layup process: a) GR anode on CF current collector with nickel tab and LFP cathode on CF current collector with aluminum tab, b) addition of separator, c) carbon fiber battery, d) epoxy impregnation, e) vacuum infusion process, f) carbon fiber composite structural battery, and g) tensile testing of composite structural battery.

Chapter 8

Conclusions and Future Outlook

8.1 Conclusions

In summary, this research demonstrates a sustainable platform to design next-generation energy storage systems. Electrochemical capture and conversion of carbon dioxide presents a novel alternative to traditional carbon nanomaterial synthesis that opens the door to large-scale, environmentally friendly production of CNTs. These CNTs can then be integrated into energy storage devices using various techniques, such as electrophoretic deposition, to augment battery performance and help drive towards higher energy and power density while mitigating the carbon footprint of the LIB. Herein I have shown how CNTs can help create a percolative pathway for ion transport through high areal loading electrodes, enable charge transport for high rate performance, and overcome the resistive nature of alternative current collectors to facilitate structural battery development.

In order to better understand the nucleation and growth mechanism of CNTs during liquid-phase electrochemical growth, chapter 2 explored the kinetics and rate-limiting step of the electrolytic reduction of CO_2 to CNTs. In most techniques to grow carbon nanotubes (CNTs), the rate-limiting kinetics of growth are coordinated to the catalyst particle and its reaction to break down hydrocarbon species to form CNTs. Here I demonstrated that in the electrochemical conversion of atmospheric carbon dioxide into valuable CNTs, the rate-limiting step responsible for the onset of catalytic growth and the resulting properties of the CNTs, including diameter and crystallinity, is based upon the activity of the oxygen evolution electrode instead of the activity of

the carbon evolution electrode. These findings were consistent across two separate sets of experiments where the oxygen evolution activity was changed both by the chemical composition of the anode as well as the size ratio of the anode to cathode with a fixed anode composition. In all cases, poor oxygen evolving anodes inhibited catalytic growth altogether, but as the oxygen evolution activity of the anode was increased the catalytic growth of CNTs at the cathode yielded higher crystallinity and smaller diameter. This is explained in the context of sluggish diffusion of oxide species between cathode to anode, and the impact of the buildup of oxide species at the cathode surface with limited oxygen evolution activity at the anode. This work revealed a unique cooperative effect between transport and the onset and effectiveness of catalytic growth that is necessary to understand to produce size-controlled and high quality crystalline high-valued carbon nanomaterials from CO_2 mitigated from the air.

Then, I explored how CNTs can be uniformly integrated into energy-storage devices in a range of different architectures by electrophoretic deposition. Chapter 3 examined how three-dimensional (3-D) current collectors in lithium-ion batteries with high areal loading of cathode materials enabled reduced packaging weight and cost compared to planar current collector materials. Here, I demonstrated the use of EPD as a route to prepare thick cathode assembles in 3-D scaffolds using $LiFePO_4$ with areal loadings measured from 2 mg/cm^2 and up to 20 mg/cm^2 in conductive carbon cloth materials. Findings demonstrated the $LiFePO_4$ cathodes with areal capacity up to ~2.4 mAh/cm^2 and minimal decay (<0.11%) per cycle. This emphasized EPD as both a technique to overcome the limitations of conventional manufacturing approaches in scaling to 3-D collector architectures for improved cell-level energy density, but also a route to transition away from costly NMP processing toward cheaper, less toxic solvents, such as ethanol as was demonstrated in this study.

Chapter 4 built upon the work in chapter 3 and further investigates EPD as a technique widely used for high throughput industrial processes. Here EPD was shown as a route to manufacture high areal capacity battery electrodes with multiwall carbon nanotubes that enabled operation at high rates. Non-toxic, quick-drying acetone was used as an EPD solvent to fabricate $LiFePO_4$ cathodes with high areal loadings of 50 mg/cm^2. Higher electrode mass loadings substantially contribute to increasing the energy density while minimizing the ratio of inactive to active components. This work highlighted the electrochemical performance of high areal loading EPD manufactured electrodes with capacities up to ~8 mAh/cm^2 and ability to perform at rates as high as 2 C. EPD is a promising technique to manufacture the next generation of nanoarchitecture electrodes with high energy density without compromising rate capability.

System-level performance of CNTs was further explored in chapter 5 to enable fast charge transport in alternative ion batteries to synthesize a battery/supercapacitor hybrid. Here I demonstrated a full-cell battery design that bridged the energy density and rate capability between that of supercapacitors or pseudocapacitors with that of traditional lithium-ion batteries. This was accomplished by pairing an anode that enabled ultrafast ion co-intercalation, an open framework cathode that allowed rapid ion diffusion, and linear ether-based electrolyte that sustained cell-level stability and high rate performance. This platform was shown to be suitable for both sodium and potassium batteries using graphite as the co-intercalation anode, and Prussian blue as the open framework cathode. Devices from this study exhibited active material energy densities >100 W h kg^{-1} with power density >1000 W kg^{-1} with cycling durability approaching ~80% energy density retention over 2000 cycles. This work brought together state-of-the-art concepts for fast-charging batteries into a full-cell configuration.

Chapter 6 explored a multifunctional battery platform where lithium-ion battery active materials were combined with carbon fiber weave materials to form energy storage composites using traditional layup methods. This design utilized epoxy resin as a packaging medium for the battery and the carbon fibers as both a conductive current collector and structurally reinforcing layer. These composites exhibited energy density surpassing 35 Wh/kg relative to combined active and inactive composite materials, stable full-cell cycling, and mechanical properties including tensile strength of 213 MPa and Young's modulus of ~1.8 MPa/(Δl/l). Structural battery panels developed from this approach were demonstrated as an integrated power delivery platform for a 1U CubeSat frame to augment or replace interior external battery packs. Overall, this approach showed a new path for battery integration into systems where the inactive materials for energy storage are the active composite structural materials.

To build upon the work in chapter 6, chapter 7 examined a key challenge in designing a structurally robust lithium-ion battery composite material; mitigating delamination across interfaces in the absence of continuously applied compressive stress from external packaging media. Here, I shown that for battery active materials coated onto carbon fiber current collectors, a thin electroconductive poly acrylonitrile, or PAN, coating applied to the surface of the fiber/active material current collector drastically improved the performance of a carbon fiber reinforced structural battery material. This lead to structural battery composites composed of lithium iron phosphate and graphite active cathode and anode materials, respectively, which exhibited energy density of 52 Wh/kg relative to combined active and inactive composite materials with capacity retention > 80% for over 100 cycles. Mechanical and electrochemical testing correlated this excellent performance to the role of PAN coating that evenly distributed stress throughout the electrode to prevent early mechanical failure across interfaces. These findings

presented a general approach suitable to adapt energy storage into systems by repurposing the structural elements of the system as the packaging of the active materials.

8.2 Future Outlook

Electrochemical reduction of CO_2 to value-added materials is a novel carbon-negative manufacturing technique to synthesize carbon nanomaterials while decreasing atmospheric CO_2. Aside from mitigating greenhouse gas emissions, this synthesis method opens new doors for liquid-phase synthesis of nanocarbons. There are so many fundamental and applied directions that can be studied. Some essential directions include exploring non catalytic electrolytic CNT growth with the promise to explore CNT cloning and extending CNT growth once initial growth has ceased. In this liquid-phase electrochemical system, carbon is being assembled at an interface, so if this atomistic assembly process could be continued without the use of a catalyst, CNT length could be extended beyond new length scales, even to meters long. CNTs sustainably grown from this electrolytic system can be used in countless other technological applications to offset the carbon footprint of industrial processes such as manufacturing of automotive parts, sporting equipment, coatings, thin-film electronics, and portable electronics to name a few.

Thinking about integration of CNTs into devices and applications, electrophoretic deposition is a favorable synthesis technique to achieve uniform dispersion of CNTs throughout the deposited materials to harness the beneficial CNT properties to their fullest extent. In addition to incorporating CNTs into energy storage devices to augment energy and power density, there are other initiatives that would greatly benefit from controlled EPD of CNTs, such as flexible electronics. This is a relatively new front that has great promise for developing next-generation circuitry and can be extended to depositing other materials such as other carbon allotropes and

metal nanoparticles. The ability to controllably assemble CNTs in a variety of patterns, including circuits, is a huge stepping stone towards flexible and transparent microchips. EPD enables CNTs to be deposited in a seamless pattern on substrates which can then be integrated as circuits in applications beyond just microchips, including everyday objects such as fabrics, wallpaper, and even home décor.

Controllable EPD of nanomaterials could also be used to fabricate battery electrodes to engineer different architectures. This strategy could be used to maximize surface area at interfaces and enhance contact between conductive additives, binders, and active battery material. Improving interfacial behavior can minimize any undesirable side reactions and can also help minimize material delamination to increase cycle life and battery performance. Engineering better interfaces is critical for many systems, not just structural batteries. When thinking about stabilizing structural battery interfaces with polymers, this technique could be extended to other battery chemistries, such as that used to enable a high-rate structural battery. An open framework cathode and co-intercalation anode with a liner ether-based electrolyte could be integrated into a structural battery architecture to increase the power density for applications such as drones, satellites, and even towards electric vehicles. Overall, fundamental CNT synthesis and integration of nanomaterials into energy storage devices enables development of next-generation technologies to provide more capacity on the grid to power society.

REFERENCES

1. Kostiantyn Turcheniuk, D. B., Vinod Singhal & Gleb Yushin, Ten years left to redesign lithium-ion batteries. *Nature* 2018, *559* (7715), 467-470.

2. Armand, M.; Tarascon, J. M., Building better batteries. *Nature* 2008, *451* (7179), 652-657.

3. Lv, W.; Wang, Z.; Cao, H.; Sun, Y.; Zhang, Y.; Sun, Z., A Critical Review and Analysis on the Recycling of Spent Lithium-Ion Batteries. *ACS Sustainable Chemistry & Engineering* 2018, *6* (2), 1504-1521.

4. Zubi, G.; Dufo-López, R.; Carvalho, M.; Pasaoglu, G., The lithium-ion battery: State of the art and future perspectives. *Renewable and Sustainable Energy Reviews* 2018, *89*, 292-308.

5. Li, M.; Lu, J.; Chen, Z.; Amine, K., 30 Years of Lithium-Ion Batteries. *Advanced Materials* 2018, *30* (33), 1800561.

6. Saw, L. H.; Ye, Y.; Tay, A. A. O., Integration issues of lithium-ion battery into electric vehicles battery pack. *Journal of Cleaner Production* 2016, *113*, 1032-1045.

7. Lin, D.; Liu, Y.; Pei, A.; Cui, Y., Nanoscale perspective: Materials designs and understandings in lithium metal anodes. *Nano Research* 2017, *10* (12), 4003-4026.

8. Kwade, A.; Haselrieder, W.; Leithoff, R.; Modlinger, A.; Dietrich, F.; Droeder, K., Current status and challenges for automotive battery production technologies. *Nature Energy* 2018, *3* (4), 290-300.

9. Schmuch, R.; Wagner, R.; Hörpel, G.; Placke, T.; Winter, M., Performance and cost of materials for lithium-based rechargeable automotive batteries. *Nature Energy* 2018, *3* (4), 267-278.

10. Magasinski, A.; Dixon, P.; Hertzberg, B.; Kvit, A.; Ayala, J.; Yushin, G., High-performance lithium-ion anodes using a hierarchical bottom-up approach. *Nature Materials* 2010, *9* (4), 353-358.

11. Manthiram, A.; Yu, X.; Wang, S., Lithium battery chemistries enabled by solid-state electrolytes. *Nature Reviews Materials* 2017, *2* (4), 16103.

12. Few, S.; Schmidt, O.; Offer, G. J.; Brandon, N.; Nelson, J.; Gambhir, A., Prospective improvements in cost and cycle life of off-grid lithium-ion battery packs: An analysis informed by expert elicitations. *Energy Policy* 2018, *114*, 578-590.

13. Ding, X.; Huang, X.; Jin, J.; Ming, H.; Wang, L.; Ming, J., Advanced and safer lithium-ion battery based on sustainable electrodes. *Journal of Power Sources* 2018, *379*, 53-59.

14. Sun, Y.-K.; Lee, D.-J.; Lee, Y. J.; Chen, Z.; Myung, S.-T., Cobalt-Free Nickel Rich Layered Oxide Cathodes for Lithium-Ion Batteries. *ACS Applied Materials & Interfaces* 2013, *5* (21), 11434-11440.

15. Wang, Q.; Liu, W.; Yuan, X.; Tang, H.; Tang, Y.; Wang, M.; Zuo, J.; Song, Z.; Sun, J., Environmental impact analysis and process optimization of batteries based on life cycle assessment. *Journal of Cleaner Production* 2018, *174*, 1262-1273.

16. Liang, Y.; Su, J.; Xi, B.; Yu, Y.; Ji, D.; Sun, Y.; Cui, C.; Zhu, J., Life cycle assessment of lithium-ion batteries for greenhouse gas emissions. *Resources, Conservation and Recycling* 2017, *117*, 285-293.

17. Tarascon, J.-M., Key challenges in future Li-battery research. *Philosophical Transactions of the Royal Society A: Mathematical, Physical and Engineering Sciences* 2010, *368*, 3227-3241.

18. Moyer, K.; Donohue, J.; Ramanna, N.; Cohn, A. P.; Muralidharan, N.; Eaves, J.; Pint, C. L., High-rate potassium ion and sodium ion batteries by co-intercalation anodes and open framework cathodes. *Nanoscale* 2018, *10* (28), 13335-13342.

19. Yuan, C.; Deng, Y.; Li, T.; Yang, F., Manufacturing energy analysis of lithium ion battery pack for electric vehicles. *CIRP Annals* 2017, *66* (1), 53-56.

20. Zheng, X.; Zhu, Z.; Lin, X.; Zhang, Y.; He, Y.; Cao, H.; Sun, Z., A Mini-Review on Metal Recycling from Spent Lithium Ion Batteries. *Engineering* 2018, *4* (3), 361-370.

21. Rao, R.; Pint, C. L.; Islam, A. E.; Weatherup, R. S.; Hofmann, S.; Meshot, E. R.; Wu, F.; Zhou, C.; Dee, N.; Amama, P. B.; Carpena-Nuñez, J.; Shi, W.; Plata, D. L.; Penev, E. S.; Yakobson, B. I.; Balbuena, P. B.; Bichara, C.; Futaba, D. N.; Noda, S.; Shin, H.; Kim, K. S.; Simard, B.; Mirri, F.; Pasquali, M.; Fornasiero, F.; Kauppinen, E. I.; Arnold, M.; Cola, B. A.; Nikolaev, P.; Arepalli, S.; Cheng, H.-M.; Zakharov, D. N.; Stach, E. A.; Zhang, J.; Wei, F.; Terrones, M.; Geohegan, D. B.; Maruyama, B.; Maruyama, S.; Li, Y.; Adams, W. W.; Hart, A. J., Carbon Nanotubes and Related Nanomaterials: Critical Advances and Challenges for Synthesis toward Mainstream Commercial Applications. *ACS Nano* 2018, *12* (12), 11756-11784.

22. Arcaro, S., *Nanomaterials for Eco-friendly Applications*. Springer Nature Switzerland AG: Gewerbestrasse 11, 6330 Cham, Switzerland, 2019.

23. Arcaro, S.; Berutti, F. A.; Alves, A. K.; Bergmann, C. P., MWCNTs produced by electrolysis of molten carbonate: Characteristics of the cathodic products grown on galvanized steel and nickel chrome electrodes. *Applied Surface Science* 2019, *466*, 367-374.

24. Licht, S.; Liu, X.; Licht, G.; Wang, X.; Swesi, A.; Chan, D., Amplified CO2 reduction of greenhouse gas emissions with C2CNT carbon nanotube composites. *Materials Today Sustainability* 2019, 100023.

25. Wu, H.; Li, Z.; Ji, D.; Liu, Y.; Yi, G.; Yuan, D.; Wang, B.; Zhang, Z., Effect of molten carbonate composition on the generation of carbon material. *RSC Advances* 2017, *7* (14), 8467-8473.

26. Ren, J.; Johnson, M.; Singhal, R.; Licht, S., Transformation of the greenhouse gas CO2 by molten electrolysis into a wide controlled selection of carbon nanotubes. *Journal of CO2 Utilization* 2017, *18*, 335-344.

27. Massot, L.; Chamelot, P.; Bouyer, F.; Taxil, P., Studies of carbon nucleation phenomena in molten alkaline fluoride media. *Electrochimica Acta* 2003, *48* (5), 465-471.

28. Ijije, H. V.; Chen, G. Z., Electrochemical manufacturing of nanocarbons from carbon dioxide in molten alkali metal carbonate salts: roles of alkali metal cations. *Advances in Manufacturing* 2016, *4* (1), 23-32.

29. Hughes, M. A.; Allen, J. A.; Donne, S. W., Carbonate Reduction and the Properties and Applications of Carbon Formed Through Electrochemical Deposition in Molten Carbonates: A Review. *Electrochimica Acta* 2015, *176*, 1511-1521.

30. Ye, L.; Zhang, M.; Huang, P.; Guo, G.; Hong, M.; Li, C.; Irvine, J. T. S.; Xie, K., Enhancing CO2 electrolysis through synergistic control of non-stoichiometry and doping to tune cathode surface structures. *Nature Communications* 2017, *8*, 14785.

31. Zhu, G.; Yang, W.; Lv, W.; He, J.; Wen, K.; Huo, W.; Hu, J.; Waqas, M.; Dickerson, J. H.; He, W., Facile electrophoretic deposition of functionalized Bi2O3 nanoparticles. *Materials & Design* 2017, *116*, 359-364.

32. Ye, L.; Wen, K.; Zhang, Z.; Yang, F.; Liang, Y.; Lv, W.; Lin, Y.; Gu, J.; Dickerson, J. H.; He, W., Highly Efficient Materials Assembly Via Electrophoretic Deposition for Electrochemical Energy Conversion and Storage Devices. *Advanced Energy Materials* 2016, *6* (7), 1502018-n/a.

33. Dillon, A. D.; Le Quoc, L.; Goktas, M.; Opasanont, B.; Dastidar, S.; Mengel, S.; Baxter, J. B.; Fafarman, A. T., Thin films of copper indium selenide fabricated with high atom economy by electrophoretic deposition of nanocrystals under flow. *Chemical Engineering Science* 2016, *154*, 128-135.

34. Moyer, K.; Carter, R.; Hanken, T.; Douglas, A.; Oakes, L.; Pint, C. L., Electrophoretic deposition of LiFePO4 onto 3-D current collectors for high areal loading battery cathodes. *Materials Science and Engineering: B* 2019, *241*, 42-47.

35. Moyer, K.; Meng, C.; Marshall, B.; Assal, O.; Eaves, J.; Perez, D.; Karkkainen, R.; Roberson, L.; Pint, C. L., Carbon fiber reinforced structural lithium-ion battery composite: Multifunctional power integration for CubeSats. *Energy Storage Materials* 2019.

36. Douglas, A.; Pint, C. L., Review—Electrochemical Growth of Carbon Nanotubes and Graphene from Ambient Carbon Dioxide: Synergy with Conventional Gas-Phase Growth Mechanisms. *ECS Journal of Solid State Science and Technology* 2017, *6* (6), M3084-M3089.

37. Yin, H.; Mao, X.; Tang, D.; Xiao, W.; Xing, L.; Zhu, H.; Wang, D.; Sadoway, D. R., Capture and electrochemical conversion of CO2 to value-added carbon and oxygen by molten salt electrolysis. *Energy & Environmental Science* 2013, *6* (5), 1538-1545.

38. Kamali, A. R.; Fray, D., Electrochemical interaction between graphite and molten salts to produce nanotubes, nanoparticles, graphene and nanodiamonds. *Journal of Materials Science* 2016, *51* (1), 569-576.

39. Ren, J.; Li, F.-F.; Lau, J.; González-Urbina, L.; Licht, S., One-Pot Synthesis of Carbon Nanofibers from CO2. *Nano Letters* 2015, *15* (9), 6142-6148.

40. Licht, S.; Douglas, A.; Ren, J.; Carter, R.; Lefler, M.; Pint, C. L., Carbon Nanotubes Produced from Ambient Carbon Dioxide for Environmentally Sustainable Lithium-Ion and Sodium-Ion Battery Anodes. *ACS Central Science* 2016, *2* (3), 162-168.

41. Douglas, A.; Carter, R.; Li, M.; Pint, C. L., Toward Small-Diameter Carbon Nanotubes Synthesized from Captured Carbon Dioxide: Critical Role of Catalyst Coarsening. *ACS Applied Materials & Interfaces* 2018, *10* (22), 19010-19018.

42. Douglas, A.; Muralidharan, N.; Carter, R.; Pint, C. L., Sustainable Capture and Conversion of Carbon Dioxide into Valuable Multiwalled Carbon Nanotubes Using Metal Scrap Materials. *ACS Sustainable Chemistry & Engineering* 2017, *5* (8), 7104-7110.

43. Gao, M.; Deng, B.; Chen, Z.; Tao, M.; Wang, D., Cathodic reaction kinetics for CO2 capture and utilization in molten carbonates at mild temperatures. *Electrochemistry Communications* 2018, *88*, 79-82.

44. Gao, M.; Deng, B.; Chen, Z.; Tao, M.; Wang, D., Enhanced kinetics of CO2 electro-reduction on a hollow gas bubbling electrode in molten ternary carbonates. *Electrochemistry Communications* 2019, *100*, 81-84.

45. Ijije, H. V.; Lawrence, R. C.; Chen, G. Z., Carbon electrodeposition in molten salts: electrode reactions and applications. *RSC Advances* 2014, *4* (67), 35808-35817.

46. Ingram, M. D.; Baron, B.; Janz, G. J., The electrolytic deposition of carbon from fused carbonates. *Electrochimica Acta* 1966, *11* (11), 1629-1639.

47. Ijije, H. V.; Lawrence, R. C.; Siambun, N. J.; Jeong, S. M.; Jewell, D. A.; Hu, D.; Chen, G. Z., Electro-deposition and re-oxidation of carbon in carbonate-containing molten salts. *Faraday Discussions* 2014, *172* (0), 105-116.

48. Massot, L.; Chamelot, P.; Bouyer, F.; Taxil, P., Electrodeposition of carbon films from molten alkaline fluoride media. *Electrochimica Acta* 2002, *47* (12), 1949-1957.

49. Du, K.; Yu, R.; Gao, M.; Chen, Z.; Mao, X.; Zhu, H.; Wang, D., Durability of platinum coating anode in molten carbonate electrolysis cell. *Corrosion Science* 2019, *153*, 12-18.

50. Kawamura, H.; Ito, Y., Electrodeposition of cohesive carbon films on aluminum in a LiCl–KCl–K2CO3 melt. *Journal of Applied Electrochemistry* 2000, *30* (5), 571-574.

51. Le Van, K.; Groult, H.; Lantelme, F.; Dubois, M.; Avignant, D.; Tressaud, A.; Komaba, S.; Kumagai, N.; Sigrist, S., Electrochemical formation of carbon nano-powders with various porosities in molten alkali carbonates. *Electrochimica Acta* 2009, *54* (19), 4566-4573.

52. Lorenz, P. K.; Janz, G. J., Electrolysis of molten carbonates: anodic and cathodic gas-evolving reactions. *Electrochimica Acta* 1970, *15* (6), 1025-1035.

53. Ijije, H. V.; Sun, C.; Chen, G. Z., Indirect electrochemical reduction of carbon dioxide to carbon nanopowders in molten alkali carbonates: Process variables and product properties. *Carbon* 2014, *73*, 163-174.

54. Chery, D.; Lair, V.; Cassir, M., Overview on CO2 Valorization: Challenge of Molten Carbonates. *Frontiers in Energy Research* 2015, *3* (43).

55. Kaplan, B.; Groult, H.; Barhoun, A.; Lantelme, F.; Nakajima, T.; Gupta, V.; Komaba, S.; Kumagai, N., Synthesis and Structural Characterization of Carbon Powder by Electrolytic Reduction of Molten Li2 CO 3 - Na2 CO 3 - K 2 CO 3. *Journal of The Electrochemical Society* 2002, *149* (5), D72-D78.

56. Janz, G. J.; Lorenz, M. R., Molten Carbonate Electrolytes: Physical Properties, Structure, and Mechanism of Electrical Conductance. *Journal of The Electrochemical Society* 1961, *108* (11), 1052-1058.

57. WILLIAMS, R. M.; SIMPSON, H. E., A Note on the Effect of Lithium Oxide Upon the Surface Tension of Several Silicate Melts. *Journal of the American Ceramic Society* 1951, *34* (9), 280-283.

58. Y. Ren, N. L., B. Wu, *LiFePO4 Cathode Material*. Shanghai, China, 2011.

59. Wakihara, M., Recent developments in lithium ion batteries. *Materials Science and Engineering: R: Reports* 2001, *33* (4), 109-134.

60. Yuan, L.-X.; Wang, Z.-H.; Zhang, W.-X.; Hu, X.-L.; Chen, J.-T.; Huang, Y.-H.; Goodenough, J. B., Development and challenges of LiFePO4 cathode material for lithium-ion batteries. *Energy & Environmental Science* 2011, *4* (2), 269-284.

61. Wu, X.-L.; Jiang, L.-Y.; Cao, F.-F.; Guo, Y.-G.; Wan, L.-J., LiFePO4 Nanoparticles Embedded in a Nanoporous Carbon Matrix: Superior Cathode Material for Electrochemical Energy-Storage Devices. *Advanced Materials* 2009, *21* (25-26), 2710-2714.

62. Han, X.; Ouyang, M.; Lu, L.; Li, J.; Zheng, Y.; Li, Z., A comparative study of commercial lithium ion battery cycle life in electrical vehicle: Aging mechanism identification. *Journal of Power Sources* 2014, *251*, 38-54.

63. Zhang, Y.; Li, Y.; Xia, X.; Wang, X.; Gu, C.; Tu, J., High-energy cathode materials for Li-ion batteries: A review of recent developments. *Science China Technological Sciences* 2015, *58* (11), 1809-1828.

64. Li, J.; Armstrong, B. L.; Kiggans, J.; Daniel, C.; Wood, D. L., Optimization of LiFePO4 Nanoparticle Suspensions with Polyethyleneimine for Aqueous Processing. *Langmuir* 2012, *28* (8), 3783-3790.

65. Ciez, R. E.; Whitacre, J. F., Comparison between cylindrical and prismatic lithium-ion cell costs using a process based cost model. *Journal of Power Sources* 2017, *340*, 273-281.

66. K. W. Celina Mikolajczak, M. K., Richard Thomas Long, *Lithium-Ion Batteries Hazard and Use Assessment*. Springer: Verlag, New York 2011.

67. Zhang, H.; Yu, X.; Braun, P. V., Three-dimensional bicontinuous ultrafast-charge and -discharge bulk battery electrodes. *Nat Nano* 2011, *6* (5), 277-281.

68. Yao, M.; Okuno, K.; Iwaki, T.; Awazu, T.; Sakai, T., Long cycle-life LiFePO4/Cu-Sn lithium ion battery using foam-type three-dimensional current collector. *Journal of Power Sources* 2010, *195* (7), 2077-2081.

69. Lim, S.; Yoon, C. S.; Cho, J., Synthesis of Nanowire and Hollow LiFePO4 Cathodes for High-Performance Lithium Batteries. *Chemistry of Materials* 2008, *20* (14), 4560-4564.

70. Li, X.; Kang, F.; Bai, X.; Shen, W., A novel network composite cathode of LiFePO4/multiwalled carbon nanotubes with high rate capability for lithium ion batteries. *Electrochemistry Communications* 2007, *9* (4), 663-666.

71. Jiang, J.; Li, Y.; Liu, J.; Huang, X.; Yuan, C.; Lou, X. W., Recent Advances in Metal Oxide-based Electrode Architecture Design for Electrochemical Energy Storage. *Advanced Materials* 2012, *24* (38), 5166-5180.

72. Ender, M.; Joos, J.; Carraro, T.; Ivers-Tiffée, E., Three-dimensional reconstruction of a composite cathode for lithium-ion cells. *Electrochemistry Communications* 2011, *13* (2), 166-168.

73. Chen, R.; Zhao, T.; Zhang, X.; Li, L.; Wu, F., Advanced cathode materials for lithium-ion batteries using nanoarchitectonics. *Nanoscale Horizons* 2016, *1* (6), 423-444.

74. Hagen, M.; Hanselmann, D.; Ahlbrecht, K.; Maça, R.; Gerber, D.; Tübke, J., Lithium–Sulfur Cells: The Gap between the State-of-the-Art and the Requirements for High Energy Battery Cells. *Advanced Energy Materials* 2015, *5* (16), 1401986-n/a.

75. Roberts, M.; Johns, P.; Owen, J.; Brandell, D.; Edstrom, K.; El Enany, G.; Guery, C.; Golodnitsky, D.; Lacey, M.; Lecoeur, C.; Mazor, H.; Peled, E.; Perre, E.; Shaijumon, M. M.; Simon, P.; Taberna, P.-L., 3D lithium ion batteries-from fundamentals to fabrication. *Journal of Materials Chemistry* 2011, *21* (27), 9876-9890.

76. Gowda, S. R.; Leela Mohana Reddy, A.; Zhan, X.; Jafry, H. R.; Ajayan, P. M., 3D Nanoporous Nanowire Current Collectors for Thin Film Microbatteries. *Nano Letters* 2012, *12* (3), 1198-1202.

77. Arthur, T. S.; Bates, D. J.; Cirigliano, N.; Johnson, D. C.; Malati, P.; Mosby, J. M.; Perre, E.; Rawls, M. T.; Prieto, A. L.; Dunn, B., Three-dimensional electrodes and battery architectures. *MRS Bulletin* 2011, *36* (7), 523-531.

78. Self, E. C.; Wycisk, R.; Pintauro, P. N., Electrospun titania-based fibers for high areal capacity Li-ion battery anodes. *Journal of Power Sources* 2015, *282*, 187-193.

79. Self, E. C.; Naguib, M.; Ruther, R. E.; McRen, E. C.; Wycisk, R.; Liu, G.; Nanda, J.; Pintauro, P. N., High Areal Capacity Si/LiCoO2 Batteries from Electrospun Composite Fiber Mats. *ChemSusChem* 2017, *10* (8), 1823-1831.

80. Self, E. C.; McRen, E. C.; Wycisk, R.; Pintauro, P. N., LiCoO2-Based Fiber Cathodes for Electrospun Full Cell Li-ion Batteries. *Electrochimica Acta* 2016, *214*, 139-146.

81. Mazor, H.; Golodnitsky, D.; Burstein, L.; Gladkich, A.; Peled, E., Electrophoretic deposition of lithium iron phosphate cathode for thin-film 3D-microbatteries. *Journal of Power Sources* 2012, *198*, 264-272.

82. Corni, I.; Ryan, M. P.; Boccaccini, A. R., Electrophoretic deposition: From traditional ceramics to nanotechnology. *Journal of the European Ceramic Society* 2008, *28* (7), 1353-1367.

83. Collini, P.; Kota, S.; Dillon, A. D.; Barsoum, M. W.; Fafarman, A. T., Electrophoretic Deposition of Two-Dimensional Titanium Carbide (MXene) Thick Films. *Journal of The Electrochemical Society* 2017, *164* (9), D573-D580.

84. Oakes, L.; Zulkifli, D.; Azmi, H.; Share, K.; Hanken, T.; Carter, R.; Pint, C. L., One Batch Exfoliation and Assembly of Two-Dimensional Transition Metal Dichalcogenide Nanosheets Using Electrophoretic Deposition. *Journal of The Electrochemical Society* 2015, *162* (11), D3063-D3070.

85. Oakes, L.; Hanken, T.; Carter, R.; Yates, W.; Pint, C. L., Roll-to-Roll Nanomanufacturing of Hybrid Nanostructures for Energy Storage Device Design. *ACS Applied Materials & Interfaces* 2015, *7* (26), 14201-14210.

86. Oakes, L.; Cohn, A. P.; Westover, A. S.; Pint, C. L., Electrophoretic stabilization of freestanding pristine graphene foams with carbon nanotubes for enhanced optical and electrical response. *Materials Letters* 2015, *159*, 261-264.

87. Oakes, L.; Carter, R.; Pint, C. L., Nanoscale defect engineering of lithium-sulfur battery composite cathodes for improved performance. *Nanoscale* 2016, *8* (46), 19368-19375.

88. Oakes, L.; Carter, R.; Hanken, T.; Cohn, A. P.; Share, K.; Schmidt, B.; Pint, C. L., Interface strain in vertically stacked two-dimensional heterostructured carbon-MoS2 nanosheets controls electrochemical reactivity. 2016, *7*, 11796.

89. Landon, O.; Nitin, M.; Adam, P. C.; Cary, L. P., Catalyst morphology matters for lithium–oxygen battery cathodes. *Nanotechnology* 2016, *27* (49), 495404.

90. Liu, Y.; Qiao, Y.; Zhang, W.; Li, Z.; Ji, X.; Miao, L.; Yuan, L.; Hu, X.; Huang, Y., Sodium storage in Na-rich NaxFeFe(CN)6 nanocubes. *Nano Energy* 2015, *12* (Supplement C), 386-393.

91. Gallagher, K. G.; Trask, S. E.; Bauer, C.; Woehrle, T.; Lux, S. F.; Tschech, M.; Lamp, P.; Polzin, B. J.; Ha, S.; Long, B.; Wu, Q.; Lu, W.; Dees, D. W.; Jansen, A. N., Optimizing Areal Capacities through Understanding the Limitations of Lithium-Ion Electrodes. *Journal of The Electrochemical Society* 2016, *163* (2), A138-A149.

92. Ahmed, S.; Nelson, P. A.; Gallagher, K. G.; Susarla, N.; Dees, D. W., Cost and energy demand of producing nickel manganese cobalt cathode material for lithium ion batteries. *Journal of Power Sources* 2017, *342*, 733-740.

93. Endo, M.; Kim, C.; Nishimura, K.; Fujino, T.; Miyashita, K., Recent development of carbon materials for Li ion batteries. *Carbon* 2000, *38* (2), 183-197.

94. Shin, H. C.; Cho, W. I.; Jang, H., Electrochemical properties of carbon-coated LiFePO4 cathode using graphite, carbon black, and acetylene black. *Electrochimica Acta* 2006, *52* (4), 1472-1476.

95. Li, J.; Rulison, C.; Kiggans, J.; Daniel, C.; Wood, D. L., Superior Performance of LiFePO4 Aqueous Dispersions via Corona Treatment and Surface Energy Optimization. *Journal of The Electrochemical Society* 2012, *159* (8), A1152-A1157.

96. Li, J.; Armstrong, B. L.; Kiggans, J.; Daniel, C.; Wood, D. L., Lithium Ion Cell Performance Enhancement Using Aqueous LiFePO4 Cathode Dispersions and Polyethyleneimine Dispersant. *Journal of The Electrochemical Society* 2013, *160* (2), A201-A206.

97. Li, J.; Armstrong, B. L.; Daniel, C.; Kiggans, J.; Wood, D. L., Optimization of multicomponent aqueous suspensions of lithium iron phosphate (LiFePO4) nanoparticles and carbon black for lithium-ion battery cathodes. *Journal of Colloid and Interface Science* 2013, *405*, 118-124.

98. Swiderska-Mocek, A.; Rudnicka, E., Lithium–sulphur battery with activated carbon cloth-sulphur cathode and ionic liquid as electrolyte. *Journal of Power Sources* 2015, *273*, 162-167.

99. Liu, B.; Zhang, J.; Wang, X.; Chen, G.; Chen, D.; Zhou, C.; Shen, G., Hierarchical Three-Dimensional ZnCo2O4 Nanowire Arrays/Carbon Cloth Anodes for a Novel Class of High-Performance Flexible Lithium-Ion Batteries. *Nano Letters* 2012, *12* (6), 3005-3011.

100. Wood Iii, D. L.; Li, J.; Daniel, C., Prospects for reducing the processing cost of lithium ion batteries. *Journal of Power Sources* 2015, *275*, 234-242.

101. Larcher, D.; Tarascon, J. M., Towards greener and more sustainable batteries for electrical energy storage. *Nat Chem* 2015, *7* (1), 19-29.

102. Turcheniuk, K.; Bondarev, D.; Singhal, V.; Yushin, G., Ten years left to redesign lithium-ion batteries. *Nature* 2018, *559*, 467-470.

103. Li, J.; Daniel, C.; Wood, D., Materials processing for lithium-ion batteries. *Journal of Power Sources* 2011, *196* (5), 2452-2460.

104. Moshtev, R.; Johnson, B., State of the art of commercial Li ion batteries. *Journal of Power Sources* 2000, *91* (2), 86-91.

105. Wang, J. S.; Liu, P.; Sherman, E.; Verbrugge, M.; Tataria, H., Formulation and characterization of ultra-thick electrodes for high energy lithium-ion batteries employing tailored metal foams. *Journal of Power Sources* 2011, *196* (20), 8714-8718.

106. Grimsmann, F.; Brauchle, F.; Gerbert, T.; Gruhle, A.; Knipper, M.; Parisi, J., Hysteresis and current dependence of the thickness change of lithium-ion cells with graphite anode. *Journal of Energy Storage* 2017, *12*, 132-137.

107. Robinson, J. P.; Ruppert, J. J.; Dong, H.; Koenig, G. M., Sintered electrode full cells for high energy density lithium-ion batteries. *Journal of Applied Electrochemistry* 2018, *48* (11), 1297-1304.

108. Zheng, H.; Li, J.; Song, X.; Liu, G.; Battaglia, V. S., A comprehensive understanding of electrode thickness effects on the electrochemical performances of Li-ion battery cathodes. *Electrochimica Acta* 2012, *71*, 258-265.

109. Elango, R.; Demortière, A.; Andrade, V.; Morcrette, M.; Seznec, V., Thick Binder-Free Electrodes for Li–Ion Battery Fabricated Using Templating Approach and Spark Plasma Sintering Reveals High Areal Capacity. *Advanced Energy Materials* 2018, *8* (15), 1703031.

110. Hawley, W. B.; Li, J., Electrode manufacturing for lithium-ion batteries—Analysis of current and next generation processing. *Journal of Energy Storage* 2019, *25*, 100862.

111. Patry, G.; Romagny, A.; Martinet, S.; Froelich, D., Cost modeling of lithium-ion battery cells for automotive applications. *Energy Science & Engineering* 2015, *3* (1), 71-82.

112. Sotomayor, M. E.; Torre-Gamarra, C. d. l.; Levenfeld, B.; Sanchez, J.-Y.; Varez, A.; Kim, G.-T.; Varzi, A.; Passerini, S., Ultra-thick battery electrodes for high gravimetric and volumetric energy density Li-ion batteries. *Journal of Power Sources* 2019, *437*, 226923.

113. Singh, M.; Kaiser, J.; Hahn, H., Thick Electrodes for High Energy Lithium Ion Batteries. *Journal of The Electrochemical Society* 2015, *162* (7), A1196-A1201.

114. Evanoff, K.; Khan, J.; Balandin, A. A.; Magasinski, A.; Ready, W. J.; Fuller, T. F.; Yushin, G., Towards Ultrathick Battery Electrodes: Aligned Carbon Nanotube – Enabled Architecture. *Advanced Materials* 2012, *24* (4), 533-537.

115. Hu, L.; La Mantia, F.; Wu, H.; Xie, X.; McDonough, J.; Pasta, M.; Cui, Y., Lithium-Ion Textile Batteries with Large Areal Mass Loading. *Advanced Energy Materials* 2011, *1* (6), 1012-1017.

116. Li, J.; Du, Z.; Ruther, R. E.; AN, S. J.; David, L. A.; Hays, K.; Wood, M.; Phillip, N. D.; Sheng, Y.; Mao, C.; Kalnaus, S.; Daniel, C.; Wood, D. L., Toward Low-Cost, High-Energy Density, and High-Power Density Lithium-Ion Batteries. *JOM* 2017, *69* (9), 1484-1496.

117. Sun, C.; Liu, S.; Shi, X.; Lai, C.; Liang, J.; Chen, Y., 3D printing nanocomposite gel-based thick electrode enabling both high areal capacity and rate performance for lithium-ion battery. *Chemical Engineering Journal* 2020, *381*, 122641.

118. Cheng, H.-M.; Li, F., Charge delivery goes the distance. *Science* 2017, *356* (6338), 582-583.

119. Du, Z.; Rollag, K. M.; Li, J.; An, S. J.; Wood, M.; Sheng, Y.; Mukherjee, P. P.; Daniel, C.; Wood Iii, D. L., Enabling aqueous processing for crack-free thick electrodes. *Journal of Power Sources* 2017, *354*, 200-206.

120. Kuang, Y.; Chen, C.; Kirsch, D.; Hu, L., Thick Electrode Batteries: Principles, Opportunities, and Challenges. *Advanced Energy Materials* 2019, *9* (33), 1901457.

121. Kanamura, K.; Goto, A.; Hamagami, J. i.; Umegaki, T., Electrophoretic Fabrication of Positive Electrodes for Rechargeable Lithium Batteries. *Electrochemical and Solid-State Letters* 2000, *3* (6), 259-262.

122. Boccaccini, A. R.; Cho, J.; Subhani, T.; Kaya, C.; Kaya, F., Electrophoretic deposition of carbon nanotube–ceramic nanocomposites. *Journal of the European Ceramic Society* 2010, *30* (5), 1115-1129.

123. Cohn, A. P.; Oakes, L.; Carter, R.; Chatterjee, S.; Westover, A. S.; Share, K.; Pint, C. L., Assessing the improved performance of freestanding, flexible graphene and carbon nanotube hybrid foams for lithium ion battery anodes. *Nanoscale* 2014, *6* (9), 4669-4675.

124. Carter, R.; Oakes, L.; Cohn, A. P.; Holzgrafe, J.; Zarick, H. F.; Chatterjee, S.; Bardhan, R.; Pint, C. L., Solution Assembled Single-Walled Carbon Nanotube Foams: Superior Performance in Supercapacitors, Lithium-Ion, and Lithium–Air Batteries. *The Journal of Physical Chemistry C* 2014, *118* (35), 20137-20151.

125. Hasan, S. A.; Kavich, D. W.; Dickerson, J. H., Sacrificial layer electrophoretic deposition of free-standing multilayered nanoparticle films. *Chemical Communications* 2009, (25), 3723-3725.

126. Ferrari, B.; Moreno, R.; Hernán, L.; Melero, M.; Morales, J.; Caballero, A., EPD of thick films for their application in lithium batteries. *Journal of the European Ceramic Society* 2007, *27* (13), 3823-3827.

127. Caballero, A.; Hernán, L.; Melero, M.; Morales, J.; Moreno, R.; Ferrari, B., LiNi0.5Mn1.5O4 thick-film electrodes prepared by electrophoretic deposition for use in high voltage lithium-ion batteries. *Journal of Power Sources* 2006, *158* (1), 583-590.

128. Mazurenko, I.; Etienne, M.; Tananaiko, O.; Urbanova, V.; Zaitsev, V.; Walcarius, A., Electrophoretic deposition of macroporous carbon nanotube assemblies for electrochemical applications. *Carbon* 2013, *53*, 302-312.

129. Du, C.; Heldbrant, D.; Pan, N., Preparation and preliminary property study of carbon nanotubes films by electrophoretic deposition. *Materials Letters* 2002, *57* (2), 434-438.

130. Wood, D. L.; Li, J.; Daniel, C., Prospects for reducing the processing cost of lithium ion batteries. *Journal of Power Sources* 2015, *275*, 234-242.

131. Wu, X.; Xia, S.; Huang, Y.; Hu, X.; Yuan, B.; Chen, S.; Yu, Y.; Liu, W., High-Performance, Low-Cost, and Dense-Structure Electrodes with High Mass Loading for Lithium-Ion Batteries. *Advanced Functional Materials* 2019, *29* (34), 1903961.

132. Seo, S.-D.; Hwang, I.-S.; Lee, S.-H.; Shim, H.-W.; Kim, D.-W., 1D/2D carbon nanotube/graphene nanosheet composite anodes fabricated using electrophoretic assembly. *Ceramics International* 2012, *38* (4), 3017-3021.

133. Padhi, A. K.; Nanjundaswamy, K. S.; Goodenough, J. B., Phospho-olivines as Positive-Electrode Materials for Rechargeable Lithium Batteries. *Journal of The Electrochemical Society* 1997, *144* (4), 1188-1194.

134. Yu, D. Y. W.; Donoue, K.; Inoue, T.; Fujimoto, M.; Fujitani, S., Effect of Electrode Parameters on LiFePO4 Cathodes. *Journal of The Electrochemical Society* 2006, *153* (5), A835-A839.

135. Mahajan, S. V.; Hasan, S. A.; Cho, J.; Shaffer, M. S. P.; Boccaccini, A. R.; Dickerson, J. H., Carbon nanotube–nanocrystal heterostructures fabricated by electrophoretic deposition. *Nanotechnology* 2008, *19* (19), 195301.

136. Boccaccini, A. R.; Cho, J.; Roether, J. A.; Thomas, B. J. C.; Jane Minay, E.; Shaffer, M. S. P., Electrophoretic deposition of carbon nanotubes. *Carbon* 2006, *44* (15), 3149-3160.

137. Du, Z.; Li, J.; Wood, M.; Mao, C.; Daniel, C.; Wood, D. L., Three-dimensional conductive network formed by carbon nanotubes in aqueous processed NMC electrode. *Electrochimica Acta* 2018, *270*, 54-61.

138. Bergin, S. D.; Nicolosi, V.; Streich, P. V.; Giordani, S.; Sun, Z.; Windle, A. H.; Ryan, P.; Niraj, N. P. P.; Wang, Z.-T. T.; Carpenter, L.; Blau, W. J.; Boland, J. J.; Hamilton, J. P.; Coleman, J. N., Towards Solutions of Single-Walled Carbon Nanotubes in Common Solvents. *Advanced Materials* 2008, *20* (10), 1876-1881.

139. Huang, Y.; Liu, H.; Lu, Y.-C.; Hou, Y.; Li, Q., Electrophoretic lithium iron phosphate/reduced graphene oxide composite for lithium ion battery cathode application. *Journal of Power Sources* 2015, *284*, 236-244.

140. Kanamura, K.; Goto, A.; Rho, Y. H.; Umegaki, T., Electrophoretic fabrication of LiCoO2 positive electrodes for rechargeable lithium batteries. *Journal of Power Sources* 2001, *97*, 294-297.

141. Yang, Y.; Chen, D.; Liu, B.; Zhao, J., Binder-Free Si Nanoparticle Electrode with 3D Porous Structure Prepared by Electrophoretic Deposition for Lithium-Ion Batteries. *ACS Applied Materials & Interfaces* 2015, *7* (14), 7497-7504.

142. McCloskey, B. D., Attainable Gravimetric and Volumetric Energy Density of Li–S and Li Ion Battery Cells with Solid Separator-Protected Li Metal Anodes. *The Journal of Physical Chemistry Letters* 2015, *6* (22), 4581-4588.

143. Hagen, M.; Hanselmann, D.; Ahlbrecht, K.; Maça, R.; Gerber, D.; Tübke, J., Lithium–Sulfur Cells: The Gap between the State-of-the-Art and the Requirements for High Energy Battery Cells. *Advanced Energy Materials* 2015, *5* (16), 1401986.

144. Yu, S.; Kim, S.; Kim, T.; Nam, J. H.; Cho, W., Model Prediction and Experiments for the Electrode Design Optimization of LiFePO4/Graphite Electrodes in High Capacity Lithium-ion Batteries. *Bull. Korean Chem. Soc.* 2013, *34*, 79-88.

145. Gao, H.; Wu, Q.; Hu, Y.; Zheng, J. P.; Amine, K.; Chen, Z., Revealing the Rate-Limiting Li-Ion Diffusion Pathway in Ultrathick Electrodes for Li-Ion Batteries. *The Journal of Physical Chemistry Letters* 2018, 5100-5104.

146. Singh, M.; Kaiser, J.; Hahn, H., Effect of Porosity on the Thick Electrodes for High Energy Density Lithium Ion Batteries for Stationary Applications. *Batteries* 2016, *2* (4), 35.

147. Cho, S.-J.; Choi, K.-H.; Yoo, J.-T.; Kim, J.-H.; Lee, Y.-H.; Chun, S.-J.; Park, S.-B.; Choi, D.-H.; Wu, Q.; Lee, S.-Y.; Lee, S.-Y., Hetero-Nanonet Rechargeable Paper Batteries: Toward Ultrahigh Energy Density and Origami Foldability. *Advanced Functional Materials* 2015, *25* (38), 6029-6040.

148. Chen, X.; Zhu, H.; Chen, Y.-C.; Shang, Y.; Cao, A.; Hu, L.; Rubloff, G. W., MWCNT/V2O5 Core/Shell Sponge for High Areal Capacity and Power Density Li-Ion Cathodes. *ACS Nano* 2012, *6* (9), 7948-7955.

149. Chen, C.; Zhang, Y.; Li, Y.; Kuang, Y.; Song, J.; Luo, W.; Wang, Y.; Yao, Y.; Pastel, G.; Xie, J.; Hu, L., Highly Conductive, Lightweight, Low-Tortuosity Carbon Frameworks as Ultrathick 3D Current Collectors. *Advanced Energy Materials* 2017, *7* (17), 1700595.

150. Li, H.; Zhu, Y.; Dong, S.; Shen, L.; Chen, Z.; Zhang, X.; Yu, G., Self-Assembled Nb2O5 Nanosheets for High Energy–High Power Sodium Ion Capacitors. *Chemistry of Materials* 2016, *28* (16), 5753-5760.

151. Lang, J.; Zhang, X.; Liu, B.; Wang, R.; Chen, J.; Yan, X., The roles of graphene in advanced Li-ion hybrid supercapacitors. *Journal of Energy Chemistry* 2018, *27* (1), 43-56.

152. Kang, B.; Ceder, G., Battery materials for ultrafast charging and discharging. *Nature* 2009, *458*, 190-193.

153. Ding, Y.; Yang, B.; Chen, J.; Zhang, L.; Li, J.; Li, Y.; Yan, X., Nanotube-like hard carbon as high-performance anode material for sodium ion hybrid capacitors. *Science China Materials* 2017.

154. Feng, J.; Chernova, N. A.; Omenya, F.; Tong, L.; Rastogi, A. C.; Stanley Whittingham, M., Effect of electrode charge balance on the energy storage performance of hybrid supercapacitor cells based on LiFePO4 as Li-ion battery electrode and activated carbon. *Journal of Solid State Electrochemistry* 2017, 1-16.

155. Le Comte, A.; Reynier, Y.; Vincens, C.; Leys, C.; Azaïs, P., First prototypes of hybrid potassium-ion capacitor (KIC): An innovative, cost-effective energy storage technology for transportation applications. *Journal of Power Sources* 2017, *363* (Supplement C), 34-43.

156. Kouchachvili, L.; Yaïci, W.; Entchev, E., Hybrid battery/supercapacitor energy storage system for the electric vehicles. *Journal of Power Sources* 2018, *374* (Supplement C), 237-248.

157. Cao, W.; Li, Y.; Fitch, B.; Shih, J.; Doung, T.; Zheng, J., Strategies to optimize lithium-ion supercapacitors achieving high-performance: Cathode configurations, lithium loadings on anode, and types of separator. *Journal of Power Sources* 2014, *268*, 841-847.

158. Boltersdorf, J.; Delp, S. A.; Yan, J.; Cao, B.; Zheng, J. P.; Jow, T. R.; Read, J. A., Electrochemical performance of lithium-ion capacitors evaluated under high temperature and high voltage stress using redox stable electrolytes and additives. *Journal of Power Sources* 2018, *373*, 20-30.

159. Béguin, F.; Presser, V.; Balducci, A.; Frackowiak, E., Carbons and Electrolytes for Advanced Supercapacitors. *Advanced Materials* 2014, *26* (14), 2219-2251.

160. Zhang, L. L.; Zhao, X. S., Carbon-based materials as supercapacitor electrodes. *Chemical Society Reviews* 2009, *38* (9), 2520-2531.

161. Sun, X.; Zhang, X.; Zhang, H.; Zhang, D.; Ma, Y., A comparative study of activated carbon-based symmetric supercapacitors in Li2SO4 and KOH aqueous electrolytes. *J Solid State Electrochem* 2012, *16*, 2597-2603.

162. Stoller, M. D.; Ruoff, R. S., Best practice methods for determining an electrode material's performance for ultracapacitors. *Energy Environ Sci* 2010, *3*, 1294-1301.

163. Ruiz, V.; Blanco, C.; Granda, M.; Menéndez, R.; Santamaría, R., Influence of electrode preparation on the electrochemical behaviour of carbon-based supercapacitors. *J Applied Electrochem* 2007, *37*, 717-721.

164. Raymundo-Pinero, E.; Kierzek, K.; Machnikowski, J.; Beguin, F., Relationship between the nanoporous texture of activated carbons and their capacitance properties in different electrolytes. *Carbon* 2006, *44*, 2498-2507.

165. Gao, Q.; Demarconnay, L.; Raymundo-Pinero, E.; Beguin, F., Exploring the large voltage range of carbon/carbon supercapacitors in aqueous lithium sulfate electrolyte. *Energy Environ Sci* 2012, *5*, 9611-9617.

166. Calvo, E. G.; Lufrano, F.; Staiti, P.; Brigandì, A.; Arenillas, A.; Menéndez, J. A., Optimizing the electrochemical performance of aqueous symmetric supercapacitors based on an activated carbon xerogel. *J Power Sources* 2013, *241*, 776-782.

167. Blomquist, N.; Wells, T.; Andres, B.; Bäckström, J.; Forsberg, S.; Olin, H., Metal-free supercapacitor with aqueous electrolyte and low-cost carbon materials. *Scientific Reports* 2017, *7*, 39836.

168. Hwang, J. Y.; El-Kady, M. F.; Li, M.; Lin, C.-W.; Kowal, M.; Han, X.; Kaner, R. B., Boosting the capacitance and voltage of aqueous supercapacitors via redox charge contribution from both electrode and electrolyte. *Nano Today* 2017, *15*, 15-25.

169. Pramudita, J. C.; Sehrawat, D.; Goonetilleke, D.; Sharma, N., An Initial Review of the Status of Electrode Materials for Potassium-Ion Batteries. *Advanced Energy Materials*, 1602911.

170. Lu, P.; Sun, Y.; Xiang, H.; Liang, X.; Yu, Y., 3D Amorphous Carbon with Controlled Porous and Disordered Structures as a High-Rate Anode Material for Sodium-Ion Batteries. *Advanced Energy Materials*, 1702434

171. Zhu, Z.; Cheng, F.; Hu, Z.; Niu, Z.; Chen, J., Highly stable and ultrafast electrode reaction of graphite for sodium ion batteries. *Journal of Power Sources* 2015, *293* (Supplement C), 626-634.

172. Jache, B.; Binder, J. O.; Abe, T.; Adelhelm, P., A comparative study on the impact of different glymes and their derivatives as electrolyte solvents for graphite co-intercalation electrodes in lithium-ion and sodium-ion batteries. *Physical Chemistry Chemical Physics* 2016, *18* (21), 14299-14316.

173. Han, P.; Han, X.; Yao, J.; Zhang, L.; Cao, X.; Huang, C.; Cui, G., High energy density sodium-ion capacitors through co-intercalation mechanism in diglyme-based electrolyte system. *Journal of Power Sources* 2015, *297* (Supplement C), 457-463.

174. Kajita, T.; Itoh, T., Mixed ether-based solvents provide a long cycle life with high rate capability to graphite anodes for Na-ion batteries. *Physical Chemistry Chemical Physics* 2018, 2188-2195.

175. Kim, H.; Hong, J.; Yoon, G.; Kim, H.; Park, K.-Y.; Park, M.-S.; Yoon, W.-S.; Kang, K., Sodium intercalation chemistry in graphite. *Energy & Environmental Science* 2015, *8* (10), 2963-2969.

176. Kim, H.; Yoon, G.; Lim, K.; Kang, K., A comparative study of graphite electrodes using the co-intercalation phenomenon for rechargeable Li, Na and K batteries. *Chemical Communications* 2016, *52* (85), 12618-12621.

177. Kim, H.; Lim, K.; Yoon, G.; Park, J.-H.; Ku, K.; Lim, H.-D.; Sung, Y.-E.; Kang, K., Exploiting Lithium–Ether Co-Intercalation in Graphite for High-Power Lithium-Ion Batteries. *Advanced Energy Materials* 2017, *7* (19), 1700418.

178. Wang, L.; Zou, J.; Chen, S.; Zhou, G.; Bai, J.; Gao, P.; Wang, Y.; Yu, X.; Li, J.; Hu, Y.-S.; Li, H., TiS2 as a high performance potassium ion battery cathode in ether-based electrolyte. *Energy Storage Materials* 2018, *12*, 216-222.

179. Hu, M.; Zhou, H.; Gan, X.; Yang, L.; Huang, Z.-H.; Wang, D.-W.; Kang, F.; Lv, R., Ultrahigh rate sodium ion storage with nitrogen-doped expanded graphite oxide in ether-based electrolyte. *Journal of Materials Chemistry A* 2018, *6* (4), 1582-1589.

180. Moon, H.; Tatara, R.; Mandai, T.; Ueno, K.; Yoshida, K.; Tachikawa, N.; Yasuda, T.; Dokko, K.; Watanabe, M., Mechanism of Li Ion Desolvation at the Interface of Graphite Electrode and Glyme–Li Salt Solvate Ionic Liquids. *The Journal of Physical Chemistry C* 2014, *118* (35), 20246-20256.

181. Maibach, J.; Jeschull, F.; Brandell, D.; Edström, K.; Valvo, M., Surface Layer Evolution on Graphite During Electrochemical Sodium-tetraglyme Co-intercalation. *ACS Applied Materials & Interfaces* 2017, *9* (14), 12373-12381.

182. Cohn, A. P.; Share, K.; Carter, R.; Oakes, L.; Pint, C. L., Ultrafast Solvent-Assisted Sodium Ion Intercalation into Highly Crystalline Few-Layered Graphene. *Nano Letters* 2016, *16* (1), 543-548.

183. Cohn, A. P.; Muralidharan, N.; Carter, R.; Share, K.; Oakes, L.; Pint, C. L., Durable potassium ion battery electrodes from high-rate cointercalation into graphitic carbons. *Journal of Materials Chemistry A* 2016, *4* (39), 14954-14959.

184. Tang, Y.; Zhang, W.; Xue, L.; Ding, X.; Wang, T.; Liu, X.; Liu, J.; Li, X.; Huang, Y., Polypyrrole-promoted superior cyclability and rate capability of NaxFe[Fe(CN)6] cathodes for sodium-ion batteries. *Journal of Materials Chemistry A* 2016, *4* (16), 6036-6041.

185. Wang, L.; Song, J.; Qiao, R.; Wray, L. A.; Hossain, M. A.; Chuang, Y.-D.; Yang, W.; Lu, Y.; Evans, D.; Lee, J.-J.; Vail, S.; Zhao, X.; Nishijima, M.; Kakimoto, S.; Goodenough, J. B., Rhombohedral Prussian White as Cathode for Rechargeable Sodium-Ion Batteries. *Journal of the American Chemical Society* 2015, *137* (7), 2548-2554.

186. You, Y.; Wu, X.-L.; Yin, Y.-X.; Guo, Y.-G., High-quality Prussian blue crystals as superior cathode materials for room-temperature sodium-ion batteries. *Energy & Environmental Science* 2014, *7* (5), 1643-1647.

187. Piernas-Muñoz, M. J.; Castillo-Martínez, E.; Bondarchuk, O.; Armand, M.; Rojo, T., Higher voltage plateau cubic Prussian White for Na-ion batteries. *Journal of Power Sources* 2016, *324* (Supplement C), 766-773.

188. Qiu, X.; Liu, Y.; Wang, L.; Fan, L.-Z., Reverse microemulsion synthesis of nickel-cobalt hexacyanoferrate/reduced graphene oxide nanocomposites for high-performance supercapacitors and sodium ion batteries. *Applied Surface Science* 2018, *434*, 1285-1292.

189. You, Y.; Yu, X.; Yin, Y.; Nam, K.-W.; Guo, Y.-G., Sodium iron hexacyanoferrate with high Na content as a Na-rich cathode material for Na-ion batteries. *Nano Research* 2015, *8* (1), 117-128.

190. Jiang, Y.; Yu, S.; Wang, B.; Li, Y.; Sun, W.; Lu, Y.; Yan, M.; Song, B.; Dou, S., Prussian Blue@C Composite as an Ultrahigh-Rate and Long-Life Sodium-Ion Battery Cathode. *Advanced Functional Materials* 2016, *26* (29), 5315-5321.

191. Zhang, C.; Xu, Y.; Zhou, M.; Liang, L.; Dong, H.; Wu, M.; Yang, Y.; Lei, Y., Potassium Prussian Blue Nanoparticles: A Low-Cost Cathode Material for Potassium-Ion Batteries. *Advanced Functional Materials* 2017, *27* (4), 1604307.

192. Wu, X.; Leonard, D. P.; Ji, X., Emerging Non-Aqueous Potassium-Ion Batteries: Challenges and Opportunities. *Chemistry of Materials* 2017, *29* (12), 5031-5042.

193. Lu, Y.; Wang, L.; Cheng, J.; Goodenough, J. B., Prussian blue: a new framework of electrode materials for sodium batteries. *Chemical Communications* 2012, *48* (52), 6544-6546.

194. Bie, X.; Kubota, K.; Hosaka, T.; Chihara, K.; Komaba, S., Synthesis and electrochemical properties of Na-rich Prussian blue analogues containing Mn, Fe, Co, and Fe for Na-ion batteries. *Journal of Power Sources* 2018, *378*, 322-330.

195. Wessells, C. D.; Peddada, S. V.; Huggins, R. A.; Cui, Y., Nickel Hexacyanoferrate Nanoparticle Electrodes For Aqueous Sodium and Potassium Ion Batteries. *Nano Letters* 2011, *11* (12), 5421-5425.

196. Qian, J.; Wu, C.; Cao, Y.; Ma, Z.; Huang, Y.; Ai, X.; Yang, H., Prussian Blue Cathode Materials for Sodium-Ion Batteries and Other Ion Batteries. *Advanced Energy Materials*, 1702619.

197. Li, C.; Zang, R.; Li, P.; Man, Z.; Wang, S.; Li, X.; Wu, Y.; Liu, S.; Wang, G., High Crystalline Prussian White Nanocubes as a Promising Cathode for Sodium-ion Batteries. *Chemistry – An Asian Journal* 2018, *13* (3), 342-349.

198. Xueying Yang, J. L., Xinkun Song, Yingzhao He, Xiaoxiao Du, Yongjin Zou, Haitao Zhang, Facile Synthesis of Polyaniline-Prussian Blue Composite for High- Performance Supercapacitors. *Int J Nanoparticles Nanotech* 2017, *3* (1), 011.

199. He, G.; Nazar, L. F., Crystallite Size Control of Prussian White Analogues for Nonaqueous Potassium-Ion Batteries. *ACS Energy Letters* 2017, *2* (5), 1122-1127.

200. Wang, J.; Purewal, J.; Liu, P.; Hicks-Garner, J.; Soukazian, S.; Sherman, E.; Sorenson, A.; Vu, L.; Tataria, H.; Verbrugge, M. W., Degradation of lithium ion batteries employing graphite negatives and nickel–cobalt–manganese oxide + spinel manganese oxide positives: Part 1, aging mechanisms and life estimation. *Journal of Power Sources* 2014, *269*, 937-948.

201. Taberna, P. L.; Mitra, S.; Poizot, P.; Simon, P.; Tarascon, J. M., High rate capabilities Fe3O4-based Cu nano-architectured electrodes for lithium-ion battery applications. *Nature Materials* 2006, *5*, 567.

202. McCargar, J. W.; Neff, V. D., Thermodynamics of mixed-valence intercalation reactions: the electrochemical reduction of Prussian blue. *The Journal of Physical Chemistry* 1988, *92* (12), 3598-3604.

203. Wessells, C. D.; Peddada, S. V.; McDowell, M. T.; Huggins, R. A.; Cui, Y., The Effect of Insertion Species on Nanostructured Open Framework Hexacyanoferrate Battery Electrodes. *Journal of The Electrochemical Society* 2011, *159* (2), A98-A103.

204. Gu, W. B.; Wang, C. Y., Thermal-Electrochemical Modeling of Battery Systems. *Journal of The Electrochemical Society* 2000, *147* (8), 2910-2922.

205. Cohn, A. P.; Muralidharan, N.; Carter, R.; Share, K.; Pint, C. L., Anode-Free Sodium Battery through in Situ Plating of Sodium Metal. *Nano Letters* 2017, *17* (2), 1296-1301.

206. Cannarella, J.; Arnold, C. B., The Effects of Defects on Localized Plating in Lithium-Ion Batteries. *Journal of The Electrochemical Society* 2015, *162* (7), A1365-A1373.

207. Liu, X. M.; Arnold, C. B., Effects of Cycling Ranges on Stress and Capacity Fade in Lithium-Ion Pouch Cells. *Journal of The Electrochemical Society* 2016, *163* (13), A2501-A2507.

208. González, C.; Vilatela, J. J.; Molina-Aldareguía, J. M.; Lopes, C. S.; Llorca, J., Structural composites for multifunctional applications: Current challenges and future trends. *Progress in Materials Science* 2017, *89*, 194-251.

209. Ferreira, A. D. B. L.; Nóvoa, P. R. O.; Marques, A. T., Multifunctional Material Systems: A state-of-the-art review. *Composite Structures* 2016, *151*, 3-35.

210. Thomas, J. P.; Qidwai, M. A., Mechanical design and performance of composite multifunctional materials. *Acta Materialia* 2004, *52* (8), 2155-2164.

211. Thomas, J.; Qidwai, S., The design and application of multifucntional structure-battery materials. *Journal of Minerals, Metals and Materials Society* 2005, *57*, 18-24.

212. Ding, J.; Zhou, H.; Zhang, H.; Tong, L.; Mitlin, D., Selenium Impregnated Monolithic Carbons as Free-Standing Cathodes for High Volumetric Energy Lithium and Sodium Metal Batteries. *Advanced Energy Materials* 2018, *8* (8), 1701918.

213. Snyder, J. F.; Carter, R. H.; Wetzel, E. D., Electrochemical and Mechanical Behavior in Mechanically Robust Solid Polymer Electrolytes for Use in Multifunctional Structural Batteries. *Chemistry of Materials* 2007, *19* (15), 3793-3801.

214. Johnson, D. J., Structure-property relationships in carbon fibres. *Journal of Physics D: Applied Physics* 1987, *20* (3), 286.

215. Pupurs, A.; Varna, J., Modeling mechanical stress and exfoliation damage in carbon fiber electrodes subjected to cyclic intercalation/deintercalation of lithium ions. *Composites Part B: Engineering* 2014, *65*, 69-79.

216. Wang, G.; Babaahmadi, V.; He, N.; Liu, Y.; Pan, Q.; Montazer, M.; Gao, W., Wearable supercapacitors on polyethylene terephthalate fabrics with good wash fastness and high flexibility. *Journal of Power Sources* 2017, *367*, 34-41.

217. Muralidharan, N.; Teblum, E.; Westover, A. S.; Schauben, D.; Itzhak, A.; Muallem, M.; Nessim, G. D.; Pint, C. L., Carbon Nanotube Reinforced Structural Composite Supercapacitor. *Scientific Reports* 2018, *8* (1), 17662.

218. Westover, A. S.; Baer, B.; Bello, B. H.; Sun, H.; Oakes, L.; Bellan, L. M.; Pint, C. L., Multifunctional high strength and high energy epoxy composite structural supercapacitors with wet-dry operational stability. *Journal of Materials Chemistry A* 2015, *3* (40), 20097-20102.

219. Westover, A. S.; Tian, J. W.; Bernath, S.; Oakes, L.; Edwards, R.; Shabab, F. N.; Chatterjee, S.; Anilkumar, A. V.; Pint, C. L., A Multifunctional Load-Bearing Solid-State Supercapacitor. *Nano Letters* 2014, *14* (6), 3197-3202.

220. Westover, A. S.; Tian, J.; Bernath, S.; Oakes, L.; Edwards, R.; Shabab, F. N.; Chatterjee, S.; Anilkumar, A.; Pint, C. L., Multifunctional Load-Bearing Energy Storage Materials. 2014, (46514), V06AT07A033.

221. Pan, Q.; Shim, E.; Pourdeyhimi, B.; Gao, W., Highly Conductive Polypropylene–Graphene Nonwoven Composite via Interface Engineering. *Langmuir* 2017, *33* (30), 7452-7458.

222. Meng, C.; Muralidharan, N.; Teblum, E.; Moyer, K. E.; Nessim, G. D.; Pint, C. L., Multifunctional Structural Ultrabattery Composite. *Nano Letters* 2018.

223. Gong, Y.; Fu, K.; Xu, S.; Dai, J.; Hamann, T. R.; Zhang, L.; Hitz, G. T.; Fu, Z.; Ma, Z.; McOwen, D. W.; Han, X.; Hu, L.; Wachsman, E. D., Lithium-ion conductive ceramic textile: A new architecture for flexible solid-state lithium metal batteries. *Materials Today* 2018, *21* (6), 594-601.

224. Yao, J.; Xie, J.; Nishimura, K.; Mukai, T.; Takasaki, T.; Tsutsumi, K.; Sakai, T., Lithium manganese aluminum oxide-based full Li-ion battery using carbon fibers as current collectors. *Ionics* 2013, *19* (12), 1849-1853.

225. Willgert, M.; Kjell, M. H.; Lindbergh, G.; Johansson, M., New structural lithium battery electrolytes using thiol–ene chemistry. *Solid State Ionics* 2013, *236*, 22-29.

226. Johannisson, W.; Ihrner, N.; Zenkert, D.; Johansson, M.; Carlstedt, D.; Asp, L. E.; Sieland, F., Multifunctional performance of a carbon fiber UD lamina electrode for structural batteries. *Composites Science and Technology* 2018, *168*, 81-87.

227. Yu, Y.; Zhang, B.; Feng, M.; Qi, G.; Tian, F.; Feng, Q.; Yang, J.; Wang, S., Multifunctional structural lithium ion batteries based on carbon fiber reinforced plastic composites. *Composites Science and Technology* 2017, *147*, 62-70.

228. Pereira, T.; Guo, Z.; Nieh, S.; Arias, J.; Hahn, H. T., Embedding thin-film lithium energy cells in structural composites. *Composites Science and Technology* 2008, *68* (7), 1935-1941.

229. Tony Pereira, Z. G., S. Nieh, J. Arias, H. Thomas Hahn, Energy Storage Structural Composites: A Review. *Journal of Composite Materials* 2009, *43*, 549-560.

230. Snyder, J. F.; Wong, E. L.; Hubbard, C. W., Evaluation of Commercially Available Carbon Fibers, Fabrics, and Papers for Potential Use in Multifunctional Energy Storage Applications. *Journal of The Electrochemical Society* 2009, *156* (3), A215-A224.

231. Kim, H. S.; Kang, J. S.; Park, J. S.; Hahn, H. T.; Jung, H. C.; Joung, J. W., Inkjet printed electronics for multifunctional composite structure. *Composites Science and Technology* 2009, *69* (7), 1256-1264.

232. Hagberg, J.; Maples, H. A.; Alvim, K. S. P.; Xu, J.; Johannisson, W.; Bismarck, A.; Zenkert, D.; Lindbergh, G., Lithium iron phosphate coated carbon fiber electrodes for structural lithium ion batteries. *Composites Science and Technology* 2018, *162*, 235-243.

233. Martha, S. K.; Kiggans, J. O.; Nanda, J.; Dudney, N. J., Advanced Lithium Battery Cathodes Using Dispersed Carbon Fibers as the Current Collector. *Journal of The Electrochemical Society* 2011, *158* (9), A1060-A1066.

234. Lu, H.; Hagberg, J.; Lindbergh, G.; Cornell, A., Li4Ti5O12 flexible, lightweight electrodes based on cellulose nanofibrils as binder and carbon fibers as current collectors for Li-ion batteries. *Nano Energy* 2017, *39*, 140-150.

235. Liu, P.; Sherman, E.; Jacobsen, A., Design and fabrication of multifunctional structural batteries. *Journal of Power Sources* 2009, *189* (1), 646-650.

236. Giulia, F.; Steffen, J.; Athmane, B.; Joachim, W.; Masoud, R.; Fang, L.; Ross, H.; Dan, Z.; Johan, H.; Göran, L.; Patrik, J.; Lorenzo, S.; Leif, E. A., Graphitic microstructure and

performance of carbon fibre Li-ion structural battery electrodes. *Multifunctional Materials* 2018, *1* (1), 015003.

237. Jacques, E.; H. Kjell, M.; Zenkert, D.; Lindbergh, G., The effect of lithium-intercalation on the mechanical properties of carbon fibres. *Carbon* 2014, *68*, 725-733.

238. Jacques, E.; Kjell, M. H.; Zenkert, D.; Lindbergh, G.; Behm, M.; Willgert, M., Impact of electrochemical cycling on the tensile properties of carbon fibres for structural lithium-ion composite batteries. *Composites Science and Technology* 2012, *72* (7), 792-798.

239. Asp, L.; Leijonmarck, S.; Carlson, T.; Lindbergh, G., *REALISATION OF STRUCTURAL BATTERY COMPOSITE MATERIALS*. 2015.

240. Kjell, M. H.; Jacques, E.; Zenkert, D.; Behm, M.; Lindbergh, G., Carbon Fiber Negative Electrodes for Structural Lithium-Ion Batteries. *Meeting Abstracts* 2011, *MA2011-02* (17), 1239.

241. Crompton, K. R.; Hladky, M. P.; Park, H. H.; Prokes, S. M.; Love, C. T.; Landi, B. J., Lithium-ion cycling performance of multi-walled carbon nanotube electrodes and current collectors coated with nanometer scale Al2O3 by atomic layer deposition. *Electrochimica Acta* 2018, *292*, 628-638.

242. Miran Beigi, A. A.; Abdouss, M.; Yousefi, M.; Pourmortazavi, S. M.; Vahid, A., Investigation on physical and electrochemical properties of three imidazolium based ionic liquids (1-hexyl-3-methylimidazolium tetrafluoroborate, 1-ethyl-3-methylimidazolium bis(trifluoromethylsulfonyl) imide and 1-butyl-3-methylimidazolium methylsulfate). *Journal of Molecular Liquids* 2013, *177*, 361-368.

243. Samareh, J. A.; Siochi, E. J., Systems analysis of carbon nanotubes: opportunities and challenges for space applications. *Nanotechnology* 2017, *28* (37), 372001.

244. Arepalli, S.; Moloney, P., Engineered nanomaterials in aerospace. *MRS Bulletin* 2015, *40* (10), 804-811.

245. Sakti, A.; Michalek, J. J.; Fuchs, E. R. H.; Whitacre, J. F., A techno-economic analysis and optimization of Li-ion batteries for light-duty passenger vehicle electrification. *Journal of Power Sources* 2015, *273*, 966-980.

246. Jin, Y.; Zhu, B.; Lu, Z.; Liu, N.; Zhu, J., Challenges and Recent Progress in the Development of Si Anodes for Lithium-Ion Battery. *Advanced Energy Materials* 2017, *7* (23), 1700715.

247. Chan, C. K.; Peng, H.; Liu, G.; McIlwrath, K.; Zhang, X. F.; Huggins, R. A.; Cui, Y., High-performance lithium battery anodes using silicon nanowires. *Nature Nanotechnology* 2008, *3* (1), 31-35.

248. Tao, J.; Liu, N.; Ma, W.; Ding, L.; Li, L.; Su, J.; Gao, Y., Solid-State High Performance Flexible Supercapacitors Based on Polypyrrole-MnO2-Carbon Fiber Hybrid Structure. *Scientific Reports* 2013, *3*, 2286.

249. Jiao, Z.; Wu, Q.; Cardon, L.; Qiu, J., Preparation and Electrochemical Performance of Hollow Activated Carbon Fiber Self-Supported Electrode for Supercapacitor. *Journal of Nanoscience and Nanotechnology* 2020, *20* (4), 2316-2323.

250. Qian, H.; Kucernak, A. R.; Greenhalgh, E. S.; Bismarck, A.; Shaffer, M. S. P., Multifunctional Structural Supercapacitor Composites Based on Carbon Aerogel Modified High Performance Carbon Fiber Fabric. *ACS Applied Materials & Interfaces* 2013, *5* (13), 6113-6122.

251. Shirshova, N.; Qian, H.; Houllé, M.; Steinke, J. H. G.; Kucernak, A. R. J.; Fontana, Q. P. V.; Greenhalgh, E. S.; Bismarck, A.; Shaffer, M. S. P., Multifunctional structural energy storage composite supercapacitors. *Faraday Discussions* 2014, *172* (0), 81-103.

252. Javaid, A.; Ho, K. K. C.; Bismarck, A.; Shaffer, M. S. P.; Steinke, J. H. G.; Greenhalgh, E. S., Multifunctional structural supercapacitors for electrical energy storage applications. *Journal of Composite Materials* 2013, *48* (12), 1409-1416.

253. Deka, B. K.; Hazarika, A.; Kim, J.; Park, Y.-B.; Park, H. W., Recent development and challenges of multifunctional structural supercapacitors for automotive industries. *International Journal of Energy Research* 2017, *41* (10), 1397-1411.

254. Liu, N.; Lu, Z.; Zhao, J.; McDowell, M. T.; Lee, H.-W.; Zhao, W.; Cui, Y., A pomegranate-inspired nanoscale design for large-volume-change lithium battery anodes. *Nature Nanotechnology* 2014, *9*, 187.

255. Cheng, H.; Liu, Z.; Huang, H.; Sun, X.; Li, Z., Stress distribution in carbon fiber-reinforced epoxy composites under the supercritical condition. *Polymer Composites* 2015, *36* (5), 961-968.

256. Ladpli, P.; Nardari, R.; Kopsaftopoulos, F.; Chang, F.-K., Multifunctional energy storage composite structures with embedded lithium-ion batteries. *Journal of Power Sources* 2019, *414*, 517-529.

257. Pereira, T.; Guo, Z.; Nieh, S.; Arias, J.; Hahn, H. T., Energy Storage Structural Composites: a Review. *Journal of Composite Materials* 2009, *43* (5), 549-560.

258. Carlstedt, D.; Asp, L. E., Thermal and diffusion induced stresses in a structural battery under galvanostatic cycling. *Composites Science and Technology* 2019, *179*, 69-78.

259. Dionisi, F.; Harnden, R.; Zenkert, D., A model to analyse deformations and stresses in structural batteries due to electrode expansions. *Composite Structures* 2017, *179*, 580-589.

260. Fredi, G.; Jeschke, S.; Boulaoued, A.; Wallenstein, J.; Rashidi, M.; Liu, F.; Harnden, R.; Zenkert, D.; Hagberg, J.; Lindbergh, G.; Johansson, P.; Stievano, L.; Asp, L. E., Graphitic

microstructure and performance of carbon fibre Li-ion structural battery electrodes. *Multifunctional Materials* 2018, *1* (1), 015003.

261. Han, Q.; Zhang, W.; Han, Z.; Niu, S.; Zhang, J.; Wang, F.; Li, X.; Geng, D.; Yu, G., Preparation of PAN-based carbon fiber/Co3O4 composite and potential application in structural lithium-ion battery anodes. *Ionics* 2019.

262. Ihrner, N.; Johannisson, W.; Sieland, F.; Zenkert, D.; Johansson, M., Structural lithium ion battery electrolytes via reaction induced phase-separation. *Journal of Materials Chemistry A* 2017, *5* (48), 25652-25659.

263. Javaid, A.; Ali, M. Z., Multifunctional structural lithium ion batteries for electrical energy storage applications. *Materials Research Express* 2018, *5* (5), 055701.

264. Johannisson, W.; Zenkert, D.; Lindbergh, G., Model of a structural battery and its potential for system level mass savings. *Multifunctional Materials* 2019, *2* (3), 035002.

265. Dasgupta, N. P.; Jung, H. J.; Trejo, O.; McDowell, M. T.; Hryciw, A.; Brongersma, M.; Sinclair, R.; Prinz, F. B., Atomic Layer Deposition of Lead Sulfide Quantum Dots on Nanowire Surfaces. *Nano Letters* 2011, *11* (3), 934-940.

266. Kazyak, E.; Wood, K. N.; Dasgupta, N. P., Improved Cycle Life and Stability of Lithium Metal Anodes through Ultrathin Atomic Layer Deposition Surface Treatments. *Chemistry of Materials* 2015, *27* (18), 6457-6462.

267. Kazyak, E.; Chen, K.-H.; Wood, K. N.; Davis, A. L.; Thompson, T.; Bielinski, A. R.; Sanchez, A. J.; Wang, X.; Wang, C.; Sakamoto, J.; Dasgupta, N. P., Atomic Layer Deposition of the Solid Electrolyte Garnet Li7La3Zr2O12. *Chemistry of Materials* 2017, *29* (8), 3785-3792.

268. Moon, J.; Jeong, J. Y.; Kim, J. I.; Kim, S.; Park, J. H., An ultrathin inorganic-organic hybrid layer on commercial polymer separators for advanced lithium-ion batteries. *Journal of Power Sources* 2019, *416*, 89-94.

269. Zhang, Y.; Song, Y.-Z.; Yuan, J.-J.; Yin, X.; Sun, C.-C.; Zhu, B.-K., Polypropylene separator coated with a thin layer of poly(lithium acrylate-co-butyl acrylate) for high-performance lithium-ion batteries. *Journal of Applied Polymer Science* 2018, *135* (26), 46423.

270. Kwon, Y.; Lee, Y.; Kim, S.-O.; Kim, H.-S.; Kim, K. J.; Byun, D.; Choi, W., Conducting Polymer Coating on a High-Voltage Cathode Based on Soft Chemistry Approach toward Improving Battery Performance. *ACS Applied Materials & Interfaces* 2018, *10* (35), 29457-29466.

271. Luo, J.; Fang, C.-C.; Wu, N.-L., High Polarity Poly(vinylidene difluoride) Thin Coating for Dendrite-Free and High-Performance Lithium Metal Anodes. *Advanced Energy Materials* 2018, *8* (2), 1701482.

272. Lopez, J.; Mackanic, D. G.; Cui, Y.; Bao, Z., Designing polymers for advanced battery chemistries. *Nature Reviews Materials* 2019, *4* (5), 312-330.

273. Shen, B. H.; Wang, S.; Tenhaeff, W. E., Ultrathin conformal polycyclosiloxane films to improve silicon cycling stability. *Science Advances* 2019, *5* (7), eaaw4856.

274. Qin, G.; Wu, Q.; Zhao, J.; Ma, Q.; Wang, C., C/LiFePO4/multi-walled carbon nanotube cathode material with enhanced electrochemical performance for lithium-ion batteries. *Journal of Power Sources* 2014, *248*, 588-595.

275. Atif Javaid, A. S., Hammad Tahir, Munazza Ali, Wajiha Younus, Investigation of Mechanical and Electrochemical Performance of

Multifunctional Carbon-Fiber Reinforced Polymer Composites for

Electrical Energy Storage Applications. *Journal of the Chemical Society of Pakistan* 2019, *41* (03), 444-451.

276. Gong, L.; Nguyen, M. H. T.; Oh, E.-S., High polar polyacrylonitrile as a potential binder for negative electrodes in lithium ion batteries. *Electrochemistry Communications* 2013, *29*, 45-47.

277. Xu, J.; Varna, J., Matrix and interface microcracking in carbon fiber/polymer structural micro-battery. *Journal of Composite Materials* 2019, *53* (25), 3615-3628.

278. Greenhalgh, E.; Ankersen, J.; Asp, L.; Bismarck, A.; Fontana, Q.; Houlle, M.; Kalinka, G.; Kucernak, A.; Mistry, M.; Nguyen, S.; Qian, H.; Shaffer, M.; Shirshova, N.; Steinke, J.; Wienrich, M., Mechanical, electrical and microstructural characterisation of multifunctional structural power composites. *Journal of Composite Materials* 2015, *49* (15), 1823-1834.

279. Boaretto, N.; Almenara, J.; Mikhalchan, A.; Marcilla, R.; Vilatela, J. J., A Route to High-Toughness Battery Electrodes. *ACS Applied Energy Materials* 2019, *2* (8), 5889-5899.

280. Das, A. D.; Mannoni, G.; Fruh, A.; Orsi, D.; Pinalli, R.; Dalcanale, E., Damage-Reporting Carbon Fiber Epoxy Composites. *ACS Applied Polymer Materials* 2019.

281. Elgrishi, N.; Rountree, K. J.; McCarthy, B. D.; Rountree, E. S.; Eisenhart, T. T.; Dempsey, J. L., A Practical Beginner's Guide to Cyclic Voltammetry. *Journal of Chemical Education* 2018, *95* (2), 197-206.

282. Jochen Bernhard Gerschler, A. H., Dirk Uwe Sauer, Investigation of cycle-life of lithium-ion batteries by

means of electrochemical impedance spectroscopy. *Technische Mitteilungen* 2006, *99*, 214-220.